Absorption de l'eau et des nutriments par les racines des plantes : modélisation, analyse et simulation

Pierre-Henri Tournier

To cite this version:

Pierre-Henri Tournier. Absorption de l'eau et des nutriments par les racines des plantes : modélisation, analyse et simulation. Mathématiques générales [math.GM]. Université Pierre et Marie Curie - Paris VI, 2015. Français. NNT : 2015PA066030 . tel-01133805

Université Pierre et Marie Curie Laboratoire Jacques-Louis Lions

THÈSE DE DOCTORAT DE
l'Université Pierre et Marie Curie

Spécialité Mathématiques appliquées

École Doctorale de Sciences Mathématiques de Paris Centre

présentée par

Pierre-Henri TOURNIER

pour obtenir le grade de

DOCTEUR de l'UNIVERSITÉ PIERRE ET MARIE CURIE

Absorption de l'eau et des nutriments par les racines des plantes :
Modélisation, analyse et simulation

---

dirigée par Frédéric HECHT et Myriam COMTE

Soutenue publiquement le 4 février 2015 devant le jury composé de :

M$^{\text{me}}$ Myriam COMTE	Co-Directrice de thèse
M. Thierry COUPEZ	Examinateur
M. Robert EYMARD	Rapporteur
M. Frédéric HECHT	Directeur de thèse
M. Stefano MANCUSO	Rapporteur
M. Bertrand MAURY	Examinateur
M. Benoît PERTHAME	Examinateur

Résumé

Dans le contexte du développement d'une agriculture durable visant à préserver les ressources naturelles et les écosystèmes, il s'avère nécessaire d'approfondir notre compréhension des processus souterrains et des interactions entre le sol et les racines des plantes. Le système racinaire est responsable de l'absorption de l'eau et des nutriments, mais les racines sont enfouies dans le sol et il est difficile d'effectuer des mesures. Récemment, des modèles mécanistiques ont été développés dans le but de simuler le transport de l'eau et des nutriments ainsi que leur absorption par les racines des plantes à l'échelle du système racinaire entier, tout en tenant compte explicitement de l'architecture tridimensionnelle du système racinaire.

Dans cette thèse, on utilise des outils mathématiques et numériques pour développer des modèles mécanistiques explicites du mouvement de l'eau et des nutriments dans le sol et de l'absorption racinaire, gouvernés par des équations aux dérivées partielles non linéaires. Un accent est mis sur la prise en compte explicite de la géométrie du système racinaire et des processus à petite échelle survenant dans la rhizosphère, qui jouent un rôle majeur dans l'absorption racinaire. De tels modèles peuvent être utilisés pour étudier la manière dont la capacité d'absorption est affectée par la forme et l'architecture du système racinaire.

La première étude est dédiée à l'analyse mathématique d'un modèle d'absorption du phosphore (P) par les racines des plantes. L'évolution de la concentration de P dans la solution du sol est gouvernée par une équation de convection-diffusion avec une condition aux limites non linéaire à la surface de la racine, que l'on considère ici comme un bord du domaine du sol. On formule ensuite un problème d'optimisation de forme visant à trouver les formes racinaires qui maximisent l'absorption de P.

La seconde partie de cette thèse montre comment on peut tirer avantage des récents progrès du calcul scientifique dans le domaine de l'adaptation de maillage non structuré et du calcul parallèle afin de développer des modèles numériques du mouvement de l'eau et des solutés et de l'absorption racinaire à l'échelle de la plante, tout en prenant en compte les phénomènes locaux survenant à l'échelle de la racine unique.

D'abord, on présente un modèle éléments finis pour le transport de l'eau et des solutés

et l'absorption racinaire. Le système racinaire est représenté comme un réseau arborescent composé de segments de racine cylindriques. Le mouvement de l'eau dans le sol est décrit par l'équation de Richards. L'absorption et le transport de l'eau à travers le système racinaire sont pris en compte explicitement en définissant des flux radiaux et axiaux sur le réseau de segments. Un terme puits est défini dans l'équation de Richards afin de représenter les flux d'absorption dans le domaine du sol, couplant ainsi les flux dans le sol et dans la racine. Les termes puits représentant l'absorption de l'eau et des nutriments dans le domaine du sol sont construits pour correspondre au volume occupé par les racines, et un procédé d'adaptation de maillage est utilisé afin de capturer précisément la géométrie du système racinaire ainsi que les forts gradients présents au voisinage des racines. Une méthode de décomposition de domaine est introduite dans le but de résoudre les problèmes provenant de la discrétisation du sol.

Le second modèle numérique inclut la croissance racinaire et prend en compte la surface de la racine, partitionnant le domaine de calcul en deux sous-domaines, le domaine du sol et le système racinaire. L'approche domaine diffus nous permet d'éviter la difficulté de générer un maillage surfacique de l'interface complexe sol-racine en remplaçant la surface de la racine par une interface diffuse étroite grâce à l'introduction d'une fonction de phase auxiliaire. Lorsque l'on considère la croissance racinaire, une procédure d'adaptation de maillage parallèle est utilisée dans le but de capturer l'interface diffuse changeante ainsi que les processus locaux au voisinage des racines.

Summary

In the context of the development of sustainable agriculture aiming at preserving natural resources and ecosystems, it is necessary to improve our understanding of underground processes and interactions between soil and plant roots. Although the root system is responsible for taking up water and nutrients from the surrounding soil, roots are hidden below ground and measurements are difficult to obtain. Recently, mechanistic models have been developed that simulate soil water and solute transport with plant root uptake at the whole root system scale while taking the three-dimensional architecture of the root system explicitely into account.

In this thesis, we use mathematical and numerical tools to develop explicit mechanistic models of soil water and solute movement accounting for root water and nutrient uptake and governed by nonlinear partial differential equations. An emphasis is put on resolving the geometry of the root system as well as small scale processes occurring in the rhizosphere, which play a major role in plant root uptake. Such models can be used to study how the uptake pattern is affected by the shape and architecture of the root system.

The first study is dedicated to the mathematical analysis of a model of phosphorus (P) uptake by plant roots. The evolution of the concentration of P in the soil solution is governed by a convection-diffusion equation with a nonlinear boundary condition at the root surface, which is included as a boundary of the soil domain. A shape optimization problem is formulated that aims at finding root shapes maximizing P uptake.

The second part of this thesis shows how we can take advantage of the recent advances of scientific computing in the field of unstructured mesh adaptation and parallel computing to develop numerical models of soil water and solute movement with root water and nutrient uptake at the plant scale while taking into account local processes at the single root scale.

First, a finite element model of soil water and solute transport with root uptake is presented. The root system is represented as a tree-like network composed of cylindrical root segments. Soil water movement is described by the Richards equation. Water uptake and transport through the root system is explicitly taken into account by defining radial and axial water flows on the tree-like root network. Soil and root water flows are coupled via

a sink term in the Richards equation representing radial water uptake flows in the soil domain. The sink terms accounting for root water and nutrient uptake in the soil domain are constructed so as to match the volume occupied by the roots, and a mesh adaptation procedure is used to accurately capture the geometry of the root system as well as high gradients located near the roots. A parallel domain decomposition method is introduced in order to solve the problems arising from the soil discretization.

The second numerical model includes root growth and takes into account the actual surface of the root, splitting the computational domain into two subdomains, the soil domain and the root system. The diffuse domain approach allows us to avoid the difficulty of generating a surface mesh of the complex soil-root interface by replacing the root surface with a narrow diffuse interface through the introduction of an auxilliary phase field function. When considering root growth, a parallel transient mesh adaptation procedure is used in order to resolve the evolving diffuse interface as well as local processes near the roots.

Contents

List of Figures and Tables

Chapter 1

General introduction

Contents

1.1 Motivation

Over the last 50 years, global crop production has expanded threefold in order to meet the increasing food demand, largely through higher yields per unit of land and crop intensification. In the context of increasing population but limited increase in productive arable land surface area [78, 24], agricultural productivity needs to be further increased in a sustainable way in order to preserve ecosystem services.

The considerable increase in agricultural inputs during the Green Revolution, especially for nitrogen (N) and phosphate (P), resulted in imbalanced ecosystems and environmental degradation, with a massive and fast-increasing eutrophication of aquatic ecosystems [22, 25, 51], contamination of groundwaters by nitrate and emission of greenhouse gas [80].

Thus, contemporary agriculture is directed towards minimizing yield losses and limiting the degradation of soil and water resources by increasing nutrient use efficiency in crops while decreasing nutrient inputs in order to preserve ecosystem services.

In addition, sustainable use of P in agroecosystems is not solely focused on reducing detrimental environmental impacts: the world reserves of high grade P ores are expected to be exhausted by the end of 21st century at current rate of consumption of P fertilizers [30, 63, 73]. This rather short deadline clearly challenges the sustainability of current P fertilizer use in developed and emerging countries [9].

As constraints on agricultural resources are imposed due to resource limitations and environmental concerns, the importance of plant-soil interactions and root function in water and nutrient transport becomes increasingly clear. Improving nutrient use efficiency in low input agriculture requires a thorough understanding of plant-soil relationships and plant responses to the availability of spatially distributed soil water and plant-available nutrients.

Rhizosphere processes play a major role in root water and nutrient uptake and plant stress responses. However, their general understanding is often incomplete. Root systems are neglected because they are hidden below ground and their extensive branching makes description difficult. Moreover, the complexity of belowground interactions is almost impossible to explore through only experimental approaches and direct measurements. On top of that, acquiring experimental data is still a major limitation [50]. For instance, it is hardly feasible to probe the local conditions (e.g. concentrations of nutrients) close to various portions of a root system for soil-grown plants in field conditions.

Soil is a complex environment encompassing physical and chemical heterogeneity across a wide range of spatial and temporal scales. On top of the spatial and temporal heterogeneity that is inherent to root function and structure, one shall also account for the heterogeneity of distribution and availability of water and nutrients in the soil, and how roots adapt to such heterogeneity. Plant growth, water and nutrient uptake and availability can be largely determined by the local environment and local processes in the rhizosphere. Differences in chemical and physical properties between the rhizosphere and the bulk soil shall also be taken into account.

Besides, many rhizosphere processes that drive nutrient acquisition are not homogeneously distributed along root axes [32, 44].

Consequently, experimental and empirical approaches are inadequate for improving our understanding of plant-soil interactions in relation to heterogeneous soils with spatial and temporal variations in water and nutrient availability in combination with spatially distributed rooting systems. Modeling is thus a powerful alternative approach to further our understanding of soil and root interactions processes, and how they ultimately determine plant nutrition. Making use of simulation models and sensitivity analysis can be useful to understand and quantify uptake and transport processes, and ultimately help us make better use of plant roots and rhizosphere dynamics to establish sustainable crop production protocols.

1.2 Soil water movement and root water uptake

1.2.1 The transpiration-cohesion-tension theory

The transpiration-cohesion-tension theory was introduced by Dixon and Jolly in 1895 [11] to explain the ascent of sap in plants and trees and is now widely accepted. It relies on the physical properties of water, on mechanisms of water transport, and on the anatomical features of the xylem, the sap conducting vascular system. Water is transported as a continuous stream through the soil into the roots and plant xylem towards the plant canopy where it eventually transpires into the atmosphere. The cohesion-tension theory assumes continuity of the water column within the whole plant, from the absorbing surfaces of the roots to the transpiring leaves. The evaporation of water from the leaf surface through the stomata generates surface tension in the cell walls, which is the driving force for water movement. This surface tension creates negative pressure or tension in adjacent regions and in the xylem. This change is transmitted throughout the whole plant through the continuous water column by cohesion (mutual attraction between water molecules) and adhesion of water to walls of xylem conduits. This way, evaporation establishes pressure gradients in plant conducting tissues and pulls water from the soil across the roots through the plant to the atmosphere.

In 1948 Van den Honert [34] quantified the cohesion-tension theory by proposing an Ohm's law analogue of water flow in the soil-plant-atmosphere continuum, expressing the flux of water as a function of a driving force, the water potential gradient, and a proportionality factor that defines the ability of the transmitting medium to conduct water. In soil science, this relationship is known as Darcy's law.

1.2.2 Water potential

The driving force for water flow is the gradient in total water potential. Water potential is a quantitative expression of the free energy associated with water. Water flows without energy input from regions of higher potential to ones of lower potential. Water potential is formally defined in [2] as "the amount of work that must be done per unit quantity of pure water in order to transport reversibly and isothermally to the soil water at a considered point, an infinitesimal quantity of water from a reference pool. The reference pool is at the elevation, the temperature, and the external gas pressure of the considered point, and contains a solution identical in composition to the soil water at the considered point". The reference state most often used to define water potential is pure water at ambient temperature and standard atmospheric pressure. Water potential on a weight basis is expressed in unit length and denotes the equivalent height of a water column. It is referred to as the water head.

The total soil water potential or soil water head H can be expressed as the sum of individual components corresponding to the different fields acting on soil water as

$$H = h + z + h_o. \tag{1.2.1}$$

In saturated conditions, the pressure head h represents the hydrostatic pressure and is positive. In unsaturated conditions, h is negative and represents the matric potential which defines the combined effects of capillary and adsorptive forces within the soil matrix. Capillarity results from surface tension caused by liquid-gas interfaces forming and interacting within the soil pore geometry.

The gravitational head z denotes the effect of gravity and is simply the elevation of the point of interest relative to the reference level.

The osmotic head h_o is determined by the presence of solutes in soil water. Solutes reduce the free energy of water by diluting the water. Osmotic effects are effective only when solutes are constrained relative to water mobility by a selectively permeable membrane or a diffusion barrier, such as by a semi-permeable membrane in plant roots.

1.2.3 Richards equation

The soil matrix consists of individual solid grains forming interconnected pore spaces of varying sizes and shapes. The pore space contains the liquid and gas phases. The complex microporous structure of the soil aggregates makes description of soil water flow at the microscopic level difficult.

At the macroscopic level, soil water flow is commonly described by the Richards equation [61], which results from the combination of the steady-state Darcy expression and the continuity equation.

Darcy's law relates the discharge rate to the hydraulic conductivity and the pressure gradient:

$$q = -K\nabla H = -K\nabla(h+z), \tag{1.2.2}$$

where q [L T^{-1}] is the macroscopic Darcy flux and K [L T^{-1}] is the hydraulic conductivity and represents the ability of the soil to transmit water.

The volumetric water content θ [L^3 L^{-3}] is defined as the ratio of the volume of water to the total volume of soil and is related to the degree of saturation. The relationship between the water content and matric potential $\theta(h)$ is called the water retention curve and is dependent on the soil particle size distribution and soil texture, and the geometric arrangement of the solid particles and soil structure.

The hydraulic conductivity $K = K(\theta)$ depends on the permeability of the porous medium and on the degree of saturation. As a soil dries, larger pores empty first, causing the hydraulic conductivity to decrease. As progressively smaller pores drain, suction forces become stronger, matric potential becomes more negative, and hydraulic conductivity can drop by several orders of magnitude.

Finally, combining Darcy's law with the continuity equation expressing the conservation of mass

$$\frac{\partial\theta}{\partial t} = -\nabla.q + S, \tag{1.2.3}$$

we obtain the Richards equation:

$$\frac{\partial\theta(h)}{\partial t} = \nabla.(K(\theta(h))\nabla(h+z))+S. \tag{1.2.4}$$

S is a generic term representing potential sources or sinks such as root water uptake.

1.2.4 Root water uptake and transport

Roots are composed of radial cell layers forming different tissues with distinct properties. The inner center contains the stele which includes the xylem and phloem. The root cortex is bounded on the inside by the endodermis and on the outside by a layer of epidermal cells from where root hairs develop.

Water and solute movement throughout the root to the xylem occurs via three different pathways: the apoplastic, symplastic and transmembrane pathways. The apoplast consists in the continuous system of cell walls and intercellular cell spaces. The symplastic route involves cell to cell transport through plasmodesmata, cytoplasmic channels which traverse cell walls and form continuous pathways between cells. The transmembrane pathway involves membrane transport between cells: water enters a cell on one side and exits on the other side, thus crossing the plasma membrane of each cell in its path twice. At the endodermis, the apoplastic pathway is obstructed by the Casparian strip, a suberized band present on the radial and transverse cell walls. The endodermis regulates the passage of water and solutes which must then move through living plasma membranes and plasmodesmata and not simply diffuse through cell walls. The endodermis thus provides a major barrier to apoplastic flow and acts as a selective membrane for solute transport.

Following [18, 45], the complex processes governing water flow through roots can be simplified by viewing the root as a single semi-permable membrane.

The radial flux per unit area into the root from the soil j_r [L T^{-1}] can then be defined as

$$j_r = L_r\left[(h_s - h_r) + \sigma(h_{o,s} - h_{o,r})\right], \tag{1.2.5}$$

where h_s (respectively $h_{o,s}$) is the soil matric (respectively osmotic) potential at the soil-root interface, h_r (respectively $h_{o,r}$) is the matric (respectively osmotic) potential in the xylem, L_r [T^{-1}] is the radial conductivity for flow from the root surface to the xylem and σ is the reflection coefficient.

The reflection coefficient σ takes values between 0 and 1 and is an indication of the effectiveness of the membrane complex (plasmalemma and Casparian band) for water flow driven by osmotic gradients. If $\sigma = 0$, the membrane is fully permeable to both water and solutes and water flow is mainly apoplastic, while $\sigma = 1$ represents a perfect semi-permeable membrane such as occurs in a well developed endodermis.

Similarly, the axial flux up the root in the xylem j_x [L^3 T^{-1}] can be defined as

$$j_x = -K_x\frac{d(h_r+z)}{dl}, \tag{1.2.6}$$

where K_x [$L^3\ T^{-1}$] is the xylem axial conductance.

1.3 Soil solute transport

1.3.1 Transport processes

The movement and fate of solutes in the subsurface is affected by a number of processes. In particular, solute transport depends on the magnitude and direction of water flow. The movement of solutes with flowing water is referred to as advection or convection. Variations in the microscopic velocity at the pore scale lead to unequal solute movement in the direction of flow. This phenomenon is referred to as mechanical dispersion. Hydrodynamic dispersion denotes the combined effects of both mechanical dispersion and diffusion.

Advection

Advection describes the transport of solutes by bulk flow at the average water velocity. The advective solute flux j_c [$M\ L^{-2}\ T^{-1}$] is given by

$$j_c = qc, \tag{1.3.1}$$

where c [$M\ L^{-3}$] is the solute concentration in the solution and q is the macroscopic Darcy flux (1.2.2).

Diffusion

Molecular or ionic diffusion is the net transfer of particles from regions with higher to lower concentrations and is described by Fick's first law. To characterize diffusion in soils, the diffusivity in a free solution is adjusted to account for a smaller cross-sectional area available for diffusion and an increased path length. The diffusive flux j_d [$M\ L^{-2}\ T^{-1}$] can be written as

$$j_d = -\theta A_0 f_l \nabla c, \tag{1.3.2}$$

where A_0 [$L^2\ T^{-1}$] is the diffusion coefficient in free water and f_l is the so-called impedance or tortuosity factor. In [4], f_l is given by

$$f_l = \begin{cases} f_1\theta + f_2 & \text{for} \quad \theta \geq \theta_l, \\ \frac{\theta(f_1\theta_l + f_2)}{\theta_l} & \text{for} \quad \theta < \theta_l, \end{cases} \tag{1.3.3}$$

where f_1, f_2 and θ_l are parameters depending on soil properties.

Dispersion

Local variations in soil water flow lead to mechanical dispersion. Dispersion may occur because of differences in velocity within an individual pore, different mean velocities in pores of different sizes, or the mean flow direction differing from the actual streamlines within individual pores.
Despite the conceptual differences between the diffusion and dispersion mechanisms, the dispersive flux j_m $[M\ L^{-2}\ T^{-1}]$ is often conveniently described by Fick's first law and can be defined by

$$j_m = -\theta D_m \nabla c, \tag{1.3.4}$$

where D_m is the dispersion tensor. For an isotropic soil, the components D_{ij} $[L^2\ T^{-1}]$ of the dispersion tensor are given by

$$D_{ij} = \delta_{ij} \alpha_T ||v|| + (\alpha_L - \alpha_T) \frac{v_i v_j}{||v||}, \tag{1.3.5}$$

where v_i $[L\ \mathrm{T}^{-1}]$ is the ith component of the pore water velocity $v = \frac{q}{\theta}$, δ_{ij} is the Kronecker delta and α_L $[L]$ and α_T $[L]$ are respectively the longitudinal and transverse dispersivity.

The total solute flux j_s $[M\ L^{-2}\ T^{-1}]$ can then be expressed as the sum of the advective, diffusive and dispersive components:

$$j_s = j_c + j_d + j_m. \tag{1.3.6}$$

Due to the macroscopic similarity between diffusion and mechanical dispersion, we can combine both processes by defining a single hydrodynamic dispersion tensor D:

$$j_s = qc - \theta D \nabla c. \tag{1.3.7}$$

In this thesis, the effects of mechanical dispersion are ignored and we only consider scalar diffusion.

Adsorption

Adsorption of ions in soils is an important phenomenon affecting the movement of solutes. Dissolved substances in the liquid phase can interact with several mineral and organic soil constituents. Contact of these charged colloids with the soil solution gives rise to surface reactions that include adsorption and ion exchange between soil particles and dissolved ions.
Adsorption and exchange reactions with the soil matrix can be described either by a kinetic reaction or by instantaneous equilibrium. For example, the Freundlich adsorption isotherm relates the adsorbed concentration c_s $[M\ L^{-3}]$ to the equilibrium concentration c in the soil solution as

$$c_s = \varphi(c) = \kappa c^b, \tag{1.3.8}$$

where κ and b are parameters of the model.

We can then express the total concentration c_T $[M\ L^{-3}]$ as the sum of the contributions of the liquid and solid phases:

$$c_T = \theta c + \varphi(c). \tag{1.3.9}$$

The convection-dispersion equation

By substituting (1.3.9) and (1.3.7) in the continuity equation

$$\frac{\partial c_T}{\partial t} = -\nabla . j_s + S_c \tag{1.3.10}$$

we obtain the following convection-dispersion equation

$$\frac{\partial(\theta c + \varphi(c))}{\partial t} = \nabla . (\theta D \nabla c - qc) + S_c. \tag{1.3.11}$$

Here S_c is a generic term accounting for potential sources or sinks such as fertilizer application or root nutrient uptake.

1.3.2 Root nutrient uptake

The rate at which water and nutrients are taken up by roots is important in generating the driving forces for movement of nutrients through the soil to the root surface either by mass flow or by diffusion following a concentration gradient. Once nutrients reach the root surface, they are transported to the xylem by passive and active processes.

Passive transport occurs in the apoplast and is kinetically controlled by diffusion and mass flow, with ion exchange occurring between the solution and the negatively-charged cell walls. The apoplastic route can be followed as far as the endodermis, where the presence of the Casparian strip restricts further movement.

The active ion transport across the plasmalemma against the concentration gradient is driven by specific energy-driven ion carriers or through ion channels embedded within the cell membrane. A major ion pathway is provided by proton pumps which transport protons (H^+) out of the cell, thereby creating pH and electropotential gradients by which both cations and anions can move across respective membranes by ion channels or carriers [52]. The energy required for active nutrient transport is metabolically driven by reduction of ATP. Energy demand for ion uptake can be large and can consume as much as 35% of the total respiratory energy.

Active nutrient uptake and its ion-selectivity can be regarded as a kinetic process equivalent to that described by Michaelis-Menten type kinetics, used for the description of enzym-catalyzed reactions [3]. Here, the Michaelis-Menten model relates the uptake rate to the concentration in the soil solution.

The uptake flux per unit area at the root surface $h(c)$ $[M\,L^{-2}\,T^{-1}]$ is then given by

$$h(c) = \frac{F_m c}{K_m + c}, \tag{1.3.12}$$

where F_m $[M\,L^{-2}\,T^{-1}]$ is the maximum uptake rate. The Michaelis constant K_m $[M\,L^{-3}]$ is the concentration at which the uptake rate is half of F_m.

The Michaelis-Menten parameters F_m and K_m are ion-specific and depend on several factors such as plant species and plant age.

1.4 Modeling soil-root interactions

The heterogeneity in soil water and nutrient distribution and availability in combination with the spatial development of the root system and the local processes occuring in the rhizosphere are of crucial importance in plant-soil relationships. However, most plant nutrition models ignore the dynamics of soil water and nutrient availability and uptake. They are usually limited to one spatial dimension and rely on empirical quantities, such as root length density. They do not account for root architecture, in spite of its importance in soil resource exploration and exploitation efficiency.

Nevertheless, considerable progress has been made in the modeling of root system architecture, and multidimensional models are now available that explicitly take into account the geometry of the root system. A first attempt to a mechanistic three-dimensional modeling approach of soil water and nutrient transport with root growth and root uptake was presented by Somma et al. in 1998 [69]. Since then, several numerical models at the whole root system scale have been developed that explicitly account for the three-dimensional distribution of water and nutrient uptake at the centimeter scale [14, 36, 65]. In these models, the simulation domain is discretized into a grid of soil voxels and root uptake is represented by a sink term in each voxel.

Such mechanistic models have a broad range of potential applications. They can be used to perform in silico experiments and explore large ranges of simulation scenarios to study the impact of various parameters, as well as help develop and calibrate simpler models by assessing the validity of assumptions and quantifying the effect of simplifications that are made in those simpler models.

1.5 Thesis outline

In this thesis, we study mechanistic models of soil water movement and solute transport with root uptake that explicitly take into account the geometry of the root system. We are interested in the mathematical and numerical treatment of the equations arising from these models.

Chapter 2 presents a mathematical analysis of a model of root phosphorus uptake governed by the convection-diffusion equation with a nonlinear boundary condition at the root surface. We first study the well-posedness of the associated Cauchy problem. We obtain existence and uniqueness of the solution in Hölder spaces under appropriate regularity assumptions on the data. Then, we define a shape optimization problem which aims at modifying the shape of the root in order to maximize root P uptake. A gradient descent algorithm based on the adjoint state method is used in order to solve the shape optimization problem. A numerical example in two spatial dimensions illustrates the optimization process.

Chapter 3 describes an adaptive finite element model of soil water and nutrient transport with root uptake. The model aims at including local processes in the rhizosphere at the whole root system scale by taking advantage of unstructured mesh adaptation. The model is comparable to [14], where the root system is represented as a tree-like network composed of cylindrical root segments and radial and axial water flows are defined for each segment. Soil and root water flows are coupled via a sink term in Richards equation and the two problems are solved iteratively until convergence at each time step. The sink terms representing root water and nutrient uptake are built from a characteristic function of the root system, representative of its geometry. This characteristic function is used to drive the mesh adaptation procedure, so that the adapted mesh can accurately resolve the complex geometry of the root system as well as small-scale phenomena in the vicinity of the roots. Since such an approach can be computationally intensive, a parallelization technique based on a scalable two-level Schwarz domain decomposition method is used to solve linear systems arising from the discretization of the soil problems. Some numerical experiments are conducted to illustrate the capabilities of the model.

In chapter 4, we use mathematical and numerical tools to develop a model of water and nutrient transport together with root uptake and root growth that explicitly takes into account the actual surface of the root as a boundary. The computational domain is partitioned into two subdomains, the soil domain and the root system. The root surface acts as a boundary between the two subdomains. Since generating an explicit discretization of the root surface remains a difficult challenge, especially when considering root growth and complex root systems, a diffuse domain approach is introduced. In the diffuse domain approach, the root surface is described as the 0 level-set of a signed distance function. The geometry of the subdomains is approximated by a phase field function, which replaces the sharp soil-root interface by a diffuse layer, allowing us to bypass the need to build a surface mesh of the root surface. The original problem is then reformulated on the regular computational domain. The method of matched asymptotic expansions is used to show that the original problem is recovered as the width of the diffuse interface goes to 0. As in the previous chapter, a mesh adaptation procedure is used to refine the volume mesh in the vicinity of the diffuse interface in order to adequately capture the interface as well as local behaviour of the solution near the root. In order to keep an affordable computing time, a parallel approach is considered, involving parallel assembly and solution of linear systems as well as a parallel mesh adaptation procedure that is performed at each time step when considering root growth. Finally, some numerical simulation results including root growth and chemotropism are presented.

We conclude by discussing the limitations of the current modeling approach, suggesting various improvements and giving some perspectives for future work.

Chapter 2

Mathematical analysis of a model of phosphorus uptake

The content of this chapter is included in [8].

Contents

2.1 Introduction

Phosphorus (P) is an essential element for plant growth and metabolism. It is involved in many plant processes such as energy transfer, the synthesis of nucleic acids and membranes, plant respiration, photosynthesis and enzyme regulation. Adequate phosphorus nutrition stimulates early plant growth and hastens maturity.

P is one of the limiting factors for plant growth in many agricultural systems. P uptake by plants is often constrained by the very low solubility of P in the soil, as P is mostly present in unavailable forms because of adsorption, precipitation, or conversion to the organic form.

This leads to the application of up to four times the fertilizer necessary for crop production. This practice can result in polluted water systems, imbalanced ecosystems and degradation of the environment. Moreoever, at the current rate of usage of P fertilizer, readily available sources of phosphate rocks could be depleted in as little as 60-90 years.

This brings us to consider the problem of reducing fertilizer usage of P, which suggests improved efficiency of fertilizer methods in the short term, and adaptation of genotypes to P-deficient soils in the long term.

We therefore propose to study the transfer of P in the soil as well as its uptake by plant roots, as was done in [62] and [55]. P moves in soil through both diffusion and mass flow, although diffusion is dominant.

Let us consider a shape modeling the root surface. The exterior domain around the root is the studied section of the soil. Let us denote by $\Omega \subset \mathbb{R}^d (d = 2,3)$ the soil domain, delimited by the root surface and the domain boundaries. Let $\Gamma = \partial\Omega$. Let Γ_1 be the boundary representing the root surface and $\Gamma_2 = \Gamma \setminus \Gamma_1$.

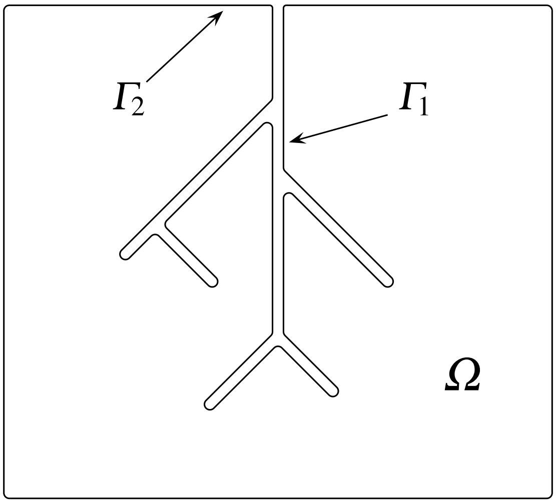

Figure 2.1 Configuration of the domain

Let $T > 0$ be given and $I = [0,T]$. The evolution of the concentration c of P in the soil is governed by the following convection-diffusion equation:

$$\begin{cases} \partial_t(\theta c + \varphi(c)) = \nabla.\big(A\nabla c - \vec{q}c\big) - R & \text{in} \quad I \times \Omega, \\ \alpha h(c) = -\big(A\nabla c - \vec{q}c\big)\cdot\vec{n} & \text{on} \quad I \times \Gamma_1, \\ 0 = \big(A\nabla c - \vec{q}c\big)\cdot\vec{n} & \text{on} \quad I \times \Gamma_2, \\ c(0,x) = c^0(x) & \text{in} \quad \Omega, \end{cases} \tag{2.1.1}$$

where

— $\vec{n}$ is the unit outward normal to the boundary of the domain,

— c^0 is the initial P concentration,

— A is the diffusion coefficient of P in the soil,

— θ is the volumetric water content,

- $\vec{q}$ is the groundwater flow,
- φ is an adsorption/desorption isotherm relating the amount of adsorbed P to the equilibrium concentration of P in solution; an example is the Freundlich adsorption isotherm [54], defined by:

$$\varphi(c) = \kappa c^b \text{ for } c \in [0,+\infty)\ ,\ \kappa > 0\ ,\ b \in (0,1),$$

- h is a model of enzyme kinetics, relating in this case the root uptake rate of P to its concentration at the root surface; an example is the Michaelis-Menten model [3], given by:

$$h(c) = \frac{F_m c}{K_m + c} \text{ for } c \in [0,+\infty)\ ,\ F_m > 0\ ,\ K_m > 0,$$

- R represents additional optional source/sink terms to the system. We will only consider source terms, such as fertilizer application.
- α is a parameter we introduce in order to obtain sufficient regularity of the boundary condition in the case $\Gamma_1 \cap \Gamma_2 \neq 0$: $\alpha \in C^\infty(\mathbb{R}^d)$ such that for $x \in \Gamma$

$$\begin{cases} 0 \leq \alpha(x) \leq 1 & \text{on } \Gamma_1 \\ \alpha(x) = 0 & \text{on } \Gamma_2. \end{cases}$$

We do not restrict ourselves to considering explicit forms for φ or h: we only use general properties of these functions throughout this chapter.
Since φ is defined on $[0,+\infty[$, we consider positive solutions of problem (2.1.1).

The chapter is organized as follows: we first discuss existence and uniquess of solutions to problem (2.1.1).
Then, we introduce a shape optimization method which enables us to modify the shape of the domain in order to maximize the amount of absorbed P, represented by the shape functional

$$J(c) = \int_0^T \int_{\Gamma_1} h(c),$$

subject to the volume constraint $|\Omega| = \text{constant}$.
Finally, we give a numerical example of the shape optimization process in two spatial dimensions.

2.2 A priori estimates

In this section, we derive upper and lower bounds for the solutions of problem (2.1.1) in the space $C^{1,2}(\overline{Q})$.

Let us first introduce some notations:

— S is the boundary of Ω,
— Q is the cylinder $(0,T)\times\Omega$,
— S_T is the lateral surface of Q: $S_T=\{(t,x)\mid t\in[0,T],x\in S\}$,
— $\theta^0(x):=\theta(0,x)$ for $x\in\overline{\Omega}$.

Moreover, we make the following assumptions:

hypotheses on S

$$S\in C^{2+\beta}, \tag{2.2.1}$$

hypotheses on c^0

$$\begin{aligned} &c^0\in C^{2+\beta}(\overline{\Omega}),\ c^0>0,\\ &\left(A\nabla c^0-\vec{q}c^0\right)\cdot\vec{n}+h(c^0)=0 \text{ on } \Gamma_1,\\ &\left(A\nabla c^0-\vec{q}c^0\right)\cdot\vec{n}=0 \text{ on } \Gamma_2, \end{aligned} \tag{2.2.2}$$

hypotheses on φ

$$\varphi\in C^3((0,+\infty)),\ \varphi'>0, \tag{2.2.3}$$

hypotheses on A

$$A\in C^{1+\beta/2,2+\beta}(\overline{Q}),\ A_m\geq A(t,x)\geq A_0>0 \text{ in } \overline{Q}, \tag{2.2.4}$$

hypotheses on θ

$$\theta\in C^{1+\beta/2,2+\beta}(\overline{Q}),\ \theta_m\geq\theta(t,x)\geq\theta_0>0 \text{ in } \overline{Q}, \tag{2.2.5}$$

hypotheses on R

$$R\in C^{1+\beta/2,2+\beta}(\overline{Q}),\ R<0 \text{ in } \overline{Q}, \tag{2.2.6}$$

hypotheses on $\vec{q}$

$$q_i\in C^{1+\beta/2,2+\beta}(\overline{Q}),\ i=1,..,d, \tag{2.2.7}$$

let us extend h to $\mathbb{R}$ so that

$$h\in C^2(\mathbb{R}),\ h(0)=0,\ \|h\|_{L^\infty(\mathbb{R})}+\|h'\|_{L^\infty(\mathbb{R})}+\|h''\|_{L^\infty(\mathbb{R})}\leq C_h. \tag{2.2.8}$$

Here and in the sequel,

$$\beta\in(0,1). \tag{2.2.9}$$

Now, let c be a solution of problem $(2.1.1)$ in the space $C^{1,2}(\overline{Q})$, $c\geq 0$ in $\overline{Q}$.

- Estimate from below:

Let $\varepsilon>0$, and let $T'=\max\{t\in[0,T]\mid c\geq\varepsilon \text{ in } [0,T']\times\overline{\Omega}\}$.
We now find a lower bound for c in $[0,T']\times\Omega$.

Let us introduce the following function

$$\hat{c}(t,x) := \delta e^{-Kt}\hat{c}_0(x), \quad (t,x) \in Q, \tag{2.2.10}$$

where $\delta, K > 0$ are chosen below and where $\hat{c}_0 \in C^2(\overline{\Omega})$ is a strictly positive function satisfying

$$A_0\frac{\partial \hat{c}_0}{\partial n} < -\|\vec{q}\|_{L^\infty(Q)}\hat{c}_0(x) - (h'(0)+1)\hat{c}_0(x) \quad \forall x \in S, \tag{2.2.11}$$

and

$$0 < \hat{c}_0(x) < 1 \quad \forall x \in \overline{\Omega}. \tag{2.2.12}$$

Choosing now K large enough and δ small enough, $\hat{c}$ satisfies

$$\begin{cases} \theta\hat{c}_t - \nabla.\big(A\nabla\hat{c} - \vec{q}\hat{c}\big) + R + \theta_t\hat{c} < 0 & \text{in } Q, \\ A\dfrac{\partial \hat{c}}{\partial n} < (\vec{q}\cdot\vec{n})\hat{c} - \alpha h(\hat{c}) & \text{on } S_T, \\ \hat{c}(0,x) < c^0(x) & \text{in } \overline{\Omega}. \end{cases} \tag{2.2.13}$$

Since $\varphi' \geq 0$, we can see that

$$(\theta + \varphi'(\hat{c}))\hat{c}_t - \nabla.\big(A\nabla\hat{c} - \vec{q}\hat{c}\big) + R + \theta_t\hat{c} < 0 \quad \text{in} \quad Q. \tag{2.2.14}$$

We now apply a comparison principle which results from the following theorem:

Theorem 2.1 ([20, Theorem 17 p. 53]). *Let v and w be two continuous functions in $\overline{Q}$, and let the first t-derivative and the first two x-derivatives of v, w be continuous in $\overline{Q}$. Let $F(t,x,p,p_i,p_{ij})$ $(i,j = 1,\dots,d)$ be a continuous function together with its first derivatives with respect to the p_{hk} in a domain E containing the closure of the set of points (t,x,p,p_i,p_{ij}) where*

$$(t,x) \in Q,\ p \in (v(t,x),w(t,x)),\ p_i \in \left(\frac{\partial v(t,x)}{\partial x_i}, \frac{\partial w(t,x)}{\partial x_i}\right),\ p_{ij} \in \left(\frac{\partial^2 v(t,x)}{\partial x_i \partial x_j}, \frac{\partial^2 w(t,x)}{\partial x_i \partial x_j}\right);$$

here (a,b) denotes the interval connecting a to b. Assume also that $(\partial F/\partial p_{hk})$ is a positive semidefinite matrix.

If

$$\begin{cases} \dfrac{\partial v}{\partial t} > F\left(t,x,v,\dfrac{\partial v}{\partial x_i},\dfrac{\partial^2 v}{\partial x_i \partial x_j}\right) & \text{in } Q, \\ \dfrac{\partial w}{\partial t} \leq F\left(t,x,w,\dfrac{\partial w}{\partial x_i},\dfrac{\partial^2 w}{\partial x_i \partial x_j}\right) & \text{in } Q, \\ v(0,x) > w(0,x) & \text{on } \overline{\Omega}, \\ \dfrac{\partial v}{\partial n} + \gamma(t,x,v) > \dfrac{\partial w}{\partial n} + \gamma(t,x,w) & \text{on } S_T, \end{cases} \tag{2.2.15}$$

for some function γ, then also $v > w$ in Q.

We have

$$\begin{cases} c_t = (\theta+\varphi'(c))^{-1}(\nabla.\big(A\nabla c-\vec{q}c\big)-R)-\theta_t c & \text{in} \quad [0,T']\times\Omega, \\ A\nabla c\cdot\vec{n} = (\vec{q}\cdot\vec{n})c-\alpha h(c) & \text{on} \quad [0,T']\times S, \end{cases} \tag{2.2.16}$$

and

$$\begin{cases} \hat{c}_t < (\theta+\varphi'(\hat{c}))^{-1}(\nabla.\big(A\nabla\hat{c}-\vec{q}\hat{c}\big)-R)-\theta_t\hat{c} & \text{in} \quad [0,T']\times\Omega, \\ A\nabla\hat{c}\cdot\vec{n} < (\vec{q}\cdot\vec{n})\hat{c}-\alpha h(\hat{c}) & \text{on} \quad [0,T']\times S. \end{cases} \tag{2.2.17}$$

Moreover, $\hat{c}(0,x) < c(0,x)$ in $\overline{\Omega}$.

It is easy to see that in our case F satisfies the hypotheses of Theorem 2.1 thanks to (2.2.3), (2.2.4), (2.2.5), (2.2.6) and (2.2.7).

Thus, we can apply Theorem 2.1 to c and $\hat{c}$ in $[0,T']\times\Omega$ in order to deduce that

$$c > \hat{c} \geq \delta e^{-KT}\min_{x\in\overline{\Omega}}\hat{c}_0(x) > 0 \quad \text{in} \quad [0,T']\times\Omega. \tag{2.2.18}$$

We proved that for every $\varepsilon > 0$, we have $c > \delta e^{-KT}\min_{x\in\overline{\Omega}}\hat{c}_0(x)$ in $[0,T']\times\Omega$, with $T' = \max\{t\in[0,T] \mid c\geq\varepsilon \text{ in } [0,T']\times\overline{\Omega}\}$. Note that the lower bound is independent of the choice of ε. Then, it is easy to see that if we take ε small enough and we suppose that $T' < T$, by a continuity argument ($c\in C^{1,2}(\overline{Q})$) we obtain that $c\geq\varepsilon$ in $[0,T'+\delta t]\times\overline{\Omega}$ for some $\delta t > 0$, which leads to a contradiction. Thus $T' = T$, and we can conclude that

$$c > \delta e^{-KT}\min_{x\in\overline{\Omega}}\hat{c}_0(x) > 0 \quad \text{in} \quad Q. \tag{2.2.19}$$

- Estimate from above:

Let $\check{c}_0 \in C^2(\overline{\Omega})$ satisfy

$$A_0\frac{\partial\check{c}_0}{\partial n} > \|\vec{q}\|_{L^\infty(Q)}\check{c}_0(x) \quad \forall x\in S, \tag{2.2.20}$$

and

$$\|c^0\|_{L^\infty(\Omega)} < \check{c}_0(x) < \|c^0\|_{L^\infty(\Omega)}+1 \quad \forall x\in\overline{\Omega}. \tag{2.2.21}$$

Let us define

$$\check{c}(t,x) := e^{\lambda t}\check{c}_0(x), \quad (t,x)\in Q, \tag{2.2.22}$$

for $\lambda > 0$. Then, for λ large enough it is clear that

$$\theta\check{c}_t-\nabla.\big(A\nabla\check{c}-\vec{q}\check{c}\big)+R+\theta_t\check{c} > 0 \quad \text{in} \quad Q, \tag{2.2.23}$$

which means that

$$(\theta+\varphi'(\check{c}))\check{c}_t-\nabla.\big(A\nabla\check{c}-\vec{q}\check{c}\big)+R+\theta_t\check{c} > 0 \quad \text{in} \quad Q. \tag{2.2.24}$$

We have

$$\begin{cases} c_t = (\theta+\varphi'(c))^{-1}(\nabla.\big(A\nabla c-\vec{q}c\big)-R)-\theta_t c & \text{in} \quad Q, \\ A\nabla c\cdot\vec{n} = (\vec{q}\cdot\vec{n})c-\alpha h(c) & \text{on} \quad S_T, \end{cases} \tag{2.2.25}$$

and

$$\begin{cases} \check{c}_t > (\theta+\varphi'(\check{c}))^{-1}(\nabla.\big(A\nabla \check{c}-\vec{q}\check{c}\big)-R)-\theta_t \check{c} & \text{in} \quad Q, \\ A\nabla \check{c}\cdot\vec{n} > (\vec{q}\cdot\vec{n})\check{c}-\alpha h(\check{c}) & \text{on} \quad S_T. \end{cases} \tag{2.2.26}$$

Moreover, $\check{c}(0,x) > c(0,x)$ in $\overline{\Omega}$.

Since we know that $c > \delta e^{-KT}\min\limits_{x\in\overline{\Omega}}\hat{c}_0(x)$ in Q, we can now apply Theorem 2.1 to c and $\check{c}$ in Q to deduce that

$$c(t,x) < \check{c}(t,x), \quad (t,x)\in Q.$$

Thus, we can conclude that there exist c_{min}, c_{max} such that

$$0 < c_{min} \leq c(t,x) \leq c_{max}, \quad (t,x)\in Q. \tag{2.2.27}$$

2.3 Uniqueness of solutions in $C^{1,2}(\overline{Q})$

In this section, we prove the uniqueness of solutions of problem (2.1.1) in the space $C^{1,2}(\overline{Q})$.

Let c_1, c_2 be two solutions of (2.1.1) belonging to $C^{1,2}(\overline{Q})$. From section 2.2, we know that

$$0 < c_{min} \leq c_1(t,x), c_2(t,x) \leq c_{max}, \quad (t,x)\in Q. \tag{2.3.1}$$

Let us multiply the equation satisfied by c_1-c_2 by c_1-c_2, integrate in Ω and integrate by parts. This yields:

$$\begin{aligned} &\frac{1}{2}\frac{d}{dt}\int_\Omega(\theta+\varphi'(c_1))|c_1-c_2|^2dx - \frac{1}{2}\int_\Omega(-\theta_t+\varphi''(c_1)c_{1,t})(c_1-c_2)^2dx \\ &+\int_\Omega(\varphi'(c_1)-\varphi'(c_2))(c_1-c_2)c_{2,t}dx + \int_\Omega A|\nabla c_1-\nabla c_2|^2dx \\ &-\int_\Omega \vec{q}\cdot\nabla(c_1-c_2)(c_1-c_2)\,dx - \int_\Gamma A\frac{\partial}{\partial n}(c_1-c_2)(c_1-c_2)d\sigma \\ &+\int_\Gamma(\vec{q}\cdot n)(c_1-c_2)^2d\sigma = 0. \end{aligned} \tag{2.3.2}$$

We use that $\theta_t \in L^\infty(\Omega\times(0,T))$ (see (2.2.5)), $\varphi''(c_1)\in L^\infty(\Omega\times(0,T))$ (thanks to (2.2.3) and (2.3.1)) and $\vec{q}\in L^\infty(\Omega\times(0,T))$. We obtain:

$$\begin{aligned} &\frac{1}{2}\frac{d}{dt}\int_\Omega(\theta+\varphi'(c_1))|c_1-c_2|^2dx + \int_\Omega A|\nabla c_1-\nabla c_2|^2dx \\ &\leq K\left(\int_\Omega(1+|c_{1,t}|+|c_{2,t}|)|c_1-c_2|^2 + \int_{\Gamma_1}|c_1-c_2|^2d\sigma\right). \end{aligned} \tag{2.3.3}$$

Here, we have also used that $|\alpha h(c_1)-\alpha h(c_2)|\leq K|c_1-c_2|$ and the same property for φ'.

- We estimate the first term in the right-hand side:

$$\left|\int_\Omega |c_1-c_2|^2(|c_{1,t}|+|c_{2,t}|)dx\right|\leq(\|c_{1,t}\|_{L^2(\Omega)}+\|c_{2,t}\|_{L^2(\Omega)})\|c_1-c_2\|^2_{L^4(\Omega)}.$$

Using that

$$\|f\|_{L^4(\Omega)}\leq\|f\|^{1/4}_{L^2(\Omega)}\|f\|^{3/4}_{L^6(\Omega)},$$

we deduce that

$$\left|\int_\Omega |c_1-c_2|^2(|c_{1,t}|+|c_{2,t}|)dx\right| \\ \leq(\|c_{1,t}\|_{L^2(\Omega)}+\|c_{2,t}\|_{L^2(\Omega)})\|c_1-c_2\|^{1/2}_{L^2(\Omega)}\|c_1-c_2\|^{3/2}_{L^6(\Omega)}.$$

Using now Young's inequality (for parameters 4 and $4/3$), we obtain, for every $\varepsilon\in[0,1]$ there exists K_ε such that

$$\left|\int_\Omega |c_1-c_2|^2(|c_{1,t}|+|c_{2,t}|)dx\right| \\ \leq K_\varepsilon(\|c_{1,t}\|^4_{L^2(\Omega)}+\|c_{2,t}\|^4_{L^2(\Omega)})\|c_1-c_2\|^2_{L^2(\Omega)}+\varepsilon\|c_1-c_2\|^2_{L^6(\Omega)}.$$

From the continuous injection $H^1(\Omega)\hookrightarrow L^6(\Omega)$ (recall that $d=2,3$), we get

$$\left|\int_\Omega |c_1-c_2|^2(1+|c_{1,t}|+|c_{2,t}|)dx\right| \\ \leq K'_\varepsilon(1+\|c_{1,t}\|^4_{L^2(\Omega)}+\|c_{2,t}\|^4_{L^2(\Omega)})\|c_1-c_2\|^2_{L^2(\Omega)}+\varepsilon\|c_1-c_2\|^2_{H^1(\Omega)}, \tag{2.3.4}$$

where K'_ε does not depend on K_ε.

- For the second term in the right-hand side of (2.3.2), we consider a function $\rho\in C^2(\overline{\Omega})$ satisfying $\frac{\partial\rho}{\partial n}\geq 1$ on S. Then,

$$\int_\Gamma\frac{\partial\rho}{\partial n}|c_1-c_2|^2d\sigma=2\int_\Omega(\nabla\rho\cdot\nabla(c_1-c_2))(c_1-c_2)\,dx+\int_\Omega\Delta\rho\,(c_1-c_2)^2dx.$$

From Young's inequality, we easily deduce that for every $\varepsilon\in[0,1]$ there exists K_ε such that

$$\int_{\Gamma_1}|c_1-c_2|^2d\sigma\leq K_\varepsilon\|c_1-c_2\|^2_{L^2(\Omega)}+\varepsilon\|\nabla(c_1-c_2)\|^2_{L^2(\Omega)}.$$

Putting this together with (2.3.4) and using (2.2.3), (2.2.4) and (2.2.5), we find

$$\begin{aligned}\frac{1}{2}\frac{d}{dt}\int_\Omega(\theta+\varphi'(c_1))|c_1-c_2|^2dx+\int_\Omega A|\nabla c_1-\nabla c_2|^2dx \\ \leq K_\varepsilon\theta_0^{-1}(1+\|c_{1,t}\|^4_{L^2(\Omega)}+\|c_{2,t}\|^4_{L^2(\Omega)})\int_\Omega(\theta+\varphi'(c_1))|c_1-c_2|^2dx \\ +\varepsilon\int_\Omega A|\nabla c_1-\nabla c_2|^2dx.\end{aligned}\tag{2.3.5}$$

Finally, taking $\varepsilon>0$ small enough and using Gronwall's Lemma, we deduce that $c_1=c_2$.

2.4 Existence and uniqueness of solutions in $C^{1+\beta/2,2+\beta}(\overline{Q})$

Recall that $\beta\in(0,1)$ is fixed (2.2.9).
In order to apply an existence and uniqueness theorem we need to define a new problem by truncating the function φ:
Let M_1,M_2 be such that $0<M_1<M_2$ and then let $M:=\begin{pmatrix}M_1\\M_2\end{pmatrix}$.
Then there exists $\varphi_M\in C^3(\mathbb{R})$ such that

$$\begin{cases}\varphi_M(c)=\varphi(c) \text{ for } M_1\leq c\leq M_2,\\ \varphi_M(c)=-\varepsilon_M \text{ for } c\leq-\varepsilon_M,\\ \varphi_M(c)=\varphi(M_2)+\varepsilon_M \text{ for } c\geq M_2+\varepsilon_M,\\ \varphi'_M\geq 0,\end{cases}$$

for some $\varepsilon_M>0$.
Note, in particular, that $\varphi'_M(c)=\varphi''_M(c)=\varphi'''_M(c)=0$ for $|c|>M_2+\varepsilon_M$ and that φ_M and its derivatives of up to order three are bounded.

Let us now define the new problem: find c_M such that

$$\begin{cases}\partial_t(\theta c_M+\varphi_M(c_M))=\nabla.\left(A\nabla c_M-\vec{q}c_M\right)-R & \text{in} \quad Q,\\ \alpha h(c)=-\left(A\nabla c_M-\vec{q}c_M\right)\cdot\vec{n} & \text{on} \quad I\times\Gamma_1,\\ 0=\left(A\nabla c_M-\vec{q}c_M\right)\cdot\vec{n} & \text{on} \quad I\times\Gamma_2,\\ c_M(0,x)=c^0(x) & \text{in} \quad \Omega.\end{cases}\tag{2.4.1}$$

Let us make the following change of variables:
let $y:=\theta c_M+\varphi_M(c_M)-\theta(0,x)c^0(x)-\varphi_M(c^0)$.

Note that y is strictly monotonically increasing in the variable c_M (recall that $\theta\geq\theta_0>0$ in $\overline{Q}$ and $\varphi'_M\geq 0$). Thus, we have $c_M=k(t,x,y)$ with k strictly monotonically increasing in the variable y.

Moreover, k is three times continuously differentiable with respect to y.
We can write the problem as follows:

$$\begin{cases} \partial_t y - \nabla.(A\nabla k - \vec{q}k) + R = 0 & \text{in } Q, \\ (A\nabla k - \vec{q}k)\cdot\vec{n} + \alpha h(k) = 0 & \text{on } I\times\Gamma_1, \\ (A\nabla k - \vec{q}k)\cdot\vec{n} = 0 & \text{on } I\times\Gamma_2, \\ y(0,x) = 0 & \text{in } \Omega. \end{cases} \tag{2.4.2}$$

We use the following notations for derivatives:

$$\frac{d}{dx}[a(x,u(x))] = \frac{\partial a}{\partial x} + \frac{\partial a}{\partial u}u_x = a_x + a_u u_x.$$

The equation in Q gives:

$$\partial_t y - \sum_i \frac{d}{dx_i}(A\frac{d}{dx_i}k) + \sum_i \frac{d}{dx_i}(q_i k) + R = 0.$$

Using the chain rule yields:

$$\partial_t y - \sum_i A\frac{d^2}{dx_i^2}k - \sum_i \frac{d}{dx_i}A\frac{d}{dx_i}k + \sum_i (k\frac{d}{dx_i}q_i + q_i\frac{d}{dx_i}k) + R = 0.$$

We obtain:

$$\begin{aligned} \partial_t y - A\sum_i \left[k_{x_ix_i} + k_y y_{x_ix_i} + k_{yx_i}y_{x_i} + k_{x_iy}y_{x_i} + k_{yy}y_{x_i}^2\right] \\ -\sum_i \left[A_{x_i}k_{x_i} + A_{x_i}k_y y_{x_i} - kq_{i_{x_i}} - q_i k_{x_i} - q_i k_y y_{x_i}\right] + R = 0. \end{aligned}$$

The equation in $I\times\partial(\Omega)$ gives:

$$\sum_i (A\frac{d}{dx_i}k - q_i k)cos(\vec{n},x_i) + \alpha h(k) = 0.$$

Using the chain rule again yields:

$$A\sum_i k_y y_{x_i} cos(\vec{n},x_i) + \sum_i (Ak_{x_i} - q_i k)cos(\vec{n},x_i) + \alpha h(k) = 0.$$

Finally, we can see that our problem is of the general form

$$\begin{cases} Ly := y_t - a_{ij}(x,t,y)y_{x_ix_j} + b(x,t,y,y_x) = 0, \\ L^{(S)}y := a_{ij}(x,t,y)y_{x_j}cos(\vec{n},x_i) + \psi(x,t,y)|_{S_T} = 0, \\ y|_{t=0} = 0, \end{cases} \tag{2.4.3}$$

with

$$\begin{cases} a_{ij} = 0 \quad \text{for} \quad i \neq j, \\ a_{ii} = Ak_y, \\ b = -A\sum_i \left[k_{x_i x_i} + k_{yx_i}y_{x_i} + k_{x_i y}y_{x_i} + k_{yy}y_{x_i}^2\right] \\ \qquad -\sum_i \left[A_{x_i}k_{x_i} + A_{x_i}k_y y_{x_i} - kq_{i_{x_i}} - q_i k_{x_i} - q_i k_y y_{x_i}\right] + R, \\ \psi = \sum_i (Ak_{x_i} - q_i k) cos(\vec{n}, x_i) + \alpha h(k). \end{cases} \tag{2.4.4}$$

We can now apply the following theorem to problem (2.4.3):

Theorem 2.2 ([43, Theorem 7.4 p. 491]). *Suppose the following conditions are fulfilled:*

There exists $\mu_1 > 0$ and $c_0, c_1, c_2, c_3, c_4 \geq 0$ such that for arbitrary y,

$$0 \leq \sum_{i,j} a_{ij}(x,t,y)\xi_i\xi_j \leq \mu_1\xi^2 \qquad \textit{for} \quad (t,x) \in \overline{Q}, \tag{2.4.5a}$$

$$-yb(x,t,y,p) \leq c_0 p^2 + c_1 y^2 + c_2 \qquad \textit{for} \quad (t,x) \in \overline{Q}, \tag{2.4.5b}$$

$$-y\psi(x,t,y) \leq c_3 y^2 + c_4 \qquad \textit{for} \quad (t,x) \in S_T, \tag{2.4.5c}$$

$$\sum_{i,j} a_{ij}(x,t,y)\xi_i\xi_j \geq \nu_1\xi^2 \qquad \textit{for} \quad (t,x) \in S_T. \tag{2.4.5d}$$

There exists $\nu, \mu > 0$ such that for $(t,x) \in \overline{Q}$, $|y| \leq N$ and for arbitrary p the functions $a_{ij}(x,t,y)$, $b(x,t,y,p)$ and $\psi(x,t,y)$ are continuous in their arguments, possess the derivatives entering into the following conditions and satisfy these conditions:

$$\nu\xi^2 \leq \sum_{i,j} a_{ij}(x,t,y)\xi_i\xi_j \leq \mu\xi^2, \tag{2.4.6a}$$

$$\left|\frac{\partial a_{ij}(x,t,y)}{\partial y}, \frac{\partial a_{ij}}{\partial x}, \psi, \frac{\partial \psi}{\partial y}, \frac{\partial \psi}{\partial x}\right| \leq \mu, \tag{2.4.6b}$$

$$|b(x,t,y,p)| \leq \mu(1+p^2), \tag{2.4.6c}$$

$$|\psi_{yy}(x,t,y)\ ,\ \psi_{yx}\ ,\ \psi_{yt}\ ,\ a_{ij_t}\ ,\ \psi_t| \leq \mu, \tag{2.4.7a}$$

$$|b_p|(1+|p|) + |b_y| + |b_t| \leq \mu(1+p^2), \tag{2.4.7b}$$

$$|a_{ij_{yy}}\ ,\ a_{ij_{yt}}\ ,\ a_{ij_{yx_j}}\ ,\ a_{ij_{x_j t}}| \leq \mu. \tag{2.4.7c}$$

For $(t,x) \in \overline{Q}$, $|y| \leq N$ and $|p| \leq N$, the functions $a_{ijx}(x,t,y)$ are Hölder continuous in the variables x with exponent β, $\psi_x(x,t,y)$ is Hölder continuous in x and t with exponent β and $\beta/2$ respectively, and $b(x,t,y,p)$ is Hölder continuous in x with exponent β. (2.4.8)

$$S \in C^{2+\beta}. \tag{2.4.9a}$$

$$\psi(x,0,0)|_{x \in S} = 0. \tag{2.4.9b}$$

Then problem (2.4.3) *has a unique solution* $y(t,x)$ *in the class* $C^{1+\beta/2,2+\beta}(\overline{Q})$.

Let us verify hypotheses (2.4.5a) to (2.4.9b) for our problem:

Proof of (2.4.5a) (2.4.5d) (2.4.6a). We have

$$k_y = \frac{1}{y_k \circ k} = \frac{1}{\theta + \varphi_M'(k)},$$

and since $0 < A_0 \le A(t,x) \le A_m$ in $\overline{Q}$ and $0 < \theta_0 \le \theta(t,x) + \varphi_M'(k) < +\infty$ in $\overline{Q} \times \mathbb{R}$, it follows that $(2.4.5a)$, $(2.4.5d)$ and $(2.4.6a)$ hold.

Proof of (2.4.5b) (2.4.5c). We have

$$\begin{aligned}-yb(x,t,y,p) =& \sum_i \left[Ak_{x_ix_i}y + A_{x_i}k_{x_i}y - kq_{i_{x_i}}y - q_ik_{x_i}y\right] - Ry \\ &+ A\sum_i \left[k_{yx_i}p_iy + k_{x_iy}p_iy + k_{yy}p_i^2y\right] + \sum_i \left[A_{x_i}k_yp_iy - q_ik_yp_iy\right].\end{aligned}$$

— Terms not involving p, for example $Ak_{x_ix_i}y$, are handled in this way:

$$\begin{aligned}k_{x_ix_j} =& -\frac{\theta_{x_ix_j}k}{\theta + \varphi_M'(k)} + \frac{2\theta_{x_i}\theta_{x_j}k}{(\theta + \varphi_M'(k))^2} - \frac{\theta_{x_i}\theta_{x_j}\varphi_M''(k)k^2}{(\theta + \varphi_M'(k))^3} \\ &+ \frac{\theta^0_{x_ix_j}c^0 + \theta^0_{x_i}c^0_{x_j} + (\theta^0 + \varphi_M'(c^0))c^0_{x_ix_j} + (\theta^0_{x_j} + \varphi_M''(c^0)c^0_{x_j})c^0_{x_i}}{\theta + \varphi_M'(k)} \\ &- \left(\theta^0_{x_i}c^0 + (\theta^0 + \varphi_M'(c^0))c^0_{x_i}\right) \\ &\left(\frac{\theta_{x_j}}{(\theta + \varphi_M'(k))^2} + \frac{\varphi_M''(k)(\theta^0_{x_i}c^0 + (\theta^0 + \varphi_M'(c^0))c^0_{x_i})}{(\theta + \varphi_M'(k))^3} - \frac{\varphi_M''(k)\theta_{x_i}k}{(\theta + \varphi_M'(k))^3}\right).\end{aligned}$$

We have $\theta_0 \le \theta(t,x) + \varphi_M'(k) < +\infty$. Moreover, for $|y|$ large enough there holds $k = \theta^{-1}y + c_t$ (with c_t bounded and independent of y) and $\varphi_M''(k) = 0$. Taking into account that θ, A, θ^0, c^0 and their space derivatives of up to order two are bounded , it follows that there exists $c_{3a}, c_{3b} \ge 0$ such that for arbitrary y

$$|Ak_{x_ix_i}y| \le c_{3a}y^2 + c_{3b} \quad \text{for} \quad (t,x) \in \overline{Q}.$$

Remaining terms not involving p are handled similarly.

— k_y, k_{yx_i} and k_{x_iy}, the derivatives appearing in terms involving p, can be bounded independently of y. In the case of the term $Ak_{yx_i}p_iy$, we have

$$k_{yx_i} = \frac{-\theta_{x_i}}{(\theta + \varphi_M'(k))^2} + \frac{\theta_{x_i}\varphi_M''(k)k}{(\theta + \varphi_M'(k))^3} - \frac{\varphi_M''(k)\left(\theta^0_{x_i}c^0 + (\theta^0 + \varphi_M'(c^0))c^0_{x_i}\right)}{(\theta + \varphi_M'(k))^3},$$

which leads to the fact that there exists $c_{t_2}, c_{5a}, c_{5b} \geq 0$ such that for arbitrary y

$$|Ak_{yx_i}p_i y| \leq c_{t_2}|p_i||y| \leq c_{5a}p^2 + c_{5b}y^2 \quad \text{for} \quad (t,x) \in \overline{Q}.$$

— The term $Ak_{yy}p_i^2 y$ remains. We have

$$k_{yy} = \frac{-\varphi_M''(k)k_y}{(\theta + \varphi_M'(k))^2} = \frac{-\varphi_M''(k)}{(\theta + \varphi_M'(k))^3},$$

which vanishes for $|y|$ large enough. It follows that there exists $c_6 \geq 0$ such that for arbitrary y

$$|Ak_{yy}p_i^2 y| \leq c_6 p^2 \quad \text{for} \quad (t,x) \in \overline{Q}.$$

Consequently, $(2.4.5b)$ holds.
$(2.4.5c)$ can be verified in the same way as $(2.4.5b)$.

Proof of (2.4.6b) (2.4.6c) (2.4.7a) (2.4.7b) (2.4.7c). It is easy to see that under the assumptions we made, all appearing quantities in these hypotheses are defined and bounded, thus it is clear that these conditions are verified.

Proof of (2.4.8). We have

$$\frac{\partial a_{ii}(x,t,y)}{\partial x_j} = A_{x_j}k_y + Ak_{yx_j},$$
$$\frac{\partial \psi}{\partial x_j} = \sum_i [(A_{x_j}k_{x_i} + Ak_{x_i x_j} - q_{i_{x_j}}k - q_i k_{x_j})n_i + (Ak_{x_i} - q_i k)n_{i_{x_j}}] + \alpha h'(k)k_{x_j} + \alpha_{x_j}h(k),$$

and one can easily verify that under the assumptions we made, the Hölder continuity hypotheses on $a_{ijx}(x,t,y)$, $\psi_x(x,t,y)$ and $b(x,t,y,p)$ required by $(2.4.8)$ hold true.

Proof of (2.4.9a). We made the assumption that $S \in C^{2+\beta}$.

Proof of (2.4.9b). We have the following initial and boundary compatibility condition:

$$(A\nabla c^0 - \vec{q}c^0) \cdot \vec{n} + \alpha h(c^0) = 0 \quad \text{on} \quad S,$$

which, since $k|_{t=0} = c^0$, leads to

$$\psi(x,0,0) = \sum_i (Ac_{x_i}^0 - q_i c^0)cos(\vec{n},x_i) + \alpha h(c^0) = 0 \quad \text{on} \quad S,$$

and $(2.4.9b)$ holds.

Thus, problem $(2.4.3)$ has a unique solution y in the class $C^{1+\beta/2,2+\beta}(\overline{Q})$.
Consequently, problem $(2.4.1)$ has a unique solution c_M in the class $C^{1+\beta/2,2+\beta}(\overline{Q})$.
Now, note that we can find estimates for solutions c_M of problem $(2.4.1)$ in exactly the

same way we did for problem (2.1.1) in section 2.2. Moreover, one can easily see that c_M can be bounded independently of M: $\forall\, M = \begin{pmatrix} M_1 \\ M_2 \end{pmatrix}$, $0 < M_1 < M_2$,

$$0 < c_{min} \leq c_M(t,x) \leq c_{max}, \quad (t,x) \in Q. \tag{2.4.10}$$

We can then choose M so that $M_1 < c_{min}$ and $M_2 > c_{max}$. It follows that the unique solution c_M of problem (2.4.1) is also a solution of the original problem (2.1.1). Thus, using the fact that problem (2.1.1) has at most one solution in the space $C^{1,2}(\overline{Q})$ which was proven in section 2.3, we can deduce that problem (2.1.1) has a unique solution in the space $C^{1+\beta/2,2+\beta}(\overline{Q})$.

2.5 Shape optimization

In this section, we use the tools of shape optimization presented in [68], [26] and [28] to find root shapes that increase the amount of absorbed P. More specifically, we want to deform Ω so as to maximize the shape functional

$$J(c) = \int_0^T \int_{\Gamma_1} \alpha h(c), \tag{2.5.1}$$

where $|\Omega| =$ a given constant.
We also assume that A and $\vec{q}$ are constants and we take $R = 0$.
We introduce a vector field $\vec{V} \in C^2(\mathbb{R}^d, \mathbb{R}^d)$ and we consider $\Omega_s = (Id + s\vec{V})(\Omega)$ where s is a small parameter.
Let c_s be the unique solution of the problem on the perturbed domain:

$$\begin{cases} \partial_t(\theta c_s + \varphi(c_s)) = \nabla.\big(A\nabla c_s - \vec{q}c_s\big) & \text{in} \quad I \times \Omega_s, \\ \alpha h(c_s) = -\big(A\nabla c_s - \vec{q}c_s\big) \cdot \vec{n} & \text{on} \quad I \times \Gamma_{1,s}, \\ 0 = -\big(A\nabla c_s - \vec{q}c_s\big) \cdot \vec{n} & \text{on} \quad I \times \Gamma_{2,s}, \\ c_s(0,x) = c^0(Id + s\vec{V})^{-1}(x)) & \text{in} \quad \Omega_s. \end{cases} \tag{2.5.2}$$

Let us now denote by c' the derivative of c with respect to the domain: $c' = \frac{d}{ds} c_s|_{s=0}$.
According to [28, Prop. 5.4.18 p. 201], the derivative of the functional J at Ω in the direction $\vec{V}$ is given by

$$dJ(c,\vec{V}) = \int_0^T \left(\int_{\Gamma_1} \alpha h'(c)c' + \int_{\Gamma_1} \alpha H h(c)(\vec{V}\cdot\vec{n}) + \int_{\Gamma_1} \frac{\partial(\alpha h(c))}{\partial n}(\vec{V}\cdot\vec{n}) \right) \tag{2.5.3}$$

where H is the mean curvature of Γ.
We first need to find the equation satisfied by c':
The solution c of the initial problem satisfies

$$\int_0^T \int_\Omega \partial_t(\theta c + \varphi(c))v + \int_0^T \int_\Omega A\nabla c \cdot \nabla v - \int_0^T \int_\Omega c\vec{q} \cdot \nabla v + \int_0^T \int_{\Gamma_1} \alpha h(c)v = 0 \tag{2.5.4}$$

for all $v \in H^1(\Omega)$ such that $v(T,.) = 0$.
Differentiating (2.5.4) using rules presented in [28] gives

$$\begin{aligned}
&\int_0^T \int_\Omega \partial_t(\theta c' + \varphi'(c)c')v + \int_0^T \int_\Gamma \partial_t(\theta c + \varphi(c))v(\vec{V}\cdot\vec{n}) + \int_0^T \int_\Omega A\nabla c' \cdot \nabla v \\
&+ \int_0^T \int_\Gamma A\nabla c \cdot \nabla v(\vec{V}\cdot\vec{n}) - \int_0^T \int_\Omega c'\vec{q}\cdot\nabla v - \int_0^T \int_\Gamma c\vec{q}\cdot\nabla v(\vec{V}\cdot\vec{n}) \\
&+ \int_0^T \int_{\Gamma_1} \alpha h'(c)c'v + \int_0^T \int_{\Gamma_1} H\alpha h(c)v(\vec{V}\cdot\vec{n}) + \int_0^T \int_{\Gamma_1} \frac{\partial(\alpha h(c)v)}{\partial n}(\vec{V}\cdot\vec{n}) = 0.
\end{aligned} \tag{2.5.5}$$

First taking v in $\mathcal{D}(\Omega)$, we obtain that

$$\frac{\partial}{\partial t}\big(\theta c' + \varphi'(c)c'\big) - A\Delta c' + \vec{q}\cdot\nabla c' = 0 \quad \text{in} \quad Q. \tag{2.5.6}$$

Integrating by parts $\int_\Omega (A\nabla c' - c'\vec{q})\cdot\nabla v$ in (2.5.5) and using (2.5.6) gives

$$\begin{aligned}
-\int_0^T \int_\Gamma A\frac{\partial c'}{\partial n}v - c'v\vec{q}\cdot\vec{n} = &\int_0^T \int_\Gamma \partial_t(\theta c + \varphi(c))v(\vec{V}\cdot\vec{n}) + \int_0^T \int_\Gamma A\nabla c \cdot \nabla v(\vec{V}\cdot\vec{n}) \\
&- \int_0^T \int_\Gamma c\vec{q}\cdot\nabla v(\vec{V}\cdot\vec{n}) + \int_0^T \int_{\Gamma_1} \alpha h'(c)c' \\
&+ \int_0^T \int_{\Gamma_1} H\alpha h(c)v(\vec{V}\cdot\vec{n}) + \int_0^T \int_{\Gamma_1} \frac{\partial(\alpha h(c)v)}{\partial n}(\vec{V}\cdot\vec{n}).
\end{aligned} \tag{2.5.7}$$

We have

$$\int_0^T \int_\Gamma A\nabla c \cdot \nabla v(\vec{V}\cdot\vec{n}) = \int_0^T \int_\Gamma \left(A\nabla_T c \cdot \nabla_T v + A\frac{\partial c}{\partial n}\frac{\partial v}{\partial n}\right)(\vec{V}\cdot\vec{n}), \tag{2.5.8}$$

where ∇_T is the tangential part of the gradient.
An integration by parts gives:

$$\int_\Gamma (A\nabla_T c \cdot \nabla_T v)(\vec{V}\cdot\vec{n}) = -\int_\Gamma A\nabla_T c \cdot \nabla_T(\vec{V}\cdot\vec{n})v - \int_\Gamma A\Delta_T c(\vec{V}\cdot\vec{n})v, \tag{2.5.9}$$

where $\Delta_T c = \mathrm{div}_T(\nabla_T c)$ is the Laplace-Beltrami operator.
Now, using [28, Prop. 5.4.12 p. 196] we have

$$\begin{aligned}
A\Delta_\Gamma c &= A\Delta c - AH\frac{\partial c}{\partial n} - A\frac{\partial^2 c}{\partial n^2} \\
&= \partial_t(\theta c + \varphi(c)) + \nabla.(\vec{q}c) - AH\frac{\partial c}{\partial n} - A\frac{\partial^2 c}{\partial n^2}.
\end{aligned} \tag{2.5.10}$$

Then (2.5.7) reads

$$\begin{aligned}
&-\int_0^T\int_\Gamma A\frac{\partial c'}{\partial n}v - c'v\vec{q}\cdot\vec{n} = -\int_0^T\int_\Gamma A\nabla_T c\cdot\nabla_T(\vec{V}\cdot\vec{n})v\\
&-\int_0^T\int_\Gamma\left(\nabla.(\vec{q}c) - AH\frac{\partial c}{\partial n} - A\frac{\partial^2 c}{\partial n^2}\right)(\vec{V}\cdot\vec{n})v + \int_0^T\int_\Gamma A\frac{\partial c}{\partial n}\frac{\partial v}{\partial n}(\vec{V}\cdot\vec{n})\\
&-\int_0^T\int_\Gamma c\vec{q}\cdot\nabla_T v(\vec{V}\cdot\vec{n}) - \int_0^T\int_\Gamma c\vec{q}\cdot\vec{n}\frac{\partial v}{\partial n}(\vec{V}\cdot\vec{n})\\
&+\int_0^T\int_{\Gamma_1}\alpha h'(c)c'v + \int_0^T\int_{\Gamma_1} H\alpha h(c)v(\vec{V}\cdot\vec{n}) + \int_0^T\int_{\Gamma_1}\frac{\partial(\alpha h(c)v)}{\partial n}(\vec{V}\cdot\vec{n}).
\end{aligned}\tag{2.5.11}$$

Moreover, since

$$\begin{aligned}
-\int_\Gamma c\vec{q}\cdot\nabla_T v(\vec{V}\cdot\vec{n}) &= -\int_\Gamma \mathrm{div}_T(\vec{q}c(\vec{V}\cdot\vec{n})v) + \int_\Gamma \mathrm{div}_T(\vec{q}c(\vec{V}\cdot\vec{n}))v\\
&= -\int_\Gamma H\vec{q}\cdot\vec{n}c(\vec{V}\cdot\vec{n})v + \int_\Gamma \mathrm{div}_T(\vec{q}c(\vec{V}\cdot\vec{n}))v,
\end{aligned}\tag{2.5.12}$$

we can see by using the boundary conditions verified by c that

$$\int_0^T\int_\Gamma(\vec{V}\cdot\vec{n})\left(Hv+\frac{\partial v}{\partial n}\right)\left(A\frac{\partial c}{\partial n} - c\vec{q}\cdot\vec{n}\right) + \int_0^T\int_{\Gamma_1}(\vec{V}\cdot\vec{n})\left(Hv+\frac{\partial v}{\partial n}\right)\alpha h(c) = 0.\tag{2.5.13}$$

After using this simplification, (2.5.11) reads

$$\begin{aligned}
&-\int_0^T\int_\Gamma A\frac{\partial c'}{\partial n}v - c'v\vec{q}\cdot\vec{n} = -\int_0^T\int_\Gamma A\nabla_T c\cdot\nabla_T(\vec{V}\cdot\vec{n})v\\
&-\int_0^T\int_\Gamma\left(\nabla.(\vec{q}c) - A\frac{\partial^2 c}{\partial n^2}\right)(\vec{V}\cdot\vec{n})v + \int_\Gamma \mathrm{div}_T(\vec{q}c(\vec{V}\cdot\vec{n}))v\\
&+\int_0^T\int_{\Gamma_1}\alpha h'(c)c'v + \int_0^T\int_{\Gamma_1}\frac{\partial(\alpha h(c))}{\partial n}v(\vec{V}\cdot\vec{n}),
\end{aligned}\tag{2.5.14}$$

from which we can deduce the boundary conditions for c'.
Finally, the equation satisfied by c' is

$$\frac{\partial}{\partial t}\big(\theta c' + \varphi'(c)c'\big) - A\Delta c' + \vec{q}\cdot\nabla c' = 0 \quad \text{in} \quad Q,\tag{2.5.15}$$

with boundary conditions

$$\begin{cases}
A\frac{\partial c'}{\partial n} - c'\vec{q}\cdot\vec{n} + \alpha h'(c)c' = \big(-A\frac{\partial^2 c}{\partial n^2} - \frac{\partial(\alpha h(c))}{\partial n} + \vec{q}\cdot\nabla c\big)(\vec{V}\cdot\vec{n})\\
+A\nabla_T(\vec{V}\cdot\vec{n})\cdot\nabla_T c - \nabla_T(c\vec{V}\cdot\vec{n})\cdot\vec{q} \quad \text{on} \quad I\times\Gamma_1,\\
A\frac{\partial c'}{\partial n} - c'\vec{q}\cdot\vec{n} = \big(-A\frac{\partial^2 c}{\partial n^2} + \vec{q}\cdot\nabla c\big)(\vec{V}\cdot\vec{n})\\
+A\nabla_T(\vec{V}\cdot\vec{n})\cdot\nabla_T c - \nabla_T(c\vec{V}\cdot\vec{n})\cdot\vec{q} \quad \text{on} \quad I\times\Gamma_2,
\end{cases}\tag{2.5.16}$$

and initial value

$$c'(0,x) = 0.\tag{2.5.17}$$

In order to get rid of the shape derivative c' (which we would have to compute for every choice of $\vec{V}$) in the expression of dJ (2.5.3), we use the adjoint state technique. Let us introduce p the solution to the following adjoint state problem:

$$\begin{cases} -(\theta+\varphi'(c))\partial_t p - \nabla.(A\nabla p) - \vec{q}\cdot\nabla p = 0 & \text{in } Q, \\ (A\nabla p)\cdot\vec{n} + \alpha h'(c)p = \alpha h'(c) & \text{on } I\times\Gamma_1, \\ (A\nabla p)\cdot\vec{n} = 0 & \text{on } I\times\Gamma_2, \\ p(T,x) = 0 & \text{in } \Omega. \end{cases} \tag{2.5.18}$$

See for example [20, Theorem 2 p. 144] for existence of a solution to this problem.

The only integral we need to get rid of in (2.5.3) is

$$\mathcal{I} := \int_0^T \int_{\Gamma_1} \alpha h'(c)c'. \tag{2.5.19}$$

Using the boundary conditions satisfied by p, we have

$$\mathcal{I} = \int_0^T \int_{\Gamma_1} \alpha h'(c)c'p + \int_0^T \int_{\Gamma} c'(A\nabla p)\cdot\vec{n}. \tag{2.5.20}$$

Integrations by parts give

$$\mathcal{I} = \int_0^T \int_{\Gamma_1} \alpha h'(c)c'p + \int_0^T \int_{\Omega} c'A\Delta p - pA\Delta c' + \int_0^T \int_{\Gamma} Ap\nabla c'\cdot\vec{n}. \tag{2.5.21}$$

From the equations in c' and p, we have

$$\partial_t[c'p(\theta+\varphi'(c))] + c'A\Delta p - pA\Delta c' + \vec{q}\cdot\nabla(c'p) = 0, \tag{2.5.22}$$

which after integration gives

$$\int_0^T \int_{\Omega} c'A\Delta p - pA\Delta c' = -\int_0^T \int_{\Gamma} c'p\vec{q}\cdot\vec{n}. \tag{2.5.23}$$

We deduce

$$\mathcal{I} = \int_0^T \int_{\Gamma_1} \alpha h'(c)c'p + \int_0^T \int_{\Gamma} Ap\nabla c'\cdot\vec{n} - c'p\vec{q}\cdot\vec{n}. \tag{2.5.24}$$

Using the boundary conditions satisfied by c' given by (2.5.16), we obtain

$$\begin{aligned} \mathcal{I} = &\int_0^T \int_{\Gamma} p\left(\big(-A\frac{\partial^2 c}{\partial n^2} + \vec{q}\cdot\nabla c\big)(\vec{V}\cdot\vec{n}) + A\nabla_T(\vec{V}\cdot\vec{n})\cdot\nabla_T c - \nabla_T(c\vec{V}\cdot\vec{n})\cdot\vec{q}\right) \\ &- \int_0^T \int_{\Gamma_1} p\frac{\partial(\alpha h(c))}{\partial n}(\vec{V}\cdot\vec{n}). \end{aligned} \tag{2.5.25}$$

Integrations by parts lead to

$$\begin{aligned}\mathcal{J} = &\int_0^T \int_\Gamma \left(p\big(-A\frac{\partial^2 c}{\partial n^2} + \vec{q}\cdot\nabla c\big) - \mathrm{div}_T(pA\nabla_T c) + c\,\mathrm{div}_T(p\vec{q})\right)(\vec{V}\cdot\vec{n}) \\ &- \int_0^T \int_{\Gamma_1} p\frac{\partial(\alpha h(c))}{\partial n}(\vec{V}\cdot\vec{n}).\end{aligned} \tag{2.5.26}$$

Note that the shape gradient dJ is now expressed in the following convenient way:

$$dJ(c,\vec{V}) = \int_\Gamma j(\vec{V}\cdot\vec{n}),$$

where j does not depend on $\vec{V}$.

With that in mind, a simple yet effective approach to maximize J consists in choosing $\vec{V}$ such that $\vec{V}\cdot\vec{n} = j$, i.e. $\vec{V} = j\vec{n}$. This brings

$$dJ(c,\vec{V}) = \int_\Gamma j^2 > 0,$$

which ensures that J increases as the domain is iteratively deformed.

Note that this method restricts the choice of the deformation, as $\vec{\vec{V}}$ is taken colinear with $\vec{n}$.

From a numerical point of view, we still need to transform the expression of j in order to avoid numerical computations of second order derivatives. We have

$$-\,\mathrm{div}_T(pA\nabla_T c) = -A\nabla p\nabla_T c - pA\Delta_T c. \tag{2.5.27}$$

Using [28, Prop. 5.4.12 p. 196] again as in (2.5.10) yields

$$-\,\mathrm{div}_T(pA\nabla_T c) = -A\nabla p\nabla_T c - p\left(\partial_t(\theta c + \varphi(c)) + \nabla.(\vec{q}c) - AH\frac{\partial c}{\partial n} - A\frac{\partial^2 c}{\partial n^2}\right). \tag{2.5.28}$$

Finally, using (2.5.28) in (2.5.26), we can express $dJ(c,\vec{V})$ as

$$\begin{aligned}dJ(c,\vec{V}) &= \mathcal{J} + \int_0^T \left(\int_{\Gamma_1} \alpha Hh(c)(\vec{V}\cdot\vec{n}) + \int_{\Gamma_1} \frac{\partial(\alpha h(c))}{\partial n}(\vec{V}\cdot\vec{n})\right) \\ &= \int_0^T \int_\Gamma \left(-A\nabla p\nabla_T c - (\partial_t(\theta c + \varphi(c))p + pAH\frac{\partial c}{\partial n} + c\nabla_T p\cdot\vec{q}\right)(\vec{V}\cdot\vec{n}) \\ &\quad + \int_0^T \int_{\Gamma_1} \left(-p\frac{\partial(\alpha h(c))}{\partial n} + \alpha Hh(c) + \frac{\partial(\alpha h(c))}{\partial n}\right)(\vec{V}\cdot\vec{n}).\end{aligned} \tag{2.5.29}$$

Numerical resolution of the state and adjoint equations in two spatial dimensions is carried out using the free finite element software FreeFEM++ [27]. Spatial discretization is done using Lagrange P2 finite elements.

The backward Euler method is applied for the discretization in time. Nonlinearities in

the state equation are handled by Newton's method. A built-in adaptive anisotropic mesh refinement algorithm is used in order to improve accuracy near the boundary while preserving an acceptable computational cost.
The constant volume constraint is enforced by a Lagrange multiplier. Additionally, a minimum diameter constraint is put on the shape in order to prevent unsuitable deformations of the domain.

Numerical values used in this example are as follows:

— $c^0 = 2.9 \times 10^{-3}$ µmol cm^{-3},

— $F_m = 0.282$ µmol cm^{-2} d^{-1}, $K_m = 5.8 \times 10^{-3}$ µmol cm^{-3},

— $\kappa = 6.15$, $b = 0.72$,

— $\theta = 0.35$ cm^3 cm^{-3},

— $A = 0.102$ cm^2 d^{-1},

— $\vec{q} = 0, R = 0$.

— The initial shape is an ellipse of diameters 1.33 cm and 2.66 cm.

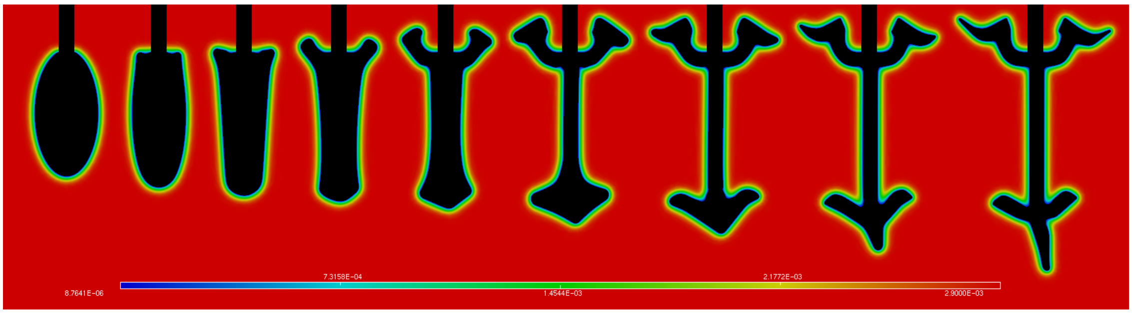

Figure 2.2 Snapshots of the domain and P concentration at different steps of the shape optimization process

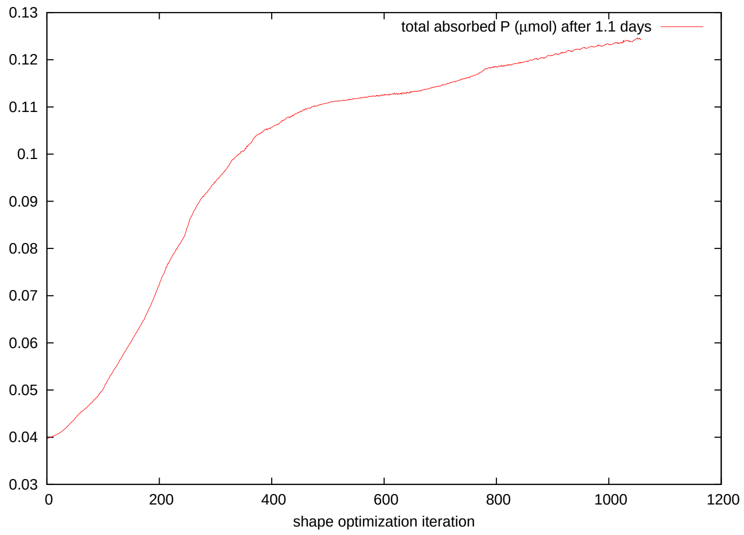

Figure 2.3 Evolution of the total amount of absorbed P during the optimization process

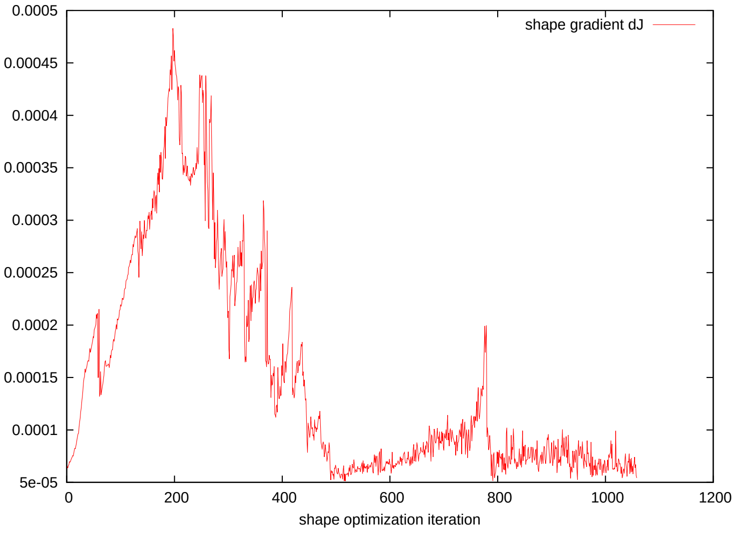

Figure 2.4 Evolution of the shape gradient dJ during the optimization process

In order to make sure that the boundary is not deformed in the region of the root collar where $0 \leq \alpha < 1$ as well as to enforce the minimum diameter constraint, the deformation field $\vec{V} = j\vec{n}$ is locally modified so as to vanish where the perturbed shape breaks these constraints. This is achieved by multiplying $\vec{V}$ by $C^\infty(\mathbb{R}^d)$ cutoff functions taking values in $[0,1]$ whose supports do not intersect the critical regions. This puts more and more restrictions on $\vec{V}$ as the shape evolves from the initial elliptic shape and causes the decrease of the shape gradient from iteration 200 to iteration 500 as we can see in figure

2.4. After iteration 500, the diameter constraint inhibits the optimization process. We observe residual oscillations of the shape gradient and the computed shapes become less and less significant. We show the whole process here for the record nonetheless.

2.6 Conclusion

In this chapter, we studied the well-posedness of a mathematical model of phosphorus uptake by plant roots, governed by a quasilinear convection-diffusion equation with a nonlinear boundary condition. We proved existence and uniqueness of solutions to the problem in Hölder spaces, assuming sufficient regularity of the data.

Then, we formulated a shape optimization problem to increase the amount of absorbed phosphorus by changing the shape of the root. The sensitivity analysis was performed using classical tools of shape optimization. The adjoint method was used to produce a gradient ascent algorithm in order to maximize the objective function.

A numerical example in two spatial dimensions with an elliptical initial shape was presented. This example shows that maximizing root surface area to volume ratio is indeed an essential component of root uptake efficiency. The resulting shape is evocative of the branching structure of plant root systems.

Chapter 3

Finite element model of soil water and nutrient transport with root uptake

The content of this chapter is included in [76].

Contents

3.1 Introduction

Numerous models have been developed in the past in order to adress the different spatial and temporal scales relevant to soil water and nutrient transport and uptake by plant roots, from crop models used to predict yields at the field level to recent plant based models involving the explicit architectural description of root system development.

Spatially explicit models defining 3D plant architecture are designed to investigate the relationship between root architectural traits and the spatio-temporal variability of resource supply. They are providing insights for understanding various root-soil interactions over a range of spatial scales and aid in the design of agricultural management schemes for improving plant performance in specific environments.

However, simulation of water and nutrient uptake is challenging especially if we consider spatial heterogeneities and local soil conditions in the rhizosphere around the roots, which are often quite different from those in the bulk soil. In addition, the efficiency of yield enhancement techniques depends on responsive root growth which allows plants to forage with precision in an heterogeneous environment.

In this chapter we attempt to include and resolve accurately local rhizosphere processes occurring at the individual root level in explicit plant scale models by taking advantage of the recent advances of scientific computing in the field of adaptive meshing and parallel computing.

The mechanistic model described here can be used to investigate plant-soil relationships in specific situations through for example sensitivity analysis, as well as verifying hypotheses and simplifications that are made in other models.

The model is comparable to [14, 36] where a discretization technique based on regular grids is employed. In such models, soil-root fluxes are taken into account in soil voxels by averaging and distributing between the soil nodes. In this work, we develop a new approach that takes advantage of the flexibility of adaptive refinement of unstructured finite element meshes to resolve small-scale behaviours such as the local hydraulic conductivity drop near the soil-root interface while retaining the simplicity of the standard finite element method. Adaptive unstructured volume remeshing is quite a powerful tool when considering complex structures such as plant root systems.

The chapter is organized as follows: section 3.2 describes our water model. We consider that the root system can be represented as a tree-like network composed of cylindrical root segments. We then define radial and axial water flows on this network that can be coupled to the soil model via a sink term in the Richards equation. The sink term is constructed upon a characteristic function representative of the geometry of the root system. In section 3.3, the nutrient model is presented in a similar way. Section 3.4 briefly describes the standard finite element method used in this work. In section 3.5, the adaptive mesh refinement algorithm is presented: the characteristic function of the root system is computed and then used to construct a metric field in order to drive the mesh adaptation procedure. Since such an approach is computationally intensive, a parallelization technique based on a scalable Schwarz domain decomposition method is used to solve the problems arising from the soil and nutrient models. The procedure is highlighted in section 3.6.

Throughout this chapter the soil domain is denoted by $\Omega \subset \mathbb{R}^d (d = 2,3)$. We consider the evolution of the water potential and nutrient concentration for $t \in [0,T], T > 0$.

3.2 The water model

3.2.1 Richards equation

In soils, water movement is governed by the Richards equation. Richards equation is derived from the continuity equation

$$\frac{\partial \theta}{\partial t} + \nabla . q = S, \tag{3.2.1}$$

with θ the volumetric water content, q the macroscopic Darcy flow and S representing sources/sinks.
Darcy law relates the water flow to the pressure of the water at any time t:

$$q = -K \nabla H, \tag{3.2.2}$$

where K is the hydraulic conductivity and H is the total hydraulic head (water potential on weight basis), which can be expressed as

$$H = h + z. \tag{3.2.3}$$

Here, h is the pressure head and comes from a hydrostatic pressure if $h > 0$ and from a capillary pressure if $h < 0$. z is the height against the gravitational direction.

The volumetric water content θ and the hydraulic conductivity K are linked to the pressure head h by relationships that depend on the soil properties.

By combining (3.2.1) and (3.2.2) we obtain the Richards equation:

$$\partial_t(\theta(h)) - \nabla.(K(h)\nabla(h+z)) = S \quad \text{in} \quad [0,T] \times \Omega. \tag{3.2.4}$$

Equation (3.2.4) is subject to the initial condition

$$h(x,0) = h_0(x) \quad \text{in} \quad \Omega, \tag{3.2.5}$$

and the no-flux boundary condition

$$K(h)\nabla(h+z).\vec{n} = 0 \quad \text{on} \quad [0,T] \times \partial\Omega, \tag{3.2.6}$$

where $\vec{n}$ denotes the unit outward normal to the boundary of the domain Ω.

The $\theta(h)$ and $K(h)$ relationships are given by empirical models whose parameters depend on the soil physical properties. We use the Brooks-Corey model:

$$\begin{aligned} \Theta(h) &:= \frac{\theta(h) - \theta_m}{\theta_M - \theta_m} = \left[\frac{h}{h_b}\right]^{-\lambda} := \begin{cases} \left(\frac{h}{h_b}\right)^{-\lambda} & \text{for} \quad h \leq h_b \\ 1 & \text{for} \quad h \geq h_b, \end{cases} \\ K(h) &= K_s \left[\frac{h}{h_b}\right]^{-\lambda e(\lambda)} \qquad \text{with } e(\lambda) := 3 + \frac{2}{\lambda}, \end{aligned} \tag{3.2.7}$$

where Θ is the normalized water content.
The parameters of the model are defined as follows:

— θ_M is the saturated water content.
— θ_m is the residual water content.
— K_s is the saturated hydraulic conductivity.
— h_b is the bubbling pressure head.
— λ is the pore size distribution index.

Experimental evidence has shown that a cycle of wetting-drying of a soil exhibits hysteresis: the water content has different profiles with respect to the wetting and draining processes. This effect can be of importance when considering irrigation or rainfall together with root water uptake. Although hysteresis effects are neglected in the model described here, hysteresis in the soil water retention function $\theta(h)$ can be taken into account by including empirical hysteresis models such as [41] based on main wetting and drying curves.

We introduce the Kirchhoff transformation κ which enables us to reduce the nonlinearity of Richards equation:

$$\kappa : h \to p \int_0^h K(p)dp. \tag{3.2.8}$$

The new variable p is called the generalized pressure. Previous applications of the Kirchhoff transformation to Richards equation can be found for example in [59, 79, 37, 72].
The water content as a function of p is denoted by

$$M(p) := \theta(\kappa^{-1}(p)). \tag{3.2.9}$$

Using the chain rule, we have

$$\nabla p = K(h)\nabla(h). \tag{3.2.10}$$

Thus the Richards equation reads:

$$\partial_t(M(p)) - \nabla.(\nabla p + K(\kappa^{-1}(p))\nabla z) - S = 0 \quad \text{in} \quad [0,T] \times \Omega. \tag{3.2.11}$$

The transformed equation is a semilinear equation in which the nonlinearity in front of the spatial derivative has been eliminated.

Using the backward Euler scheme for the time discretization, we are able to write the following weak formulation of the semi-discrete problem: find $p^{n+1} \in H^1(\Omega)$ such that $\forall v \in H^1(\Omega)$,

$$\int_\Omega \frac{M(p^{n+1}) - M(p^n)}{\Delta t} v + \int_\Omega \nabla p^{n+1} \nabla v + \int_\Omega K(\kappa^{-1}(p^{n+1}))\nabla z \nabla v - \int_\Omega Sv = 0. \tag{3.2.12}$$

Following the approach suggested in [6, 72], the solution at each time step is obtained iteratively; applying Newton's method to linearize $M(p^{n+1})$ gives the following Newton-like iteration where i is the inner iteration counter for time $n+1$:

$$\int_\Omega \frac{M'(p^i)(p^{i+1}-p^i)+M(p^i)-M(p^n)}{\Delta t} v + \int_\Omega \nabla p^{i+1} \nabla v + \int_\Omega K(\kappa^{-1}(p^i)) \nabla z \nabla v - \int_\Omega S v = 0. \tag{3.2.13}$$

In practice, as the soil dries the capillary effects get stronger as well as the nonlinearities, while the gravity term becomes of less importance. This allows us to use a simple picard method for the gravity term with no effect on the convergence rate.

The use of the Brooks-Corey model allows us to express the Kirchhoff transformation and its inverse and the transformed functions involved in (3.2.13) explicitly in a closed form as in [5]:

$$\begin{aligned}
p = \kappa(h) &= \begin{cases} \frac{h_b}{-\lambda e(\lambda)+1}\left(\frac{h}{h_b}\right)^{-\lambda e(\lambda)+1} + \frac{-\lambda e(\lambda) h_b}{-\lambda e(\lambda)+1} & \text{for} \quad h \le h_b \\ h & \text{for} \quad h \ge h_b, \end{cases} \\
h = \kappa^{-1}(p) &= \begin{cases} h_b \left(\frac{p(-\lambda e(\lambda)+1)}{h_b} + \lambda e(\lambda)\right)^{\frac{1}{-\lambda e(\lambda)+1}} & \text{for} \quad p_c < p \le h_b \\ p & \text{for} \quad p \ge h_b, \end{cases} \\
M(p) &= \begin{cases} \theta_m + (\theta_M - \theta_m)\left(\frac{p(-\lambda e(\lambda)+1)}{h_b} + \lambda e(\lambda)\right)^{\frac{\lambda}{\lambda e(\lambda)-1}} & \text{for} \quad p_c < p \le h_b \\ \theta_M & \text{for} \quad p \ge h_b, \end{cases} \\
M'(p) &= \begin{cases} (\theta_M - \theta_m)\frac{-\lambda}{h_b}\left(\frac{p(-\lambda e(\lambda)+1)}{h_b} + \lambda e(\lambda)\right)^{\frac{\lambda}{\lambda e(\lambda)-1}-1} & \text{for} \quad p_c < p \le h_b \\ 0 & \text{for} \quad p \ge h_b, \end{cases} \\
K(\kappa^{-1}(p)) &= \begin{cases} \left(\frac{p(-\lambda e(\lambda)+1)}{h_b} + \lambda e(\lambda)\right)^{\frac{\lambda e(\lambda)}{\lambda e(\lambda)-1}} & \text{for} \quad p_c < p \le h_b \\ 1 & \text{for} \quad p \ge h_b, \end{cases}
\end{aligned} \tag{3.2.14}$$

Since the transformations (3.2.14) are obtained analytically, the additional computational cost of employing the Kirchhoff transformation is negligible compared to that of solving the linear system arising from the discretization of (3.2.13).

Note that the discontinuity of $M'(p)$ for $p = h_b$ comes from the non-differentiability of the Brooks-Corey function $\theta(h)$ at $h = h_b$. However, we do not consider the saturated case $h \ge h_b$ in the examples presented in this chapter. Besides, from a numerical point of view, numerical tests have shown that for realistic parameter values the discontinuity is small and does not hinder the convergence of the iterative method.

3.2.2 Root water uptake

Here we consider that the root system is composed of cylindrical root segments. It can then be represented as a series of interconnected nodes forming a network of segments Σ, each segment with its own parameters (radius, conductivity, etc.). Such a representation can be generated by the Matlab code RootBox [46], which implements a root system growth model based on L-Systems. RootBox is a root architectural model that explicitly simulates the architecture of root systems in the 3D space, using a set of growth rules which are applied to a series of root types or classes, with each root type having its own characteristic set of growth parameters such as root elongation rate or branching density. The algorithm computes elongation and branching of the roots according to the initial growth speed, lengths of apical and basal zones as well as internodal distances, maximal number of branches and branching angles. Growth direction can follow different types of user defined tropisms. The model has a stochastic component in that all parameters can be given with mean and standard deviation. Fig. 3.1 shows an example of a maize root system generated by RootBox.

Figure 3.1 Example of a 20-days-old maize root system generated by RootBox composed of 10611 segments

In the following we define water flows on the root network and describe the coupling with the soil model as was done in [14].

We make the same assumptions as in [14], which are explained in [13]. The model describing root water uptake can be found in [18, 45]: water flow in roots and between soil and roots is described by the transpiration-cohesion-tension mechanism and follows an Ohm's law analogy.
Let us recall the hypotheses made in [13]: First, the influence of solutes on flow is neglected, because during periods of active transpiration, the hydrostatic pressure gradient rather than the osmotic potential gradient is the effective driving force for flow. The second hypothesis consists in neglecting the capacitive effect of the roots and considering only steady-state flow, because water stored in roots is generally small compared to transpiration requirements. Thus, for a cylindrical root segment of radius r and length l and following [45], we can define the volumetric radial water flow into the root from the soil J_r and the longitudinal flow up the root in the xylem J_x as

$$\begin{aligned} J_r &= L_r s_r (h_s - h_r), \\ J_x &= -K_x \frac{d(h_r + z)}{dl}, \end{aligned} \tag{3.2.15}$$

where

- — L_r is the radial conductivity of the root and represents the conductivity of the series of tissues from the root surface to the xylem,
- — K_x is the xylem conductance,
- — $s_r = 2\pi r l$ is the root-soil interface area,
- — h_s is the soil water potential at the root surface,
- — h_r is the water potential in the xylem.

Although these simplifications are made in our model as well, the model can be extended by taking into account osmotic gradients and capacitive effects of roots.

Equations (3.2.15) giving radial and longitudinal flows can be used to formulate a water mass balance equation for a given root node i of parent node p in the tree-like structure as depicted in Fig. 3.2:

$$J_{x,i} = \sum_{j \in \text{childs}(i)} J_{x,j} + J_{r,i}, \tag{3.2.16}$$

which can be written as

$$\begin{aligned} -K_{x,i}\frac{(h_{r,p}+z_p)-(h_{r,i}+z_i)}{l_i} &= -\sum_{j \in \text{childs}(i)} K_{x,j}\frac{(h_{r,i}+z_i)-(h_{r,j}+z_j)}{l_j} \\ &\quad + L_{r,i} 2\pi r_i l_i \frac{(h_{s,i}-h_{r,i})+(h_{s,p}-h_{r,p})}{2}. \end{aligned} \tag{3.2.17}$$

Here $K_{x,i}, L_{r,i}, r_i$ and l_i refer to the root segment (p,i) while $K_{x,j}$ and l_j relate to the root segment (i,j). $h_{s,i}$ and $h_{r,i}$ are the soil water potential at root node i and the xylem water potential at root node i respectively. We approximate the potentials h_s and h_r for segment (i,p) by averaging their value at the two nodes i and p. Parameters L_r and K_x are given for each segment and can depend on various data such as root type and age.

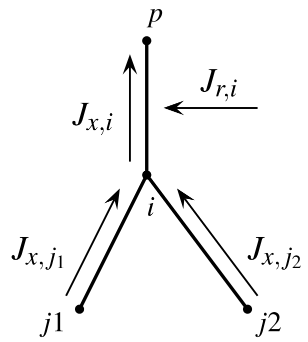

Figure 3.2 Water mass balance for root node i

Writing (3.2.17) for every node in the tree-like structure, the xylem water potential vector $(h_{r,i})_i$ is then solution of a linear system, with the right-hand side containing the soil factors represented by the $h_{s,i}$.
At the root collar, we can prescribe the transpiration flow or the xylem potential with a Neumann or Dirichlet boundary condition respectively. We can follow the same approach as in [14, 36]: In the case of a flux-type boundary condition, stress may occur when the evaporative demand cannot be met by the soil. In such a case, a maximum allowable threshold value for absolute collar water potential is defined (usually taken as a typical value of the permanent wilting point $h_w = -150$ m), beyond which the collar boundary condition is switched from a flux-type (Neumann) to a pressure-head-type (Dirichlet) condition.
Other models could also be considered, such as [77] where stomatal response to a drying soil is modeled by a logistic function with empirically determined parameters.

In order to take the radial water uptake flows into account in the soil water model, a sink term S in the Richards equation is defined in the domain. Since the sink term represents root uptake flows in the 3D (or 2D) space, we construct S through a characteristic function of the root system f_c representative of its geometry using the distance function to the root network Σ. The characteristic function f_c can be seen as a smooth approximation of the 1D root network Σ, taking the values 1 at the root and 0 away from the root, with a smooth change of width ε in between.
The purpose of the characteristic function is threefold: define a regularization of the delta function representing the network of segments Σ, construct a sink term matching the volume occupied by the roots by using the diameter of the root as the width of the regularization, and drive the adaptive mesh refinement procedure.

The function f_c representative of the geometry of the root system in the domain is constructed as follows:

— For a point x of the domain Ω the distance d from x to the root is computed:

$$d(x) = \min_{s \in \Sigma} d_s(x), \tag{3.2.18}$$

with Σ the set of root segments in the tree-like network. For each root segment s, the distance $d_s(x)$ from the point x to the segment s is easily computed using distance from line and point routines.

— The distance function d is then used to compute the characteristic function. There is a variety of admissible transformations that we can use, and we choose the following:

$$f_c(x) = f_d(d(x)) = 1 - \tanh\left(\frac{6d(x)}{\varepsilon}\right). \tag{3.2.19}$$

We can choose ε to be equal to the radius of the root.

We can now build the sink term in the Richards equation. In order to ensure that the sink term in the soil model corresponds to the volumetric radial flow in the network model, we need to introduce a scale factor depending on the choice of f_d.

Let us consider the case of a cylindrical root segment s, formed by the nodes i and j. The corresponding radial flow is

$$J_r = L_r 2\pi r_r l_r \frac{(h_{s,i} - h_{r,i}) + (h_{s,j} - h_{r,j})}{2}. \tag{3.2.20}$$

We want the integral of the corresponding sink term S over the domain to be equal to the outflow rate, i.e.

$$\int_\Omega S = -J_r. \tag{3.2.21}$$

If f_c is the characteristic function of the single root segment as defined above, using cylindrical coordinates we get (in the 3D case)

$$\int_\Omega f_c \simeq 2\pi l_r \int_0^R r f_d(r) dr \tag{3.2.22}$$

with $R >> \varepsilon$. The approximation error coming from the truncature in the integral is negligible for usual choices of f_d.

Let us define Tr as

$$T_r = \int_0^R r f_d(r) dr. \tag{3.2.23}$$

We then define the sink term S as

$$S = -f_c \frac{L_r r_r}{T_r} h_l, \tag{3.2.24}$$

where h_l only depends on the longitudinal coordinate and linearly interpolates $h_s - h_r$ along the segment.
Thus, we have

$$\int_\Omega S = -\int_\Omega f_c \frac{L_r r_r}{T_r} h_l = -L_r 2\pi r_r l_r \frac{(h_{s,i} - h_{r,i}) + (h_{s,j} - h_{r,j})}{2} = -J_r. \tag{3.2.25}$$

The extension to the whole root system is straightforward.

Since the characteristic function does not correspond to an arrangement of perfect cylindrical root segments due to its shape at root tips or in-between root segments, a modified approach consists in adjusting the surface areas of the root segments in the definition of the radial uptake flows in the root network model so that for each root segment, the volumetric uptake flow is equal to the actual contribution of the segment to the global sink term in the soil model. This approach ensures that the amount of water depleted in the soil water model is equal to the transpiration rate in the network model, although the difference is minimal in actual computations.

The coupling between the tree-like model and the soil water model consists in iteratively solving the two problems until convergence. Let $h_s^{t_i}$ be the soil matric potential distribution at time t_i, h_s^k and h_r^k the soil and xylem matric potentials at inner iteration k and time t_{i+1}. The coupling algorithm reads as follows:

1. $h_s^0 = h_s^{t_i}$.
2. Solve the linear system of the tree-like model derived from (3.2.17) with soil factors h_s^k, obtain h_r^k on the root network.
3. Compute the sink term S as in (3.2.24) using h_s^k and h_r^k.
4. Perform an inner iteration of (3.2.13), obtain h_s in the soil domain.
5. $h_s^{k+1} = h_s^k + \alpha_k(h_s - h_s^k)$, where α_k is an under-relaxation parameter that ensures convergence of the system.
6. If $||h_s - h_s^k|| > \tau$, go to 2. with $k \leftarrow k+1$.

Fig. 3.3 gives an overview of the water model through an example.

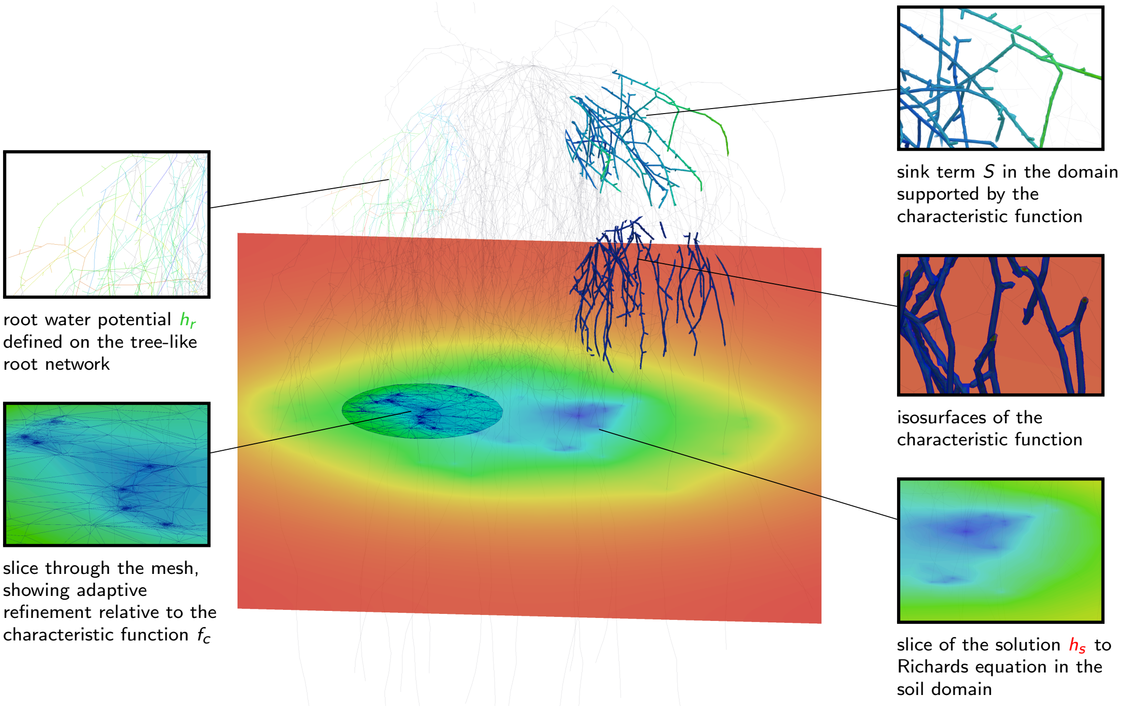

Figure 3.3 Overview of the water model

3.3 The nutrient model

Here we consider the evolution of the concentration c of a nutrient ion N in the soil solution, governed by diffusion, mass flow, adsorption in the soil solid phase and root uptake.

3.3.1 The convection-diffusion equation

The convection-diffusion equation expresses the nutrient mass balance and can be written in its conservative form:

$$\partial_t(\theta c + \varphi(c)) = \nabla.\big(A\nabla c - qc\big) + S_c(c) \quad \text{in} \quad [0,T] \times \Omega, \tag{3.3.1}$$

where

— A is the diffusion coefficient of N in the soil. For simplicity we consider a modified diffusion coefficient with a tortuosity factor in place of the effective dispersion coefficient tensor that is usually employed for flow in porous media, although the model can easily be extended to account for dispersibility since water flow is explicitly considered. Following [4], A is given by

$$A = A_0 \theta f_l, \tag{3.3.2}$$

with A_0 the diffusion coefficient of N in free water and f_l the so-called tortuosity factor:

$$f_l = \begin{cases} f_1\theta + f_2 & \text{for} \quad \theta \geq \theta_l, \\ \frac{\theta(f_1\theta_l + f_2)}{\theta_l} & \text{for} \quad \theta < \theta_l, \end{cases} \tag{3.3.3}$$

where f_1, f_2 and θ_l are parameters depending on soil properties.

— φ is an adsorption/desorption isotherm relating the amount of adsorbed N to the equilibrium concentration of N in solution; we use the Freundlich adsorption isotherm [54], defined by

$$\varphi(c) = \kappa c^b, \tag{3.3.4}$$

where $\kappa > 0$ and $b \in (0,1)$ are fitting parameters of the model,

— $S_c(c)$ represents sources/sinks.

Equation (3.3.1) is subject to the initial condition

$$c(x,0) = c_0(x) \quad \text{in} \quad \Omega, \tag{3.3.5}$$

and the no-flux boundary condition

$$\big(A\nabla c - qc\big).\vec{n} = 0 \quad \text{on} \quad [0,T] \times \partial\Omega. \tag{3.3.6}$$

The convective form of equation (3.3.1) is obtained by multiplying equation (3.2.1) by c and substracting it from equation (3.3.1). This gives

$$(\theta + \varphi'(c))\partial_t c = \nabla.\big(A\nabla c\big) - q.\nabla c - Sc + S_c(c). \tag{3.3.7}$$

Here $\theta + \varphi'(c)$ is the buffer power and represents the ability of the soil to resupply nutrients as plants take it up from the soil solution.
The Lagrangian form is derived by dividing by $\theta + \varphi'(c)$ and defining the material derivative

$$\frac{Dc}{Dt} = \partial_t c + \frac{q}{\theta + \varphi'(c)}.\nabla c. \tag{3.3.8}$$

We can use the method of characteristics to handle the convective part. The velocity field is $a = \frac{q}{\theta + \varphi'(c)}$.
Following [64], we can use the approach yielding (3.3.7) at the semi-discrete level to reduce mass balance errors. Using the implicit Euler scheme for the time discretization of (3.3.1) gives

$$\frac{\theta^{n+1}c^{n+1} + \varphi(c^{n+1}) - \theta^n c^n - \varphi(c^n)}{\Delta t} = \nabla.\big(A^{n+1}\nabla c^{n+1} - q^{n+1}c^{n+1}\big) + S_c(c^{n+1}). \tag{3.3.9}$$

Our implicit time discretization of Richards equation (3.2.12) corresponds to

$$\frac{\theta^{n+1} - \theta^n}{\Delta t} + \nabla.q^{n+1} = S^{n+1}. \tag{3.3.10}$$

Multiplying (3.3.10) by c^{n+1} and substracting it from (3.3.9), we are able to write the weak formulation of the semi-discrete problem: find $c^{n+1} \in H^1(\Omega)$ such that $\forall v \in H^1(\Omega)$,

$$\begin{aligned} &\int_\Omega \frac{\theta^n c^{n+1} + \varphi(c^{n+1}) - \theta^n c^n \circ X - \varphi(c^n \circ X)}{\Delta t} v + \int_\Omega A^{n+1} \nabla c^{n+1} \nabla v \\ &+ \int_\Omega S^{n+1} c^{n+1} v - \int_\Omega S_c(c^{n+1}) v = 0 \end{aligned} \tag{3.3.11}$$

with the approximated characteristics $X = x - \Delta t a$.
Applying Newton's method and denoting by i the inner iteration counter for time $n+1$, we get

$$\begin{aligned} &\int_\Omega \frac{\theta^n c^{i+1} + \varphi(c^i) + \varphi'(c^i)(c^{i+1} - c^i) - \theta^n c^n \circ X - \varphi(c^n \circ X)}{\Delta t} v + \int_\Omega A^{n+1} \nabla c^{i+1} \nabla v \\ &+ \int_\Omega S^{n+1} c^{i+1} v - \int_\Omega S_c(c^i) v - \int_\Omega S_c'(c^i)(c^{i+1} - c^i) v = 0. \end{aligned} \tag{3.3.12}$$

3.3.2 Nutrient uptake

Here we consider that the root acts as a selective membrane for ion uptake. Nutrient uptake by roots is given by a model of enzyme kinetics, relating in this case the root uptake rate of N to its concentration at the root surface. Here we use the following Michaelis-Menten model:

$$h(c) = \frac{F_m c}{K_m + c}, \tag{3.3.13}$$

where $h(c)$ is the uptake rate and $F_m, K_m > 0$ are parameters of the model.
This model of active nutrient uptake is taken from [3]. The hypothesis that active uptake becomes more important under low nutrient supply, while the transpiration driven mass flow dominates for higher concentrations, is proposed in [82].
For a cylindrical root segment of radius r and length l and assuming that the uptake flux at the root surface is given by (3.3.13), we can define the volumetric nutrient uptake rate by

$$J_N = 2\pi r l h(c_s), \tag{3.3.14}$$

where c_s is the concentration of N at the root surface.

Similarly to the sink term (3.2.24) in the Richards equation, the sink term S_c representing nutrient uptake in the convection-diffusion equation is constructed as follows:

$$S_c = -f_c \frac{r}{T_r} h(c). \tag{3.3.15}$$

The model can easily be adapted to implement other nutrient uptake models. For example, in [69, 35] the solute uptake term is defined as

$$S'(c) = \varepsilon S c + (1 - \varepsilon) S_c(c),$$

where $\varepsilon \in [0,1]$ is a coefficient partitioning total uptake between passive uptake Sc where solutes enter the root dissolved in water and active uptake $S_c(c)$, which could also be described following for example [40] by a Michaelis-Menten-type kinetic with a linear component.

3.4 Finite element formulation

In this section we briefly describe the Galerkin P1 finite element approximation of problems (3.2.13) and (3.3.12).
Let T_h be a mesh of the domain Ω. Let

$$V_h = \left\{ u_h \in H^1(\Omega) \,\middle|\, u_h|_K \in P_1,\ \forall K \in T_h \right\}. \tag{3.4.1}$$

Spatial discretization of Equation (3.2.13) leads to the following discrete variational problem: find $p_h \in V_h$ such that $\forall v_h \in V_h$,

$$\begin{aligned}\left(M'(p_h^i)p_h, v_h\right) + \Delta t\,(\nabla p_h, \nabla v_h) = \left(M'(p_h^i)p_h^i, v_h\right) - \left(M(p_h^i), v_h\right) + (M(p_h^n), v_h)\\ - \left(K(\kappa^{-1}(p_h^i))\nabla z, \nabla v_h\right) + \left(S_h^i, v_h\right).\end{aligned} \tag{3.4.2}$$

Spatial discretization of Equation (3.3.12) leads to the following discrete variational problem: find $c_h \in V_h$ such that $\forall v_h \in V_h$,

$$\begin{aligned}&(\theta_h^n c_h, v_h) + \left(\varphi'(c_h^i)c_h, v_h\right) + \left(A_h^{n+1}\nabla c_h, \nabla v_h\right) + \Delta t\left(S_h^{n+1} c_h, v_h\right) - \Delta t\left(S_c'(c^i)_h c_h, v_h\right)\\ &= -\left(\varphi(c_h^i), v_h\right) + \left(\varphi'(c_h^i)c_h^i, v_h\right) + (\theta_h^n c_h^n \circ X, v_h) + (\varphi(c_h^n \circ X), v_h)\\ &+ \Delta t\left(S_c(c^i)_h, v_h\right) - \Delta t\left(S_c'(c^i)_h c_h^i, v_h\right).\end{aligned} \tag{3.4.3}$$

Numerical resolution of problems (3.4.2) and (3.4.3) is carried out using the finite element software FreeFem++ [27].

3.5 Mesh adaptation

The soil domain Ω is first represented by a regular initial simplicial finite element mesh. Since the characteristic function of the root system f_c is poorly represented on the initial mesh, we refine it iteratively using anisotropic mesh adaptation. Since we expect high gradients and small-scale phenomena to be localized near the roots (i.e. where f_c exhibits strong variations), this type of a priori refinement is adequate.
The main steps of the adaptive procedure are as follows: First, we compute f_c for each node of the mesh. Then we define a nodal based anisotropic metric from the Hessian of the function f_c. Finally, the mesh is adapted using the size and streching of elements provided by the metric. This procedure is repeated iteratively.
The metric-based mesh adaptation procedure is described in more details in chapter 4.

In 2D, we use the built-in adaptive remesher of FreeFem++. For 3D simulations, FreeFem++ is interfaced with the `mshmet` library [19] for computing the Hessian-based anisotropic metric and with the anisotropic fully tetrahedral automatic remesher Mmg3d [12] which uses anisotropic Delaunay kernel and local mesh modifications based on a combination of edge flips, edge collapsing, node relocation and vertex insertion operations to adapt the mesh.

Fig. 3.4 illustrates the mesh adaptation process in a 2D simulation.

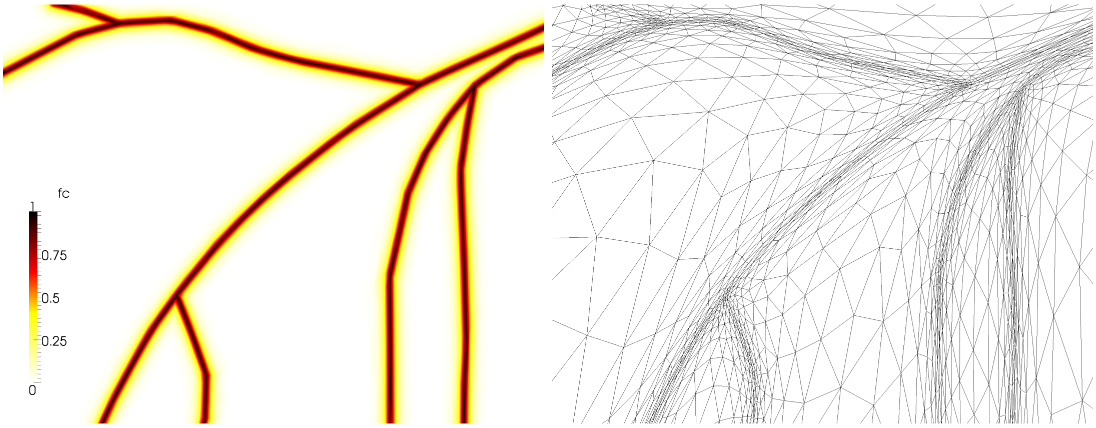

Figure 3.4 2D example of the mesh adaptation process: representation of the function f_c (left) defined on the adapted mesh (right)

3.6 Domain decomposition

Sinces meshes generated as described in section 3.5 require a considerable number of nodes to be able to adequately resolve the geometry of complex root systems, linear systems resulting from the discrete problems (3.4.2) and (3.4.3) can be quite large. In order to reduce computation time, we opted for a parallel divide-and-conquer technique with an additive Schwartz overlapping domain decomposition method.

The initial computational domain is partitioned by metis [39] into a number of subdomains, on which local variational problems are defined. A two-level coarse grid preconditioner taken from [38] is also used to improve the convergence of the domain decomposition method.

Numerical tests are conducted in 2D and in 3D in order to assess the efficiency of the two-level preconditioner compared to a classical one-level preconditioner. We consider one inner iteration of (3.4.2). In the 2D case, the mesh is composed of 204 331 vertices and 407 839 triangles. The 3D mesh is composed of 2 673 103 vertices and 15 273 475 tetrahedra. Numerical tests are performed on the SGI Altix UV100 computer at Laboratoire Jacques-Louis Lions. Results are outlined in Table 3.5.

There are several iterative algorithms used to obtain the numerical solution. In the

2D	1-level precond.		2-level precond.	
# of subdomains	# of iterations	Wall-clock time	# of iterations	Wall-clock time
16	42	20.95 s	11	6.69 s
64	55	4.88 s	14	1.58 s
140	68	2.08 s	16	0.69 s

3D	1-level precond.		2-level precond.	
# of subdomains	# of iterations	Wall-clock time	# of iterations	Wall-clock time
16	31	209.93 s	17	129.15 s
64	39	29.24 s	15	13.17 s
140	44	12.49 s	16	5.54 s

Table 3.5 Comparison between a one-level and a two-level preconditioner for the 2D and 3D test cases

water model, the outer loop consists in a fixed point algorithm solving alternatively the root problem (3.2.17) and the soil problem (3.4.2). Solving the linear system resulting from the discrete soil problem (3.4.2) using the domain decomposition method presented in this section constitutes an inner loop. Local problems defined on each subdomain are also solved iteratively using a conjugate gradient method, and thus the complete algorithm consists in three nested loops.

We can take advantage of the iterative nature of the domain decomposition and linear solvers by using adaptive stopping criteria in order to further reduce the computational time. Here we use simple heuristics expressing that there is no need to continue with iterations in the inner loop once the error from the outer loop starts to dominate. More elaborate stopping criteria can be used, see for example [81] where adaptive stopping criteria based on a posteriori error estimates are derived.

3.7 Numerical resolution

The purpose of the numerical examples presented in this section is to illustrate the capabilities of the numerical model.

Numerical values used in the examples are as follows:

— parameters for a clay soil are $\theta_m = 0.068$, $\theta_M = 0.38$, $\lambda = 0.17$, $h_b = -0.4$ m, $K_s = 0.144\ \mathrm{m\,d^{-1}}$.

— the initial water potential in the soil domain is in hydrostatic equilibrium: $h_0 = -15\text{ m} - z$.

For simplicity, all root parameters are taken constant across the whole root system. Numerical values of L_r and K_x for maize are taken from [13]:

— Root radius is set to 5.0×10^{-4} m.

— $L_r = 1.92308 \times 10^{-4}\ \mathrm{d}^{-1}$, $K_x = 4.32 \times 10^{-8}\ \mathrm{m}^3\,\mathrm{d}^{-1}$.

As an illustration of the nutrient model, we consider the transport and uptake of nitrate. Parameters for equation (3.3.2) are taken from [4], Michaelis-Menten constants for maize are taken from [3]:

— $A_0 = 1.6416 \times 10^{-4}\ \mathrm{m}^2\,\mathrm{d}^{-1}$, $f_1 = 1.58$, $f_2 = -0.17$, $\theta_l = 0.12$.

— $F_m = 8.64 \times 10^{-3}\ \mathrm{mol\,m}^{-2}\,\mathrm{d}^{-1}$, $K_m = 2.5 \times 10^{-2}\ \mathrm{mol\,m}^{-3}$.

— the homogeneous initial concentration of nitrate in the soil solution is $c_0 = 5$ $\mathrm{mol\,m}^{-3}$.

We consider that adsorption of nitrate in the soil solid phase is negligible: $\varphi = 0$.

The first numerical simulation involves the 20-days-old maize root system generated by the Matlab code RootBox depicted in Fig. 3.1. The soil domain is of dimensions 0.4 m × 0.4 m × 0.4 m. No-flux boundary conditions are imposed on the boundaries of the soil domain. A constant transpiration rate equal to $1.44 \times 10^{-4}\ \mathrm{m}^3\,\mathrm{d}^{-1}$ is imposed at the root collar. The time step Δt is taken constant equal to 0.05 d. Numerical results are depicted in Figs. 3.6 and 3.7. Fig. 3.6 shows the Darcy flux q in the vicinity of the roots. In the beginning of the simulation, root water uptake is still relatively evenly distributed over the dense upper portion of the root system (left picture, $t = 4.8$h). As time passes, the uptake pattern is modified. The soil dries in the dense root zone and the root system takes up water from wetter zones (mostly in the deeper part of the soil profile) in order to maintain a constant transpiration rate (right picture, $t = 7.3$d).

Fig. 3.7 shows high gradients developing in the vicinity of the roots as the soil dries.

Figure 3.6 Soil water flow near the root system of a 20-days-old maize plant

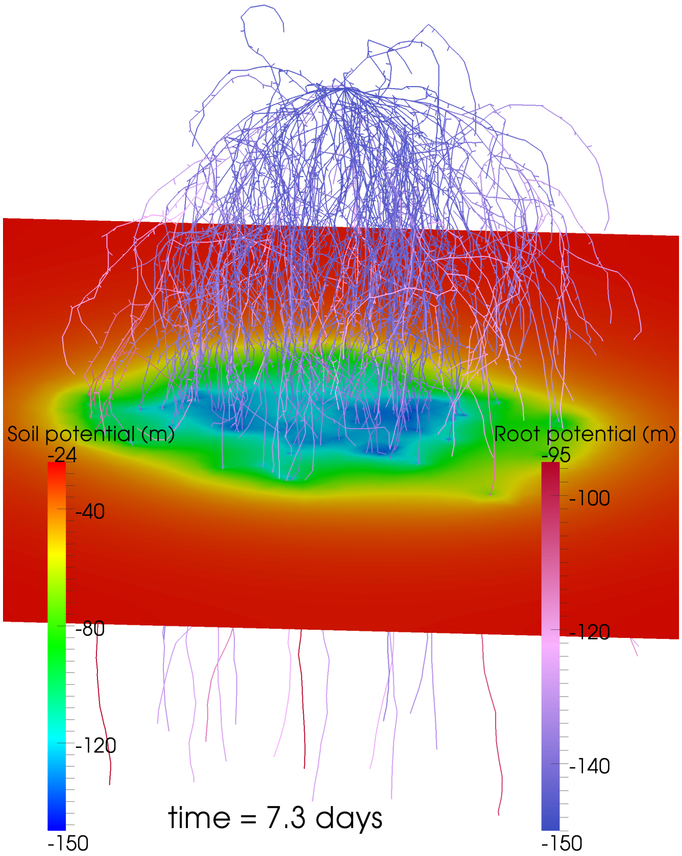

Figure 3.7 Root water potential h_r defined on the tree-like network and slice of the soil water potential h_s

The second example illustrates how we are able to integrate root growth and chemotropism in 2D by coupling the model with the implementation of growth and tropisms in RootBox.

RootBox can simulate root tip response to mechanical soil heterogeneities as well as various types of tropisms like gravitropism, hydrotropism or chemotropism. The specific growth behaviour can be chosen for every root type.

In RootBox, the implementation of tropisms consists in computing the new growth direction by random minimization of an objective function: for each active root tip, several rotations are randomly computed and the one that leads to minimizing the objective function is chosen. Different types of tropisms are realized by choosing appropriate objective functions depending on soil properties (water content, nutrient concentration). In this example, a combination of gravitropism and chemotropism is achieved by defining the objective function as $-\lambda c + z$ where $\lambda > 0$ represents the relative strength of chemotropism. At each time step, an iteration of the following coupling algorithm is performed:

1. RootBox finds the best growth direction for each active root tip through multiple evaluations of the objective function depending on the spatial concentration c. RootBox is interfaced with the FreeFem++ finite element code so that the values

of the concentration can be determined by interpolation on the mesh. Then, a new tree-like network with new root segments is obtained.

2. A mesh adapted to the new characteristic function f_c is obtained from the previous mesh by the mesh adaptation procedure described in section 3.5.
3. Finite element functions (namely the current soil water potential and N concentration) are interpolated from the previous mesh to the new mesh.
4. Solve (3.2.12) and (3.3.11) and obtain the new soil water potential and N concentration distributions.

Fig. 3.8 depicts some results of such a simulation with the initial nitrate concentration set to a linear profile varying from 0 mol m^{-3} at the top left corner of the domain to 10 mol m^{-3} at the bottom right corner. Notice the accumulation of nitrate around some of the roots in the bottom right: as the soil dries out, radial soil-root water flow increases in the bottom right where the soil is wetter, resulting in the mass flow of nitrate bringing more than the root can take up.

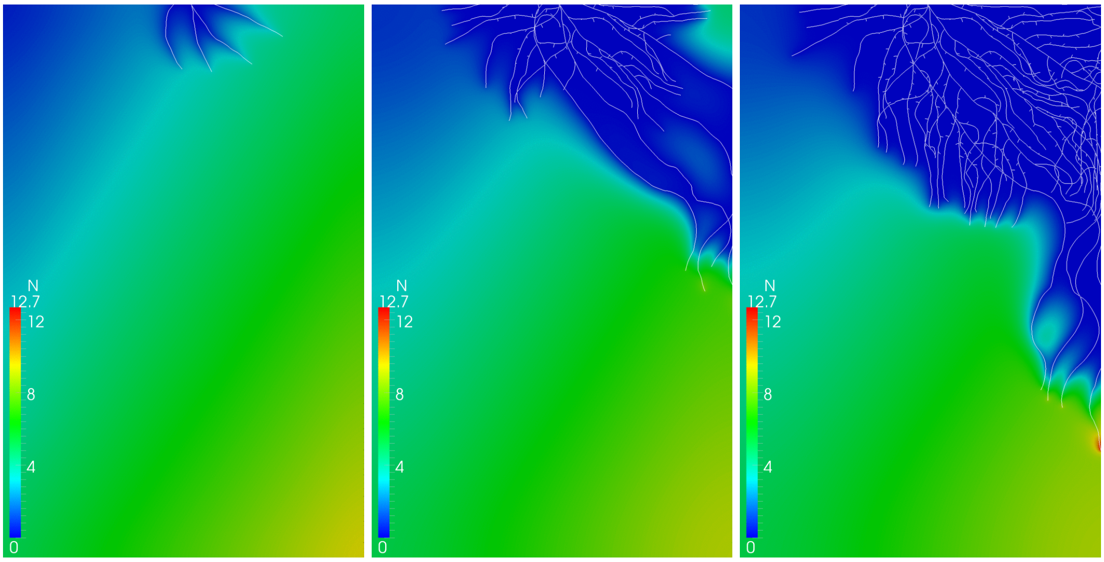

Figure 3.8 2D simulation example with root growth and chemotropism: snapshots of nitrate concentration at different time steps. In white, isosurface 0.5 of the characteristic function f_c.

3.8 Conclusion

In this chapter we presented a model of soil water and nutrient transport with plant root uptake. A characteristic function of the geometry of the root system was used to construct accurate sink terms corresponding to water and nutrient uptake by roots. An emphasis was put on the spatial discretization with an adaptive mesh refinement procedure producing meshes that are able to resolve the complex geometry of the root system together with small-scale phenomena occuring in the rhizosphere. A parallel finite element method was then presented using a two-level Schwarz domain decomposition method to solve the potentially large systems arising from the discretization. Numerical experiments were conducted in two and three spatial dimensions to illustrate the capabilities of the model.

Chapter 4

Modeling root uptake and root growth using the diffuse domain approach

The content of this chapter is included in [75].

Contents

4.1 Introduction

Plant scale models involving the explicit architectural description of root system development are designed to address the spatial and temporal heterogeneity of soil water and nutrient distribution and uptake in relation to root system architecture.
Furthermore, local processes occurring at the soil-root interface and in the rhizosphere play a major role in belowground interactions, and taking into account these small-scale processes is of fundamental importance for understanding plant-soil relationships.
This study follows on from the work presented in chapter 3 in an attempt to bridge the gap between single root scale and plant scale models. We use mathematical and numerical tools to develop a mechanistic model for predicting water and solute movement with root uptake and root growth at the root system scale while accurately resolving processes at the soil-root interface by explicitly considering the surface of the root.
The main idea is the following: instead of considering an explicit discretization of the root surface as a surface mesh, which remains a difficult challenge when considering root growth and complex root systems, a level set representation of the root surface is introduced through a signed distance function and the problem is reformulated in a larger regular computational domain by using the diffuse domain approach, where the sharp boundary is approximated by a diffuse layer.
The computational expense of the model can be reduced to a tractable cost by taking advantage of parallel computing together with unstructured adaptive meshing techniques.
The chapter is organized as follows: section 4.2 describes the mathematical setting of soil water and solute transport together with root water and nutrient uptake. Section 4.3 introduces the diffuse domain approach used to define the approximate regularized problems. In section 4.4, numerical discretization schemes for the approximate problems are presented. Section 4.5 deals with the representation and discretization of root systems as well as the computation of the signed distance function to the root surface. Section 4.6 describes the mesh adaptation procedure, and section 4.7 discusses details of the parallel implementation. Finally, some numerical results are presented in section 4.8.

4.2 Mathematical model

Let us consider a plant root system $\Omega_r(t)$ surrounded by the soil domain $\Omega_s(t)$, with $t \in I = [0,T], T > 0$. The root surface is represented by the interface between the two domains $\Gamma_r(t)$ and the root collar is denoted by Γ_p. Γ_e is the exterior boundary of the soil domain. Let $\vec{n}(t)$ be the unit outward normal to the boundary of the domain $\Omega_s(t)$.
The evolution of the domain $\Omega_r(t)$ over time corresponds to the development of the root system. Let V be the normal velocity of $\Gamma_r(t)$.
Here we only consider root growth and we do not take into account root shrinking nor root death:

$$V \leq 0 \quad \text{on} \quad I \times \Gamma_r(t). \tag{4.2.1}$$

Throughout this chapter and for clarity, the dependence in time will be omitted in the notations unless necessary.
The modeling framework considered in this study is analogous to that of chapter 3 and is recalled in the following for completeness.

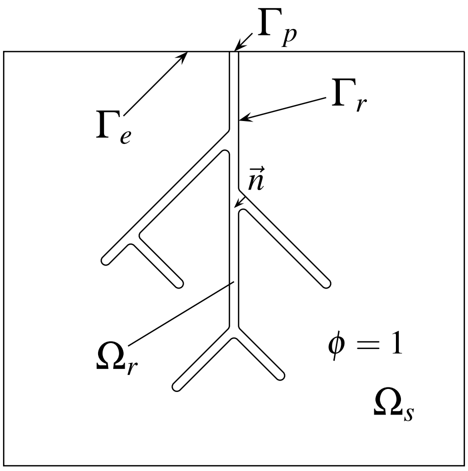

Figure 4.1 Configuration of the domain

4.2.1 Soil water movement with root water uptake

The Richards equation

Soil water movement is governed by the Richards equation. Richards equation is derived from the continuity equation

$$\frac{\partial \theta}{\partial t} + \nabla . q = 0, \tag{4.2.2}$$

with θ the volumetric water content and q the macroscopic Darcy flow.
Darcy law relates the water flow to the pressure of the water:

$$q = -K \nabla H, \tag{4.2.3}$$

where K is the hydraulic conductivity and H is the total hydraulic head and can be expressed as

$$H = h + z. \tag{4.2.4}$$

The pressure head h comes from a hydrostatic pressure if $h > 0$ and from a capillary pressure if $h < 0$. z is the height against the gravitational direction.

By combining (4.2.2) and (4.2.3) we obtain the Richards equation:

$$\partial_t(\theta(h)) - \nabla.(K(\theta(h))\nabla(h+z)) = 0 \quad \text{in} \quad I \times \Omega_s. \tag{4.2.5}$$

Equation (4.2.5) is subject to the initial condition

$$h(0,x) = h_0(x) \quad \text{in} \quad \Omega_s, \tag{4.2.6}$$

and the no-flux boundary condition at the exterior boundary

$$-K(\theta(h))\nabla(h+z).\vec{n} = 0 \quad \text{on} \quad I \times \Gamma_e. \tag{4.2.7}$$

The $\theta(h)$ and $K(\theta(h))$ relationships are given by the Brooks-Corey model which we recall here:

$$\begin{aligned} \Theta(h) &:= \frac{\theta(h)-\theta_m}{\theta_M-\theta_m} = \left[\frac{h}{h_b}\right]^{-\lambda} := \begin{cases} \left(\frac{h}{h_b}\right)^{-\lambda} & \text{for} \quad h \le h_b \\ 1 & \text{for} \quad h \ge h_b, \end{cases} \\ K(\theta(h)) &= K_s\Theta(h)^{e(\lambda)} = K_s\left[\frac{h}{h_b}\right]^{-\lambda e(\lambda)} \quad \text{with } e(\lambda) := 3+\frac{2}{\lambda}, \end{aligned} \tag{4.2.8}$$

where Θ is the normalized water content.

The parameters of the model are defined as follows:

- θ_M is the saturated water content.
- θ_m is the residual water content.
- K_s is the saturated hydraulic conductivity.
- h_b is the bubbling pressure head.
- λ is the pore size distribution index.

Root water uptake

Water flow in roots and between soil and roots is assumed to follow an Ohm's law analogy and the model makes the same assumptions as in chapter 3 which are detailed in section 3.2.2.

Water transport through the root system Ω_r is driven by potential gradient. The water potential in the root system is denoted by u. The conductivity of the root is denoted by K_r.

The internal structure of a root is quite complex and consists in layers of different tissues from the epidermis to the xylem. As a first step and for the sake of simplicity, we consider that the root system Ω_r represents the xylem vessels. The conductivity L_r of the root surface Γ_r thus takes into account all root tissues between the root surface and the xylem.

The uptake flux through the soil-root interface is proportional to the conductivity L_r and to the difference of water potential between the soil and the root $h-u$.

Furthermore, the evolution of the domain $\Omega_s(t)$ due to root growth induces a boundary flux $-\theta(h)V$ on Γ_r which can be related to the mechanism of root interception, i.e. contact with soil particles and the surrounding soil solution as a result of root growth. The boundary condition on Γ_r then reads:

$$-K(\theta(h))\nabla(h+z).\vec{n} - \theta(h)V = -K_r\nabla(u+z).\vec{n} = L_r(h-u) \quad \text{on} \quad I \times \Gamma_r. \tag{4.2.9}$$

Finally, following the transpiration-cohesion-tension mecanism, the whole system is driven by the boundary condition at the root collar Γ_p. We can specify the transpirational flux or prescribe the water potential at the root collar. In the following we will consider the latter case, which translates into a Dirichlet boundary condition; let u_c be the prescribed water potential at the root collar.
We are then able to write the following coupled problem: find (h,u) such that

$$\begin{cases} \partial_t(\theta(h)) - \nabla.(K(\theta(h))\nabla(h+z)) = 0 & \text{in } I\times\Omega_s, \\ -K(\theta(h))\nabla(h+z).\vec{n} = 0 & \text{on } I\times\Gamma_e, \\ -K(\theta(h))\nabla(h+z).\vec{n} = L_r(h-u)+\theta(h)V & \text{on } I\times\Gamma_r, \\ h(0,x) = h_0 & \text{in } \Omega_s, \\ & \\ -\nabla.(K_r\nabla(u+z)) = 0 & \text{in } I\times\Omega_r, \\ -K_r\nabla(u+z).\vec{n} = L_r(h-u) & \text{on } I\times\Gamma_r. \\ u = u_c & \text{on } I\times\Gamma_p. \end{cases} \tag{4.2.10}$$

4.2.2 Nutrient transport with root nutrient uptake

We consider the evolution of the concentration c of a nutrient ion N in the soil solution, governed by diffusion, mass flow, adsorption and root uptake.

The convection-diffusion equation

The convection-diffusion equation in its conservative form can be written as:

$$\partial_t(\theta c + \varphi(c)) - \nabla.(A\nabla c - qc) = 0 \quad \text{in} \quad I\times\Omega_s, \tag{4.2.11}$$

where

— A is the diffusion coefficient of N in the soil and is given by

$$A = A_0\theta f_l, \tag{4.2.12}$$

with A_0 the diffusion coefficient of N in free water and f_l the so-called tortuosity factor:

$$f_l = \begin{cases} f_1\theta + f_2 & \text{for} \quad \theta \geq \theta_l, \\ \frac{\theta(f_1\theta_l+f_2)}{\theta_l} & \text{for} \quad \theta < \theta_l, \end{cases} \tag{4.2.13}$$

where f_1, f_2 and θ_l are parameters depending on soil properties.

— φ is a sorption isotherm relating the amount of adsorbed N to the equilibrium concentration of N in solution. For example, the Freundlich adsorption isotherm is expressed as

$$\varphi(c) = \kappa c^b, \tag{4.2.14}$$

where $\kappa > 0$ and $b \in (0,1)$ are fitting parameters.

Equation (4.2.11) is subject to the initial condition

$$c(0,x) = c_0(x) \quad \text{in} \quad \Omega_s, \tag{4.2.15}$$

and the no-flux boundary condition at the exterior boundary

$$-(A\nabla c - qc).\vec{n} = 0 \quad \text{on} \quad I \times \Gamma_e. \tag{4.2.16}$$

Multiplying equation (4.2.5) by c and substracting it from equation (4.2.11) yields the convective form of equation (4.2.11):

$$(\theta + \varphi'(c))\partial_t c = \nabla.(A\nabla c) - q.\nabla c \quad \text{in} \quad I \times \Omega_s. \tag{4.2.17}$$

Root nutrient uptake

The model takes into account active nutrient uptake at the root surface. As in the previous chapters, nutrient transport within the root system is not considered.
Nutrient uptake by roots is given by the Michaelis-Menten model, relating the root uptake rate of N to its concentration at the root surface:

$$h(c) = \frac{F_m c}{K_m + c}, \tag{4.2.18}$$

where $h(c)$ is the uptake rate and $F_m, K_m > 0$ are parameters of the model.
Furthermore, the evolution of the domain $\Omega_s(t)$ due to root growth induces a boundary flux $-(\theta c + \varphi(c))V$ on Γ_r similar to the boundary flux for water $-\theta V$. The resulting boundary condition on Γ_r is

$$\begin{aligned} & -(A\nabla c - qc).\vec{n} - (\theta c + \varphi(c))V = h(c) \\ \Longleftrightarrow & -A\nabla c.\vec{n} - \varphi(c)V = h(c) - Lr(h-u)c \quad \text{on} \quad I \times \Gamma_r, \end{aligned} \tag{4.2.19}$$

where we used the water flux boundary condition on Γ_r (4.2.9).
We can finally state the problem: find c such that

$$\begin{cases} (\theta + \varphi'(c))\partial_t c - \nabla.(A\nabla c) + q.\nabla c = 0 & \text{in} \quad I \times \Omega_s, \\ -A\nabla c.\vec{n} = 0 & \text{on} \quad I \times \Gamma_e, \\ -A\nabla c.\vec{n} = h(c) - L_r(h-u)c + \varphi(c)V & \text{on} \quad I \times \Gamma_r, \\ c(0,x) = c_0(x) & \text{in} \quad \Omega_s. \end{cases} \tag{4.2.20}$$

4.3 The diffuse domain approach

The diffuse domain approach [49] allows us to avoid the difficult task of generating a conformal mesh to the complex geometry of the root system represented by the boundary Γ_r. The problem is reformulated in the larger regular domain $\Omega = \Omega_s \cup \Omega_r$ and Γ_r is implicitly represented by a diffuse interface defined through a phase field function ϕ approximating the characteristic function of the domain Ω_s.

4.3.1 Formulation of the approximate problems

In the following we derive the diffuse domain formulation for problem (4.2.10). Multiplying the first equation by a test function v and integrating over $I \times \Omega_s$ leads to

$$\int_0^T \int_{\Omega_s} \partial_t(\theta(h))v - \int_0^T \int_{\Omega_s} \nabla.(K(\theta(h))\nabla(h+z))v = 0.$$

Integrating by parts yields

$$\int_0^T \int_{\Omega_s} \partial_t(\theta(h))v + \int_0^T \int_{\Omega_s} K(\theta(h))\nabla(h+z)\nabla v + \int_0^T \int_{\Gamma_r} L_r(h-u)v + \int_0^T \int_{\Gamma_r} \theta(h)Vv = 0.$$

Introducing the characteristic function χ_{Ω_s} of the domain Ω_s and the surface delta function δ_{Γ_r}, and changing the integration domain to Ω, we obtain

$$\int_0^T \int_{\Omega} \chi_{\Omega_s}\partial_t(\theta(h))v + \int_0^T \int_{\Omega} \chi_{\Omega_s}K(\theta(h))\nabla(h+z)\nabla v + \int_0^T \int_{\Omega} \delta_{\Gamma_r}L_r(h-u)v + \int_0^T \int_{\Gamma_r} \theta(h)Vv = 0. \quad (4.3.1)$$

Applying Reynolds' transport theorem, the last term in (4.3.1) reads

$$\int_{\Gamma_r(t)} \theta(h)Vv = \frac{\mathrm{d}}{\mathrm{d}t}\int_{\Omega_s(t)} \theta(h)v - \int_{\Omega_s(t)} \partial_t(\theta(h)v) = \frac{\mathrm{d}}{\mathrm{d}t}\int_{\Omega} \chi_{\Omega_s}\theta(h)v - \int_{\Omega} \chi_{\Omega_s}\partial_t(\theta(h)v). \quad (4.3.2)$$

Following similar steps for the second set of equations of problem (4.2.10) yields

$$\int_0^T \int_{\Omega} \chi_{\Omega_r}K_r\nabla(u+z)\nabla v - \int_0^T \int_{\Omega} \delta_{\Gamma_r}L_r(h-u)v = 0, \quad (4.3.3)$$

where χ_{Ω_r} is the characteristic function of the domain Ω_r.
In order to approximate the characteristic functions χ_{Ω_r} and χ_{Ω_s}, we define the following phase field function for $\varepsilon > 0$:

$$\phi(t,x) = \frac{1}{2}\left(1 - \tanh\left(\frac{3r(t,x)}{\varepsilon}\right)\right), \quad (4.3.4)$$

where $r(t,x)$ is the signed distance of x from $\Gamma_r(t)$, negative in $\Omega_s(t)$ and positive in $\Omega_r(t)$.
We can see that

$$\begin{cases} \lim_{\varepsilon \to 0} \phi = \chi_{\Omega_s}, \\ \lim_{\varepsilon \to 0} \psi := (1-\phi) = \chi_{\Omega_r}. \end{cases} \quad (4.3.5)$$

The original sharp boundary Γ_r is thus replaced by a diffuse boundary, where ε sets the width of the diffuse interface layer that separates the two diffuse domains.
In the following, we also use $\varepsilon^{-1}B(\phi) = \varepsilon^{-1}36\phi^2(1-\phi)^2$ as an approximation of the

surface delta function δ_{Γ_r}.

Using (4.3.2), we can now define the approximate variational problem corresponding to (4.3.1):

$$\int_0^T \int_\Omega \phi \partial_t(\theta(h))v + \int_0^T \int_\Omega \phi K(\theta(h))\nabla(h+z)\nabla v + \int_0^T \int_\Omega \varepsilon^{-1} B(\phi) L_r(h-u)v + \int_0^T \int_\Omega \partial_t \phi \theta(h) v = 0. \tag{4.3.6}$$

Integrating by parts gives

$$\int_0^T \int_\Omega \partial_t(\phi\theta(h))v - \int_0^T \int_\Omega \nabla.(\phi K(\theta(h))\nabla(h+z))v + \int_0^T \int_\Gamma \phi v K(\theta(h))\nabla(h+z).\vec{n_0} + \int_0^T \int_\Omega \varepsilon^{-1} B(\phi) L_r(h-u)v = 0,$$

where $\vec{n_0}$ is the unit outward normal to the boundary Γ of the domain Ω.
Thus, we have

$$\begin{cases} \partial_t(\phi\theta(h)) - \nabla.(\phi K(\theta(h))\nabla(h+z)) + \varepsilon^{-1} B(\phi) L_r(h-u) = 0 & \text{in } I \times \Omega, \\ -\phi K(\theta(h))\nabla(h+z).\vec{n_0} = 0 & \text{on } I \times \Gamma. \end{cases} \tag{4.3.7}$$

Similarly, the approximate variational problem corresponding to (4.3.3) is

$$\int_0^T \int_\Omega \psi K_r \nabla(u+z)\nabla v - \int_0^T \int_\Omega \varepsilon^{-1} B(\phi) L_r(h-u)v = 0 \tag{4.3.8}$$

and we have

$$\begin{cases} -\nabla.(\psi K_r \nabla(u+z)) - \varepsilon^{-1} B(\phi) L_r(h-u) = 0 & \text{in } I \times \Omega, \\ -\psi K_r \nabla(u+z).\vec{n_0} = 0 & \text{on } I \times \Gamma_e, \\ u = u_c & \text{on } I \times \Gamma_p. \end{cases} \tag{4.3.9}$$

Thus, we can approach the initial problem (4.2.10) by the following approximate problem corresponding to (4.3.7) and (4.3.9): find (h,u) such that

$$\begin{cases} \partial_t(\phi\theta(h)) - \nabla.(\phi K(\theta(h))\nabla(h+z)) + \varepsilon^{-1} B(\phi) L_r(h-u) = 0 & \text{in } I \times \Omega, \\ -\phi K(\theta(h))\nabla(h+z).\vec{n_0} = 0 & \text{on } I \times \Gamma, \\ h(0,x) = \overline{h_0}(x) & \text{in } \Omega, \\ & \\ -\nabla.(\psi K_r \nabla(u+z)) - \varepsilon^{-1} B(\phi) L_r(h-u) = 0 & \text{in } I \times \Omega, \\ -\psi K_r \nabla(u+z).\vec{n_0} = 0 & \text{on } I \times \Gamma_e, \\ u = u_c & \text{on } I \times \Gamma_p, \end{cases} \tag{4.3.10}$$

where $\overline{h_0}$ is an extension of h_0 to the domain Ω.

In a similar manner, we can derive the diffuse domain formulation for problem (4.2.20). Multiplying the first equation of (4.2.20) by a test function v and integrating over $I \times \Omega_s$ leads to

$$\int_0^T \int_{\Omega_s} (\theta + \varphi'(c))\partial_t c v - \int_0^T \int_{\Omega_s} \nabla.(A\nabla c)v + \int_0^T \int_{\Omega_s} q.\nabla c v = 0.$$

Integrating by parts yields

$$\begin{aligned}\int_0^T \int_{\Omega_s} (\theta + \varphi'(c))\partial_t c v + \int_0^T \int_{\Omega_s} A\nabla c \nabla v + \int_0^T \int_{\Omega_s} q.\nabla c v \\ + \int_0^T \int_{\Gamma_r} (h(c) - L_r(h-u)c)v + \int_0^T \int_{\Gamma_r} \varphi(c) V v = 0.\end{aligned}$$

Changing the integration domain to Ω, we obtain

$$\begin{aligned}\int_0^T \int_{\Omega} \chi_{\Omega_s}(\theta + \varphi'(c))\partial_t c v + \chi_{\Omega_s} A\nabla c \nabla v + \chi_{\Omega_s} q.\nabla c v \\ + \int_0^T \int_{\Omega} \delta_{\Gamma_r}(h(c) - L_r(h-u)c)v + \int_0^T \int_{\Gamma_r} \varphi(c) V v = 0.\end{aligned}$$

Applying Reynolds' transport theorem yields

$$\int_{\Gamma_r(t)} \varphi(c) V v = \frac{\mathrm{d}}{\mathrm{d}t} \int_{\Omega_s(t)} \varphi(c) v - \int_{\Omega_s(t)} \partial_t(\varphi(c)v) = \frac{\mathrm{d}}{\mathrm{d}t} \int_{\Omega} \chi_{\Omega_s} \varphi(c) v - \int_{\Omega} \chi_{\Omega_s} \partial_t(\varphi(c)v).$$

Proceeding as above, we can then approach the initial problem (4.2.20) by the following approximate problem: find c such that

$$\begin{cases} \phi(\theta + \varphi'(c))\partial_t c - \nabla.(\phi A\nabla c) + \phi q.\nabla c \\ \qquad + \varepsilon^{-1} B(\phi)\,(h(c) - L_r(h-u)c) + \varphi(c)\partial_t \phi = 0 & \text{in } I \times \Omega, \\ -\phi A\nabla c.\vec{n}_0 = 0 & \text{on } I \times \Gamma, \\ c(0,x) = \overline{c_0}(x) & \text{in } \Omega, \end{cases} \tag{4.3.11}$$

where $\overline{c_0}$ is an extension of c_0 to the domain Ω.

4.3.2 Convergence study

In this section we give a formal justification of the diffuse domain approximate problems (4.3.10) and (4.3.11).

Let us first turn our attention to problem (4.3.10). We assume that K_r and L_r are constants for simplicity. When considering the general case one only needs to extend L_r such that the extension is constant in the normal direction to Γ_r.

In the following we denote the direction of gravity by $\vec{g} := -\nabla z$.
We use the method of matched asymptotic expansions to show that when $\varepsilon \to 0$ we recover the original problem (4.2.10). In this approach, the domain is separated into two regions - the regions far from Γ_r (the outer region) and the region near Γ_r (the inner region). In each region, the variables are expanded in powers of the diffuse interface thickness ε. In a region where both expansions are valid, the expansions are matched.

We introduce a local coordinate system. Define $r = r(x,\varepsilon)$ to be the signed distance of x from Γ_r. Furthermore let $X : S \to \mathbb{R}^d$ be a parametric representation of Γ_r, where S is an oriented manifold of dimension $d-1$. Let $n = n(s,\varepsilon)$ denote the unit normal vector to Γ_r pointing into Ω_r, and let s be the arclength. Then we assume that for $0 < \rho << 1$ there exists a neighborhood

$$U_\varepsilon = \left\{ x \in \Omega \,\middle|\, |r(x,\varepsilon)| < \rho \right\}$$

of Γ_r such that one can write $x = X(s,\varepsilon) + r(x,\varepsilon)n(x,\varepsilon)$ for $x \in U_\varepsilon$.
Now we can express variables in the new coordinate system, for example

$$h(r,s,\varepsilon) := h(x,\varepsilon) = h(X(s,\varepsilon) + rn(s,\varepsilon),\varepsilon), \quad x \in U_\varepsilon. \tag{4.3.12}$$

Here we expand h, K, θ, u, ϕ and ψ in non-negative powers of ε:

$$h(r,s,\varepsilon) = h_0(r,s) + \varepsilon h_1(r,s) + ..., \quad K(r,s,\varepsilon) = K_0(r,s) + \varepsilon K_1(r,s) + ... \tag{4.3.13}$$

To find the inner expansion, we introduce a stretched variable $\zeta := \frac{r}{\varepsilon}$, and define

$$\begin{aligned} &H(\zeta,s,\varepsilon) = h(r,s,\varepsilon), \quad \boldsymbol{K}(\zeta,s,\varepsilon) = K(r,s,\varepsilon), \quad \Theta(\zeta,s,\varepsilon) = \theta(r,s,\varepsilon), \\ &U(\zeta,s,\varepsilon) = u(r,s,\varepsilon), \quad \Phi(\zeta,s,\varepsilon) = \phi(r,s,\varepsilon), \quad \Psi(\zeta,s,\varepsilon) = \psi(r,s,\varepsilon). \end{aligned} \tag{4.3.14}$$

As in the outer expansion, we expand $H, \boldsymbol{K}, \Theta, U, \Phi$ and Ψ in non-negative powers of ε:

$$H(\zeta,s,\varepsilon) = H_0(\zeta,s) + \varepsilon H_1(\zeta,s) + ..., \quad \boldsymbol{K}(\zeta,s,\varepsilon) = \boldsymbol{K}_0(\zeta,s) + \varepsilon \boldsymbol{K}_1(\zeta,s) + ... \tag{4.3.15}$$

By matching the inner and outer expansions in an overlapping region where both expansions are valid, the following matching conditions hold:

$$\begin{cases} \lim\limits_{r\to\pm 0} h_0(r,s) = \lim\limits_{\zeta\to\pm\infty} H_0(\zeta,s), \\ \lim\limits_{r\to\pm 0} u_0(r,s) = \lim\limits_{\zeta\to\pm\infty} U_0(\zeta,s), \\ \lim\limits_{r\to\pm 0} \phi_0(r,s) = \lim\limits_{\zeta\to\pm\infty} \Phi_0(\zeta,s), \\ \lim\limits_{r\to\pm 0} K_0 \nabla h_0.\vec{n} = \lim\limits_{\zeta\to\pm\infty} \left(\boldsymbol{K}_1 \partial_\zeta H_0 + \boldsymbol{K}_0 \partial_\zeta H_1 \right), \\ \lim\limits_{r\to\pm 0} K_r \nabla u_0.\vec{n} = \lim\limits_{\zeta\to\pm\infty} K_r \partial_\zeta U_1. \end{cases} \tag{4.3.16}$$

Outer expansion:
At leading order $O(\varepsilon^0)$, equations (4.3.10) yield

$$\begin{cases} \partial_t \theta_0 - \nabla.(K_0(\nabla h_0 - \vec{g})) = 0 \quad \text{in} \quad I \times \Omega_s, \\ -\nabla.(K_r(\nabla u_0 - \vec{g})) = 0 \quad \text{in} \quad I \times \Omega_r, \end{cases} \tag{4.3.17}$$

and we recover the original equations of (4.2.10) in Ω_s and Ω_r.

Inner expansion:
At $O(\varepsilon^{-2})$, we obtain

$$\begin{cases} -\partial_\zeta(\Phi_0 \boldsymbol{K}_0 \partial_\zeta H_0) = 0, \\ -\partial_\zeta(\Psi_0 K_r \partial_\zeta U_0) = 0, \end{cases} \tag{4.3.18}$$

which gives

$$\begin{cases} \partial_\zeta H_0 = 0, \\ \partial_\zeta U_0 = 0. \end{cases} \tag{4.3.19}$$

At $O(\varepsilon^{-1})$, using the fact that in the inner expansion $\partial_t = -\frac{V}{\varepsilon}\partial_\zeta + O(\varepsilon^0)$ we have

$$\begin{cases} -V\partial_\zeta \Phi_0 \Theta_0 - \partial_\zeta((\Phi_0 \boldsymbol{K}_1 + \Phi_1 \boldsymbol{K}_0)\partial_\zeta H_0) \\ \qquad\qquad - \partial_\zeta(\Phi_0 \boldsymbol{K}_0(\partial_\zeta H_1 - \vec{g}.\vec{n})) + L_r(H_0 - U_0)B(\Phi_0) = 0, \\ -\partial_\zeta(\Psi_1 K_r \partial_\zeta U_0) - \partial_\zeta(\Psi_0 K_r(\partial_\zeta U_1 - \vec{g}.\vec{n})) - L_r(H_0 - U_0)B(\Phi_0) = 0. \end{cases} \tag{4.3.20}$$

Since $\Theta_0 = \theta(H_0)$ and using (4.3.19), equations (4.3.20) read

$$\begin{cases} -\Theta_0 V \partial_\zeta \Phi_0 - \partial_\zeta(\Phi_0 \boldsymbol{K}_0(\partial_\zeta H_1 - \vec{g}.\vec{n})) + L_r(H_0 - U_0)B(\Phi_0) = 0, \\ -\partial_\zeta(\Psi_0 K_r(\partial_\zeta U_1 - \vec{g}.\vec{n})) - L_r(H_0 - U_0)B(\Phi_0) = 0. \end{cases} \tag{4.3.21}$$

Integrating the above equations from $-\infty$ to $+\infty$ and using that H_0, U_0, Θ_0 and V are independent of ζ together with the fact that

$$\int_{-\infty}^{\infty} B(\Phi_0)d\zeta = \int_1^0 \frac{B(\Phi_0)}{\partial_\zeta \Phi_0} d\Phi_0 = \frac{1}{6}\int_0^1 \frac{B(\Phi_0)}{\Phi_0(1-\Phi_0)} d\Phi_0 = 6\int_0^1 \Phi_0(1-\Phi_0)d\Phi_0 = 1 \tag{4.3.22}$$

we obtain

$$\begin{cases} \lim\limits_{\zeta \to -\infty} \left[\Theta_0 V + \boldsymbol{K}_0(\partial_\zeta H_1 - \vec{g}.\vec{n}) + L_r(H_0 - U_0)\right] = 0, \\ \lim\limits_{\zeta \to +\infty} \left[-K_r(\partial_\zeta U_1 - \vec{g}.\vec{n}) - L_r(H_0 - U_0)\right] = 0. \end{cases} \tag{4.3.23}$$

By using the matching conditions (4.3.16), we get

$$\begin{cases} \lim\limits_{r \to -0} -K_0(\nabla h_0 - \vec{g}).\vec{n} = \lim\limits_{r \to -0} (L_r(h_0 - u_0) + \theta_0 V), \\ \lim\limits_{r \to +0} -K_r(\nabla u_0 - \vec{g}).\vec{n} = \lim\limits_{r \to +0} L_r(h_0 - u_0), \end{cases} \tag{4.3.24}$$

and we recover the original boundary conditions of problem (4.2.10) on Γ_r.

In a similar manner, we can give a formal justification for the diffuse domain approximate problem (4.3.11) and show that when $\varepsilon \to 0$ we recover the original problem (4.2.20). Expressing variables in the local coordinate system as in (4.3.12), we expand c, A, q, θ, h, u and ϕ in non-negative powers of ε:

$$c(r,s,\varepsilon) = c_0(r,s) + \varepsilon c_1(r,s) + ..., \quad A(r,s,\varepsilon) = A_0(r,s) + \varepsilon A_1(r,s) + ... \tag{4.3.25}$$

To find the inner expansion, we introduce once again the stretched variable $\zeta = \frac{r}{\varepsilon}$, and define C, $\boldsymbol{A}$, Q, Θ, H, U and Φ as in (4.3.14)

$$C(\zeta,s,\varepsilon) = c(r,s,\varepsilon), \quad \boldsymbol{A}(\zeta,s,\varepsilon) = A(r,s,\varepsilon), \quad Q(\zeta,s,\varepsilon) = q(r,s,\varepsilon), \quad ... \tag{4.3.26}$$

As in the outer expansion, we expand C, $\boldsymbol{A}$, Q, Θ, H, U and Φ in non-negative powers of ε:

$$C(\zeta,s,\varepsilon) = C_0(\zeta,s) + \varepsilon C_1(\zeta,s) + ..., \quad \boldsymbol{A}(\zeta,s,\varepsilon) = \boldsymbol{A}_0(\zeta,s) + \varepsilon \boldsymbol{A}_1(\zeta,s) + ... \tag{4.3.27}$$

By matching the inner and outer expansions in an overlapping region where both expansions are valid, the following matching conditions hold:

$$\begin{cases} \lim\limits_{r\to\pm 0} h_0(r,s) = \lim\limits_{\zeta\to\pm\infty} H_0(\zeta,s), \\ \lim\limits_{r\to\pm 0} c_0(r,s) = \lim\limits_{\zeta\to\pm\infty} C_0(\zeta,s), \\ \lim\limits_{r\to\pm 0} \phi_0(r,s) = \lim\limits_{\zeta\to\pm\infty} \Phi_0(\zeta,s), \\ \lim\limits_{r\to\pm 0} A_0 \nabla c_0 . \vec{n} = \lim\limits_{\zeta\to\pm\infty} \left(\boldsymbol{A}_1 \partial_\zeta C_0 + \boldsymbol{A}_0 \partial_\zeta C_1 \right). \end{cases} \tag{4.3.28}$$

Outer expansion:
At leading order $O(\varepsilon^0)$, equation (4.3.11) reads

$$(\theta_0 + \varphi'(c_0))\partial_t(c_0) - \nabla.(A_0 \nabla c_0) + q_0.\nabla c_0 = 0 \qquad \text{in} \quad I \times \Omega_s, \tag{4.3.29}$$

and we recover the original equation (4.2.20) in Ω_s.

Inner expansion:
At $O(\varepsilon^{-2})$, we obtain

$$-\partial_\zeta(\Phi_0 \boldsymbol{A}_0 \partial_\zeta C_0) = 0, \tag{4.3.30}$$

which gives

$$\partial_\zeta C_0 = 0. \tag{4.3.31}$$

At $O(\varepsilon^{-1})$, we have after using (4.3.31)

$$-\partial_\zeta(\Phi_0 \boldsymbol{A}_0 \partial_\zeta C_1) + (h(C_0) - L_r(H_0 - U_0)C_0)B(\Phi_0) - \varphi(C_0) V \partial_\zeta \Phi_0 = 0. \tag{4.3.32}$$

Integrating the above equation from $-\infty$ to $+\infty$ and using that H_0, U_0, C_0 and V are independent of ζ together with (4.3.22) we obtain

$$\lim_{\zeta \to -\infty} \left[A_0 \partial_\zeta C_1 + h(C_0) - L_r(H_0 - U_0)C_0 + \varphi(C_0)V \right] = 0. \tag{4.3.33}$$

By using the matching conditions (4.3.28), we get

$$\lim_{r \to -0} -A_0 \nabla c_0 . \vec{n} = \lim_{r \to -0} (h(c_0) - L_r(h_0 - u_0)c_0 + \varphi(c_0)V), \tag{4.3.34}$$

and we recover the original boundary condition of problem (4.2.20) on Γ_r.

4.4 Numerical schemes

In this section we present the numerical approximation of problems (4.3.10) and (4.3.11). The numerical schemes are written using a constant time step and without considering transient mesh adaptation for simplicity.

4.4.1 Water model

Let $H_0^1(\Omega) := \{v \in H^1(\Omega),\ \gamma_0 v = 0\}$, where $\gamma_0 v$ is the trace of v to Γ_p.
We consider Problem (4.3.10) in the following weak sense:

$$\begin{cases} h \in L^2(0,T;H^1(\Omega)), \quad u - u_c \in L^2(0,T;H_0^1(\Omega)), \\ -\int_0^T \int_\Omega \phi(t,x)\theta(h(t,x))\partial_t \varphi_1(t,x) \mathrm{d}t\mathrm{d}x - \int_\Omega \phi(0,x)\theta(\overline{h_0}(x))\varphi_1(0,x)\mathrm{d}x \\ + \int_0^T \int_\Omega \phi(t,x)K(\theta(h(t,x)))\nabla(h(t,x)+z)\nabla\varphi_1(t,x)\mathrm{d}t\mathrm{d}x \\ + \int_0^T \int_\Omega \psi(t,x)K_r(t,x)\nabla(u(t,x)+z)\nabla\varphi_2(t,x)\mathrm{d}t\mathrm{d}x \\ + \int_0^T \int_\Omega \varepsilon^{-1}B(\phi(t,x))L_r(t,x)\left(h(t,x)-u(t,x)\right)\left(\varphi_1(t,x)-\varphi_2(t,x)\right)\mathrm{d}t\mathrm{d}x = 0, \\ \forall \varphi_1, \varphi_2 \in C_c^\infty([0,T)\times\Omega). \end{cases} \tag{4.4.1}$$

We consider a time discretization $(t^{(n)})_{n=0,\ldots,N}$ with time step $\delta t = \frac{T}{N}$: $t^{(n)} = n\delta t, n = 0,\ldots,N$.
Let T_h be a tetrahedral mesh of the domain Ω, and let X_D be the set of discrete unknowns associated to the vertices of T_h. Furthermore, let $X_{D,0} \subset X_D$ stand for the subset of X_D devoted to the approximation of the problem with homogeneous Dirichlet boundary condition on Γ_p.
Let the linear mapping $\Pi_D : X_D \to L^2(\Omega)$ be the piecewise constant reconstruction of the

approximate function such that

$$\Pi_D v = \sum_{i\in N_D} v_i \chi_{K_i}, \text{ for all } v = (v_i)_{i\in N_D} \in X_D, \tag{4.4.2}$$

where χ_{K_i} is the characteristic function of K_i and the family $(K_i)_{i\in N_D}$ constitute the barycentric dual mesh and is obtained by splitting each tetrahedron in subsets defined by the highest barycentric coordinate and defining K_i as the union of subsets connected to the vertex indexed by i.

Let $\nabla_D : X_D \to L^2(\Omega)^3$ be the discrete gradient operator such that

$$\nabla_D v = \sum_{i\in N_D} v_i \nabla \xi_i, \text{ for all } v = (v_i)_{i\in N_D} \in X_D, \tag{4.4.3}$$

where $(\xi_i)_{i\in N_D}$ is the set of shape functions of the usual piecewise linear finite element method.

This spatial discretization scheme corresponds to the case of linear P_1 finite elements with mass lumping.

We can now define the following implicit scheme for the discretization of problem (4.4.1): for given $u_{cD}, \overline{h_0}_D \in X_D$, find a sequence $(h^{(n)}, u^{(n)})_{n=1,\dots,N} \subset X_D$ such that

$$\begin{cases} u^{(n+1)} - u_{cD} \in X_{D,0}, \\ h^{(0)} = \overline{h_0}_D, \\ \displaystyle\int_\Omega \phi(t^{(n+1)},x) \frac{\theta(\Pi_D h^{(n+1)}(x)) - \theta(\Pi_D h^{(n)}(x))}{\delta t} \Pi_D v(x) \mathrm{d}x \\ \displaystyle+ \int_\Omega \phi(t^{(n+1)},x) K(\theta(\Pi_D h^{(n+1)}(x))) \nabla_D (h^{(n+1)}(x) + z) \nabla_D v(x) \mathrm{d}x \\ \displaystyle+ \int_\Omega \psi(t^{(n+1)},x) K_r(t^{(n+1)},x) \nabla_D (u^{(n+1)}(x) + z) \nabla_D w(x) \mathrm{d}x \\ \displaystyle+ \int_\Omega \varepsilon^{-1} B(\phi(t^{(n+1)},x)) L_r(t^{(n+1)},x) (\Pi_D h^{(n+1)}(x) - \Pi_D u^{(n+1)}(x)) \Pi_D v(x) \mathrm{d}x \\ \displaystyle- \int_\Omega \varepsilon^{-1} B(\phi(t^{(n+1)},x)) L_r(t^{(n+1)},x) (\Pi_D h^{(n+1)}(x) - \Pi_D u^{(n+1)}(x)) \Pi_D w(x) \mathrm{d}x = 0, \\ \forall v \in X_D, \quad \forall w \in X_{D,0}, \quad \forall n = 0, \dots, N-1. \end{cases} \tag{4.4.4}$$

4.4.2 Nutrient model

In problem (4.3.11) the transport component is handled by the method of characteristics. The transport part is of the form

$$\phi(\theta + \varphi'(c)) \partial_t c + \phi q.\nabla c = 0, \tag{4.4.5}$$

which can be written as

$$\partial_t c + \frac{q}{\theta + \varphi'(c)}.\nabla c = 0. \tag{4.4.6}$$

Denoting the velocity field $\frac{q}{\theta+\varphi'(c)}$ by a, the exact characteristics $\mathcal{X}(s,t^{(n+1)},x)$ satisfies

$$\frac{d\mathcal{X}(s,t^{(n+1)},x)}{ds} = a(s,\mathcal{X}(s,t^{(n+1)},x)), \quad s \in (t^{(n)},t^{(n+1)}), \quad \mathcal{X}(t^{(n+1)},t^{(n+1)},x) = x \tag{4.4.7}$$

which can be approximated by an implicit Euler scheme:

$$x - \mathcal{X}(t^{(n)},t^{(n+1)},x) \approx \delta t\, a(t^{(n+1)},x). \tag{4.4.8}$$

Using $X^{(n)}(x) = x - \delta t\, a(t^{(n+1)},x)$ as an approximation of the characteristics $\mathcal{X}(t^{(n)},t^{(n+1)},x)$, we can write the following semi-discrete implicit scheme corresponding to problem (4.3.11): determine $c^{(n+1)}$ successively for $n = 0,...,N-1$ such that

$$\begin{cases} c^{(0)} = \overline{c_0} & \text{in } \Omega, \\ \phi(t^{(n+1)})\dfrac{\theta^{(n)}c^{(n+1)} + \varphi(c^{(n+1)}) - \theta^{(n)}c^{(n)} \circ X^{(n)} - \varphi(c^{(n)} \circ X^{(n)})}{\delta t} & \\ -\nabla.\big(\phi(t^{(n+1)})A^{(n+1)}\nabla c^{(n+1)}\big) & \\ +\varepsilon^{-1}B(\phi(t^{(n+1)}))\left(h(c^{(n+1)}) - L_r(t^{(n+1)})(h^{(n+1)} - u^{(n+1)})c^{(n+1)}\right) = 0 & \text{in } \Omega, \\ -\phi(t^{(n+1)})A^{(n+1)}\nabla c^{(n+1)}.\vec{n_0} = 0 & \text{on } \Gamma. \end{cases} \tag{4.4.9}$$

As explained in chapter 3, section 3.3.1 and following [64], the water content θ is evaluated at time $t^{(n)}$ in order to reduce mass balance errors.
The corresponding fully discrete scheme for problem (4.3.11) then reads: for a given $\overline{c_0}_D \in X_D$, find a sequence $(c^{(n)})_{n=1,...,N} \subset X_D$ such that

$$\begin{cases} c^{(0)} = \overline{c_0}_D, \\ \displaystyle\int_\Omega \phi(t^{(n+1)},x)\frac{\theta(\Pi_D h^{(n)}(x))\Pi_D c^{(n+1)}(x) + \varphi(\Pi_D c^{(n+1)}(x))}{\delta t}\Pi_D v(x)\mathrm{d}x \\ \displaystyle -\int_\Omega \phi(t^{(n+1)},x)\frac{\theta(\Pi_D h^{(n)}(x))\Pi_D c^{(n)}(X^{(n)}(x)) + \varphi(\Pi_D c^{(n)}(X^{(n)}(x)))}{\delta t}\Pi_D v(x)\mathrm{d}x \\ \displaystyle +\int_\Omega \phi(t^{(n+1)},x)A(\theta(\Pi_D h^{(n+1)})(x))\nabla_D c^{(n+1)}(x)\nabla_D v(x)\mathrm{d}x \\ \displaystyle -\int_\Omega \varepsilon^{-1}B(\phi(t^{(n+1)},x))L_r(t^{(n+1)},x)(\Pi_D h^{(n+1)}(x) - \Pi_D u^{(n+1)}(x))\Pi_D c^{(n+1)}(x)\Pi_D v(x)\mathrm{d}x \\ \displaystyle +\int_\Omega \varepsilon^{-1}B(\phi(t^{(n+1)},x))h(\Pi_D c^{(n+1)}(x))\Pi_D v(x)\mathrm{d}x = 0,\ \forall v \in X_D, \quad \forall n = 0,...,N-1. \end{cases} \tag{4.4.10}$$

Nonlinearities in both problems (4.4.4) and (4.4.10) are handled by Newton's method.

Remark that the terms $\theta\partial_t\phi$ and $\varphi(c)\partial_t\phi$ corresponding to the boundary terms θV and $\varphi(c)V$ on Γ_r induced by root growth have been omitted in the numerical schemes. Numerical tests have shown that the contribution of these terms is negligible when considering realistic root shapes and root systems, which can be related to the experimental observation that the contribution of the interception mechanism to root uptake is negligible for most nutrients [3]. Moreover, accounting for these terms leads to the appearance of non-physical values of h and c in the region $\phi << 1$ which, when combined with transient mesh adaptation and interpolation between meshes, can affect the stability of the numerical method.

4.4.3 Preserving positivity

The solution c of the convection-diffusion equation naturally remains non-negative, and this important qualitative property should carry over to its discrete counterpart, in order to avoid meaningless and unstable numerical computations. In the following we propose a modification of the numerical scheme that produces a positive discrete solution under some geometrical constaints on the mesh and assuming positive initial data.
Let $n \in \{0,...,N-1\}$ and suppose that $c_i^{(n)} \geq 0 \, \forall i \in N_D$.
Scheme (4.4.10) reads: $\forall i \in N_D$,

$$\begin{aligned}
&\int_\Omega \frac{\phi(t^{(n+1)},x)}{\delta t} \sum_{j\in N_D} \left(\theta(h_j^{(n)})c_j^{(n+1)} + \varphi(c_j^{(n+1)})\right)\chi_{K_j}(x)\chi_{K_i}(x)\\
&+ \int_\Omega \phi(t^{(n+1)},x)\left(\sum_{k\in N_D} A(\theta(h_k^{(n+1)}))\chi_{K_k}(x)\right)\left(\sum_{j\in N_D}(c_j^{(n+1)})\nabla\xi_j(x)\right)\nabla\xi_i(x)\\
&+ \int_\Omega \varepsilon^{-1}B(\phi(t^{(n+1)},x))\sum_{j\in N_D}(h(c_j^{(n+1)}) - L_r(t^{(n+1)},x)(h_j^{(n+1)}-u_j^{(n+1)})c_j^{(n+1)})\chi_{K_j}(x)\chi_{K_i}(x)\\
&= \int_\Omega \frac{\phi(t^{(n+1)},x)}{\delta t}\left(\theta(\Pi_D h^{(n)}(x))\Pi_D c^{(n)}(X^{(n)}(x)) + \varphi(\Pi_D c^{(n)}(X^{(n)}(x)))\right)\chi_{K_i}(x).
\end{aligned} \tag{4.4.11}$$

Here we used the two following properties:

$$\begin{cases} g(\Pi_D u(x)) = \Pi_D g(u)(x), \ \text{ for a.e } x\in\Omega, \ \forall u\in X_D, \ \forall g\in C(\mathbb{R}),\\ \Pi_D u(x)\Pi_D v(x) = \Pi_D(uv)(x), \ \text{ for a.e } x\in\Omega, \ \forall u,v\in X_D. \end{cases} \tag{4.4.12}$$

Now, let

$$\begin{cases}
m_i = \displaystyle\int_\Omega \frac{\phi(t^{(n+1)},x}{\delta t}\chi_{K_i}(x),\\
\gamma_{i,j} = \displaystyle\int_\Omega \phi(t^{(n+1)},x)\sum_{k\in N_D} A(\theta(h_k^{(n+1)}))\chi_{K_k}(x)\nabla\xi_j(x)\nabla\xi_i(x),\\
b_i = \displaystyle\int_\Omega \varepsilon^{-1}B(\phi(t^{(n+1)},x))\chi_{K_i}(x),\\
\beta_i = \displaystyle\int_\Omega \varepsilon^{-1}B(\phi(t^{(n+1)},x))L_r(t^{(n+1)},x)\chi_{K_i}(x),\\
g_i = \displaystyle\int_\Omega \frac{\phi(t^{(n+1)},x)}{\delta t}\left(\theta(\Pi_D h^{(n)}(x))\Pi_D c^{(n)}(X^{(n)}(x)) + \varphi(\Pi_D c^{(n)}(X^{(n)}(x)))\right)\chi_{K_i}(x).
\end{cases} \tag{4.4.13}$$

Then (4.4.11) reads: $\forall i \in N_D$,

$$m_i \left(\theta(h_i^{(n)})c_i^{(n+1)} + \varphi(c_i^{(n+1)})\right) + \sum_{j\in N_D} \gamma_{i,j} c_j^{(n+1)} + b_i h(c_i^{(n+1)}) \\ - \beta_i(h_i^{(n+1)} - u_i^{(n+1)})c_i^{(n+1)} = g_i. \quad (4.4.14)$$

Here we used the fact that for almost every $x \in \Omega$,

$$\chi_{K_i}(x)\chi_{K_j}(x) = \begin{cases} \chi_{K_i}(x) & \text{for } i = j, \\ 0 & \text{for } i \neq j. \end{cases} \quad (4.4.15)$$

Applying Newton's method yields the corresponding linear problem: find $(c_i)_{i\in N_D} \in X_D$ such that $\forall i \in N_D$,

$$\begin{aligned} &\left(m_i\theta(h_i^{(n)}) - \beta_i(h_i - u_i)\right) c_i + \sum_{j\in N_D} \gamma_{i,j} c_j^{(n+1)} + \left(m_i\varphi'(c_i^{[k]}) + b_i h'(c_i^{[k]})\right) c_i \\ &= \left(m_i\varphi'(c_i^{[k]}) + b_i h'(c_i^{[k]})\right) c_i^{[k]} - m_i\varphi(c_i^{[k]}) - b_i h(c_i^{[k]}) + g_i, \end{aligned} \quad (4.4.16)$$

where $[k]$ is the inner iteration counter. The initial guess is chosen as $c^{[0]} = c^{(n)}$.
Now, let k be fixed and suppose that $c_i^{[k]} \geq 0 \ \forall i \in N_D$.

Problem (4.4.16) can be written in matrix form

$$(\boldsymbol{M} + \boldsymbol{K})\boldsymbol{c} = \boldsymbol{f}, \quad (4.4.17)$$

where $\boldsymbol{M}$ is diagonal and

$$\begin{cases} \boldsymbol{M} = [M_{ii}]_{N_D\times N_D}, \quad M_{ii} = \left(m_i\theta(h_i^{(n)}) - \beta_i(h_i - u_i)\right) + \left(m_i\varphi'(c_i^{[k]}) + b_i h'(c_i^{[k]})\right), \\ \boldsymbol{K} = [K_{ij}]_{N_D\times N_D}, \quad K_{ij} = \gamma_{i,j}, \\ \boldsymbol{f} = [f_i]_{N_D}, \quad f_i = \left(m_i\varphi'(c_i^{[k]}) + b_i h'(c_i^{[k]})\right) c_i^{[k]} - m_i\varphi(c_i^{[k]}) - b_i h(c_i^{[k]}) + g_i, \\ \boldsymbol{c} = [c_i]_{N_D}. \end{cases} \quad (4.4.18)$$

Similarly to what is done for establishing classical discrete maximum principles for elliptic problems [7], it is sufficient to show that $\boldsymbol{M} + \boldsymbol{K}$ is a non-singular M-matrix (and thus has non-negative inverse) and that $\boldsymbol{f} \geq 0$ in order to ensure that $\boldsymbol{c} \geq 0$.
Now, note that $\forall i \in N_D$,

$$\sum_{j\in N_D} K_{ij} = \int_\Omega \sum_{k\in N_D} A(\theta(h_k^{(n+1)}))\chi_{K_k}(x) \left(\sum_{j\in N_D} \nabla\xi_j(x)\right) \nabla\xi_i(x) = 0. \quad (4.4.19)$$

Thus, sufficient conditions to ensure that $\boldsymbol{c} \geq 0$ are

$$\begin{cases} M_{ii} > 0 \quad \forall i \in N_D, \\ K_{ij} \leq 0 \quad \forall i, j \in N_D,\ i \neq j, \\ f_i \geq 0 \quad \forall i \in N_D. \end{cases} \quad (4.4.20)$$

The condition

$$\nabla\xi_i\nabla\xi_j \leq 0 \quad \forall i,j\in N_D,\ i\neq j \tag{4.4.21}$$

guarantees that the off-diagonal entries of $\boldsymbol{K}$ are non-positive. Condition (4.4.21) is related to the well known non-obtuse angle condition that requires the dihedral angles of all elements of the mesh T_h to be non-obtuse.

In order to ensure that $M_{ii} > 0$ and $f_i \geq 0$ for all i in N_D, we introduce a modified Newton's method based on an altered Jacobian. Since $m_i, b_i > 0$ and $\varphi', h' > 0$, we can compute the smallest $\nu_i >= 1$ such that

$$\begin{cases} \left(m_i\theta(h_i^{(n)}) - \beta_i(h_i-u_i)\right) + \nu_i\left(m_i\varphi'(c_i^{[k]}) + b_ih'(c_i^{[k]})\right) > 0, \\ \nu_i\left(m_i\varphi'(c_i^{[k]}) + b_ih'(c_i^{[k]})\right)c_i^{[k]} - m_i\varphi(c_i^{[k]}) - b_ih(c_i^{[k]}) + g_i \geq 0. \end{cases} \tag{4.4.22}$$

The coefficients ν_i can be related to the concept of under-relaxation in damped Newton's methods.
The modified Newton's method then consists in replacing the terms M_{ii} and f_i in (4.4.18) with

$$\begin{cases} M_{ii} = \left(m_i\theta(h_i^{(n)}) - \beta_i(h_i-u_i)\right) + \nu_i\left(m_i\varphi'(c_i^{[k]}) + b_ih'(c_i^{[k]})\right), \\ f_i = \nu_i\left(m_i\varphi'(c_i^{[k]}) + b_ih'(c_i^{[k]})\right)c_i^{[k]} - m_i\varphi(c_i^{[k]}) - b_ih(c_i^{[k]}) + g_i, \end{cases} \tag{4.4.23}$$

where the derivative has been multiplied by the coefficient ν_i.
Note that if $c_i^{[k]} = 0$, we have that $\varphi(c_i^{[k]}) = h(c_i^{[k]}) = 0$ and thus $f_i \geq 0$ since $g_i \geq 0$.

In the practical numerical implementation and when considering root growth and transient mesh adaptation, the mesh adaptation procedure does not guarantee the non-obtuse angle condition, which is actually quite restrictive. Thus, some numerical values of the concentration can become negative, although the magnitude of the negative values remains small, and the functions φ and h need to be extended to $c < 0$. In our case, where φ and h are given by (4.2.14, 4.2.18), we simply choose to extend φ and φ' by 0 for $c \leq 0$, although smoother extensions can be considered (see for example section 2.4 in chapter 2). Besides, we can keep h as the original Michaelis-Menten function (4.2.18) for $c < 0$ and the method remains stable in all numerical tests as the magnitude of the negative values is small enough.

Another thing to note is that the damping (4.4.22) introduced in the modified Newton's method takes effect only in the case of high transpiration rates (where $\beta_i(h_i - u_i)$ can be large) and does not significantly affect the convergence rate of the Newton's method.

4.4.4 Numerical integration

In problems (4.4.4) and (4.4.10), integrals such as (4.4.13) cannot be computed exactly and have to be approximated by numerical integration. Remark that although the $\nabla\chi_i$ are constant on each element of the mesh T_h, the χ_{K_i} are discontinuous on each element intersecting their support. A simple way to avoid discontinuous integrands is to split each tetrahedron of T_h according to the barycentric dual mesh, the four polygons defined by the highest barycentric coordinate each split into six tetrahedra as depicted in Fig. 4.2. Thus, all integrands are continuous on each of these tetrahedra, over which we can then use standard Gaussian quadrature rules. It is important to note that this splitting algorithm does not generate additional degrees of freedom and is only used for numerical integration.

On a similar note, we can devise an adaptive quadrature algorithm in order to improve the accuracy of the approximation of the phase field function for the purpose of numerical integration. We can use the P1 approximation r_D of the signed distance function to the root system r to define a piecewise planar representation of the root surface defined by $r_D = 0$ that cuts through the mesh and splits each intersected tetrahedron into two polygons, which are then subdivided into tetrahedras. Since Gaussian quadrature rules tend to concentrate integration points near the edges, this ensures a larger number of quadrature points near $r = 0$ where ϕ and $B(\phi)$ show high gradients. This procedure is illustrated in Fig. 4.3.

In practice, numerical tests have shown that it is unnecessary to combine the two splitting algorithms, and that applying only the second adaptive splitting procedure based on r_D on the original mesh yields very good results while using much less integration points even though integrands are discontinuous.

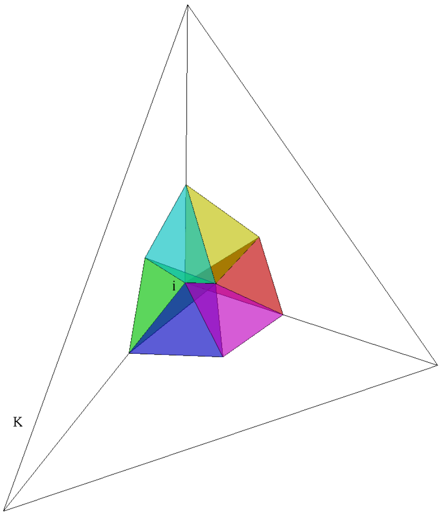

Figure 4.2 The intersection of K_i with element K is split into 6 tetrahedra

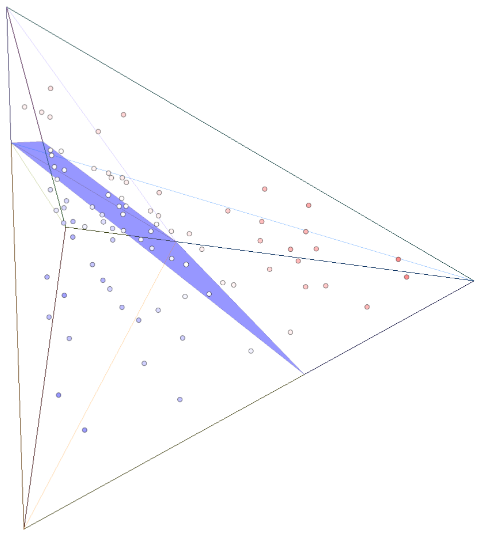

Figure 4.3 An element is split along the surface defined by $r_D = 0$ (in blue). Integration points from a 15-point Gaussian quadrature rule are colored according to the value of ϕ.

4.5 The root system

As in chapter 3, we consider that the root system is composed of cylindrical root segments and we use RootBox [46], a root growth model based on L-Systems, to generate the tree-like network of segments $\Sigma(t)$ representing the root system. A description of RootBox is given in chapter 3, section 3.2.2.

At the discrete level, new root segments are added at each time step as the root system develops, each segment with its own parameters (radius, age, conductivity, ...).

Let $\Sigma^{(n)}$ be the set of segments representing the root system at time $t^{(n)}$.

The signed distance $r(t^{(n)},x)$ of a point x to the root surface $\Gamma_r(t^{(n)})$ is then given by

$$r(t^{(n)},x) = -\min_{s\in\Sigma^{(n)}} (d_s(x) - r_s)\,, \tag{4.5.1}$$

where $d_s(x)$ is the distance of x to the segment s and r_s is the radius of segment s.

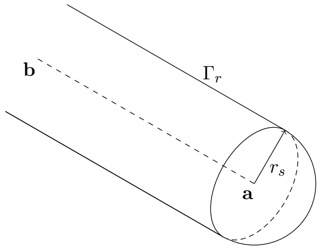

Figure 4.4 Root surface Γ_r of a root tip represented by segment $(\mathbf{a},\mathbf{b})$

Since the value of the phase field function ϕ (4.3.4) is non-trivial only in a neighborhood of Γ_r, the signed distance function r used in the computation of ϕ is relevant solely in the vicinity of the root system. Thus, we only need to consider a subset $\Sigma_x^{(n)} \subset \Sigma^{(n)}$ of root segments close enough to x when computing $r(t^{(n)},x)$.
To this end, we define a regular partition of the domain Ω, subdividing it into $N_b \times N_b \times N_b$ boxes. We then define for each box B the subset $\Sigma_B^{(n)} \subset \Sigma^{(n)}$ containing segments relevant to the computation of $r(t^{(n)},x)$ for any x in box B, namely segments located in B as well as in all boxes adjacent to B.
This preliminary grouping of segments into subsets $\Sigma_B^{(n)}$ allows to speed up the computation of the signed distance function: for each subsequent computation of $r(t^{(n)},x)$ only segments in $\Sigma_x^{(n)}$ are considered, where $\Sigma_x^{(n)} = \Sigma_B^{(n)}$, $B \ni x$.
The algorithm used for the computation of $r(t^{(n)},x)$ is as follows:

```
Data: $\mathbf{x}$
Result: $r(t^{(n)},\mathbf{x})$
$r \leftarrow +\infty$;
find the box $B$ containing $\mathbf{x}$;
for each $s \in \Sigma_B^{(n)}$ do
    let $(\mathbf{a},\mathbf{b})$ be the two nodes forming segment $s$;
    if $(\mathbf{x}-\mathbf{a})\cdot(\mathbf{b}-\mathbf{a}) < 0$ then
        $d \leftarrow |\mathbf{x}-\mathbf{a}|^2$;
    else if $(\mathbf{x}-\mathbf{b})\cdot(\mathbf{a}-\mathbf{b}) < 0$ then
        $d \leftarrow |\mathbf{x}-\mathbf{b}|^2$;
    else
        $d \leftarrow \frac{|(\mathbf{x}-\mathbf{a})\times(\mathbf{b}-\mathbf{a})|^2}{|\mathbf{b}-\mathbf{a}|^2}$;
    end
    $r \leftarrow \min(r, \sqrt{d} - r_s)$;
end
return $-r$
```

Algorithm 4.5 Computation of the signed distance $r(t^{(n)},x)$

4.6 Adaptive meshing

Unstructured mesh adaptation has largely proved its efficiency for improving the accuracy of numerical solutions. The mesh adaptation procedure allows to capture the behavior of local phenomena while substantially reducing the number of degrees of freedom by adjusting locally the mesh density, controlling the size, shape and orientation of mesh elements.

Here we make the following hypothesis: the quality of the numerical solutions to problems (4.4.4) and (4.4.10) depends on the quality of the approximation of the diffuse interface, which in turns depends on the quality of the approximation of the phase field function. Thus, the goal is to adapt the finite element mesh T_h of the domain Ω to the variations of ϕ, so as to resolve the diffuse interface as well as the potentially high gradient of the solution in the vicinity of the interface.

Furthermore, we make the hypothesis that the approximation error is controlled by the interpolation error. We then aim at generating an adapted mesh for which the interpolation error of the phase field function ϕ is equidistributed in all directions.

For an element K of the mesh, we have the following bound on the interpolation error based on the second-order derivatives of ϕ:

$$||\phi - \Pi\phi||_{\infty,K} \leq C \max_{x\in K} \max_{e\in E_K} \langle \vec{e}, |H_\phi(x)|\vec{e}\rangle \tag{4.6.1}$$

where Π is the linear interpolation operator on T_h, C is a constant depending on the dimension, E_K is the set of edges of element K and $|H_\phi| = \mathcal{R}|\Lambda|\mathcal{R}^{-1}$ is the absolute value of the hessian of ϕ, with $\mathcal{R}$ the matrix composed of the eigenvectors of H_ϕ and $|\Lambda| = \mathrm{diag}(\lambda_i)$ the diagonal matrix composed of the absolute values of the eigenvalues of H_ϕ.

Let us fix an error threshold ε_m; we want to commit an error of ε_m on each element K of the mesh:

$$C \max_{x\in K} \max_{e\in E_K} \langle \vec{e}, |H_\phi(x)|\vec{e}\rangle = \varepsilon_m. \tag{4.6.2}$$

A discrete metric field is then defined at the vertices of the mesh. Let us denote by $h_{\min}$ (resp. $h_{\max}$) the prescribed minimum (resp. maximum) edge length. At each mesh vertex we define an anisotropic metric tensor as:

$$\mathcal{M} = \mathcal{R}\tilde{\Lambda}\mathcal{R}^{-1} \quad \text{where} \quad \tilde{\Lambda} = \mathrm{diag}(\tilde{\lambda}_i) \tag{4.6.3}$$

and

$$\tilde{\lambda}_i = \min\left(\max\left(\frac{C|\lambda_i|}{\varepsilon_m}, \frac{1}{h^2_{\max}} \right), \frac{1}{h^2_{\min}} \right). \tag{4.6.4}$$

The goal is then to modify the mesh T_h iteratively by local operations in order to obtain a quasi-uniform mesh with respect to the prescribed metric: $l_{\mathcal{M}}(\vec{e}) \approx 1$ for every edge $\vec{e}$ of the mesh, where $l_{\mathcal{M}}(\vec{e})$ is the length of edge $\vec{e}$ in the metric $\mathcal{M}$. Since $\mathcal{M}$ is defined at the vertices of the mesh, we define the length of edge $\vec{e} = \overrightarrow{p_1 p_2}$ as:

$$l_{\mathcal{M}}(\vec{e}) = \int_0^1 \sqrt{{}^t\vec{e}\mathcal{M}(p_1 + t\overrightarrow{p_1 p_2})\vec{e}}\,\mathrm{d}t. \tag{4.6.5}$$

The code is interfaced with the `mshmet` library [19] for computing the metric and with the anisotropic tetrahedral automatic remesher Mmg3d [12] which uses an anisotropic Delaunay kernel and local mesh modifications based on a combination of edge flips, edge collapsing, node relocation and vertex insertion operations to adapt the mesh.

Note that the fine features of ϕ cannot be resolved accurately on an initial non-adapted coarse mesh, and some of them may be entirely overlooked when defining the metric $\mathcal{M}$ at the vertices of a coarse mesh. Thus, the practical implementation consists in performing several iterations of mesh adaptation while defining at each iteration i a suitable metric $\mathcal{M}_i$ guiding the mesh adaptation procedure. The idea is to construct metrics $(\mathcal{M}_i)$ by intersecting $\mathcal{M}$ with one or more metrics $\mathcal{M}_{\varepsilon_j}$, where $\varepsilon_j > \varepsilon$ and $\mathcal{M}_{\varepsilon_j}$ is computed from the hessian of ϕ_{ε_j}, the phase field function with a transition of width $2\varepsilon_j$. Decreasing values of ε_j are chosen during the iterations following appropriate heuristics so that the variations of ϕ_{ε_j} are captured on the current mesh, progressively guiding the mesh adaptation procedure towards locating and capturing the variations of ϕ.

A mesh gradation control procedure is also applied by bounding the variations of the metric field in all directions in order to improve the quality of the mesh.

Fig. 4.6 presents a general overview of the model through an example, showing the root system, the adapted mesh and the water potential.

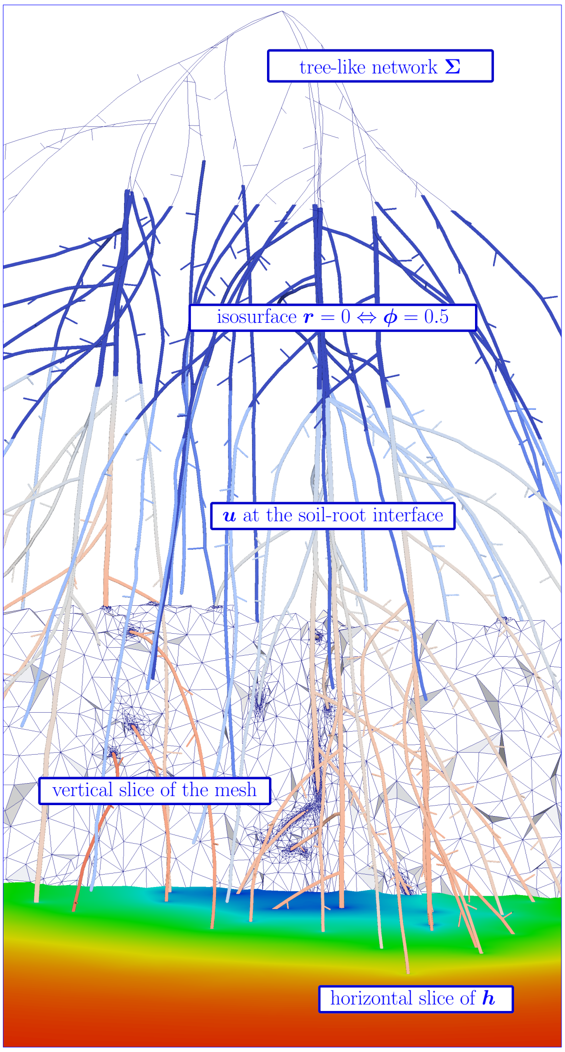

Figure 4.6 Overview of the model

4.7 Parallel implementation

This section shows how we can make use of parallel architectures in order to keep an affordable computing time when considering complex root systems, in the mesh adaptation procedure as well as for assembling and solving the linear systems. The parallel implementation is done using MPI.
Numerical tests were performed on the SGI Altix UV100 computer at Laboratoire Jacques-Louis Lions and on the CURIE French supercomputer operated by CEA.
Execution times of the different parts of the computation are given for the numerical example presented in section 4.8.2.

4.7.1 Assembling and solving the linear systems

Since the mesh is modified at each time step as the root system expands due to root growth, using a domain decomposition method as was done in chapter 3 presents additional difficulties and requires efficient load balancing and repartitioning algorithms. Instead, we choose to use a parallel direct solver.

Assembly of the linear systems arising from problems (4.4.4) and (4.4.10) can be parallelized in a straightforward manner, as it consists in loops over mesh elements, degrees of freedom or quadrature points. The linear systems are then solved by the multifrontal parallel sparse direct solver Mumps [1].

4.7.2 Parallel mesh adaptation

When considering root growth, the phase field function evolves at each time step due to new segments being added as the root system develops. Thus at time $t^{(n+1)}$, the mesh T_h has to be adapted only in a neighborhood of each new segment in $S := \Sigma^{(n+1)} \setminus \Sigma^{(n)}$.

Remark that if two new segments are sufficiently distant from each other, then their neighborhood consists of two non-overlapping subdomains, which can then be remeshed independently in parallel. This idea can be generalized to a subset $M \subset S$ of new segments, provided all segments in M have pairwise disjoint neighborhoods.
We can then devise an iterative algorithm which consists in computing such a subset $M \subset S$, extracting submeshes corresponding to the neighborhoods of the segments in M and performing mesh adaptation as described in section 4.6 on each submesh in parallel. This procedure is repeated a few times until all segments in S have been processed.

The parallel mesh adaptation algorithm is detailed below:

```
Data: mesh $T_h^{(n)}$ adapted to $\phi(t^{(n)})$
Result: mesh $T_h^{(n+1)}$ adapted to $\phi(t^{(n+1)})$

$T_h \leftarrow T_h^{(n)}$;
$S \leftarrow \Sigma^{(n+1)} \setminus \Sigma^{(n)}$;
while $S \neq \emptyset$ do
    $M \leftarrow \emptyset$;
    for each $s$ in $S$ do
        let $m_s$ be the midpoint of segment $s$;
        disj $\leftarrow$ true ;
        for each $p$ in $M$ do
            let $m_p$ be the midpoint of segment $p$;
            let $\lambda_r$ be the distance threshold between the two midpoints, which
            depends on the length of segments $s$ and $p$ and on the the maximum
            edge length of $T_h$;
            if $||m_s - m_p|| < \lambda_r$ then
                disj $\leftarrow$ false ;
            end
        end
        if disj is true then
            $M \leftarrow M \cup \{s\}$;
        end
    end
    for each $p$ in $M$ do in parallel
        extract a submesh $S_h^p \subset T_h$ composed of all elements $K \in T_h$ such that
        $K \cap B(m_p, \mu_r) \neq \emptyset$, where $B(m_p, \mu_r)$ is the ball of radius $\mu_r$ centered at the
        midpoint of segment $p$ and $\mu_r$ depends on the length of segment $p$ and on
        the the maximum edge length of $T_h$;
        for $i \leftarrow 1$ to $n_{iter}$ do
            compute the metric $\mathcal{M}_i$ defined at the vertices of $S_h^p$;
            adapt the volume mesh $S_h^p$ to obtain a quasi-unit mesh in the metric $\mathcal{M}_i$.
            The boundary of $S_h^p$ is preserved;
        end
    end
    gather the modified submeshes and reassemble the global mesh $T_h$;
    $S \leftarrow S \setminus M$;
end
return $T_h$
```

Algorithm 4.7 Parallel mesh adaptation

In this algorithm the λ_r and μ_r are chosen so that every submesh encloses a ball containing a sufficiently large neighborhood of the corresponding segment while guaranteeing that there are no intersection between any two submeshes.

4.8 Numerical experiments

We first test the efficiency of the diffuse domain approach by comparing the diffuse domain approximate solution to the solution of the original problem. We then present some numerical simulations of water and nutrient uptake of growing maize root systems showing the effects of different tropisms. Note that the purpose of this section is not to present quantitative results or perform sensitivity analysis, but rather to show the capability of the numerical model.
In all simulations, the computational domain is of dimensions 0.4 m × 0.4 m × 0.4 m. The time step δt is taken constant equal to 0.1 d. Parameters for a clay soil are taken as $\theta_m = 0.068$, $\theta_M = 0.38$, $\lambda = 0.17$, $h_b = -0.4$ m, $K_s = 0.144\,\mathrm{m\,d^{-1}}$.
The maize root systems generated by RootBox are composed of tap roots, first and second order laterals of radius 0.3 mm, 0.2 mm and 0.1 mm respectively.
Root parameters are taken constant across the whole root system, and numerical values of the radial conductivity L_r and the xylem conductance K_x for maize are taken from [13]: $L_r = 1.923\,08 \times 10^{-4}\,\mathrm{d^{-1}}$, $K_x = 4.32 \times 10^{-8}\,\mathrm{m^3\,d^{-1}}$.
As explained in section 4.2.1, we consider that Ω_r represents the xylem vessels. Thus, the conductivity K_r has to be taken equal to the xylem conductance K_x divided by the cross-sectional area of the root in order to recover the appropriate longitudinal flow.

4.8.1 Test case - convergence of the diffuse domain approach

In order to assess the quality of the diffuse domain approximation in a non-trivial case, we compare numerical solutions of the original (4.2.10) and diffuse domain (4.3.10) problems in the case of a root system composed of 545 root segments generated by RootBox.
We use tools developed in [10] for the purpose of generating the surface and volume meshes conforming to the root surface Γ_r corresponding to this root system:

- First, the background mesh of Ω is adapted to the phase field function ϕ as described in section 4.6. We obtain a mesh $\mathcal{T}_D$ of Ω which is the support of a good P1 approximation r_D of the signed distance function to the root system r near the root. $\mathcal{T}_D$ is the mesh that is used for the diffuse domain method.
- Then, a new mesh $\mathcal{T}_C$ is generated from $\mathcal{T}_D$ containing an explicit discretization of the 0 level set of r_D.
- Finally, $\mathcal{T}_C$ is modified using tools developed in [10] so that a new well-shaped mesh $\tilde{\mathcal{T}_C}$ is obtained, which contains a well-shaped close approximation of the boundary Γ_r. The original problem (4.2.10) is solved on $\tilde{\mathcal{T}_C}$.

In this test case, the initial water potential in the soil domain is homogeneous: $h_0 = -15$ m. A constant water potential $u_c = -100$ m is imposed at the root collar.

A comparison of the results between the original (4.2.10) and diffuse domain (4.3.10) problems after a simulation time of one day is depicted in Figs. 4.8 and 4.9.

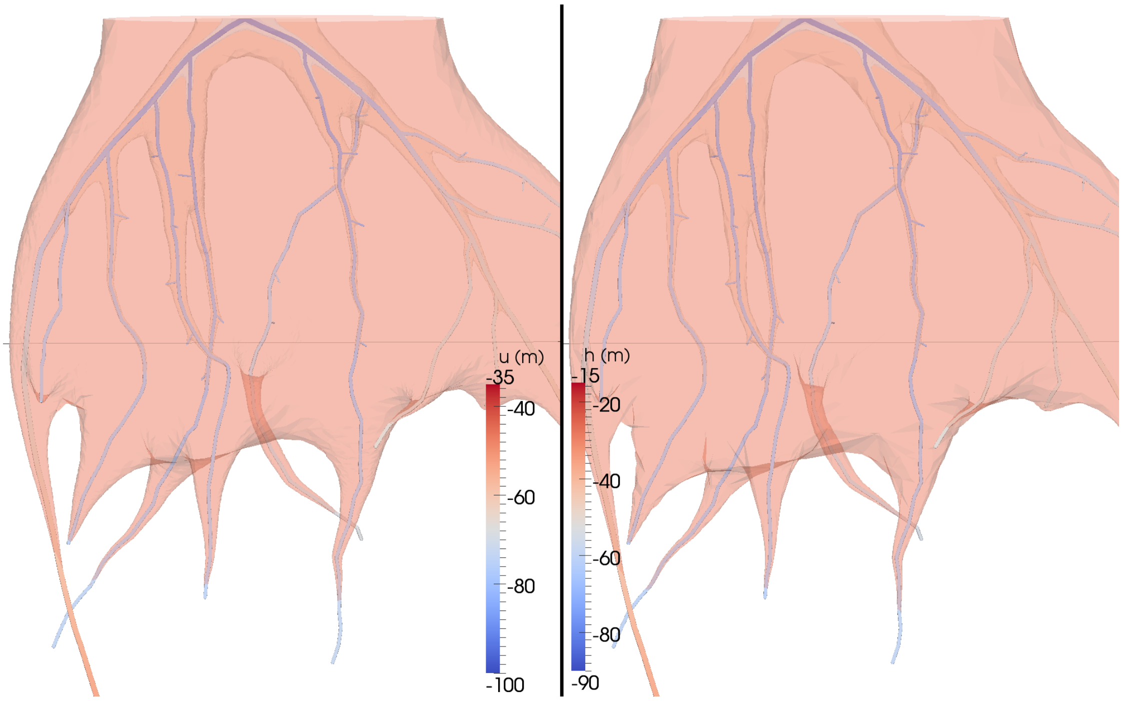

Figure 4.8 Left: solution to the original problem (4.2.10). Right: solution to the diffuse domain approximation (4.3.10)

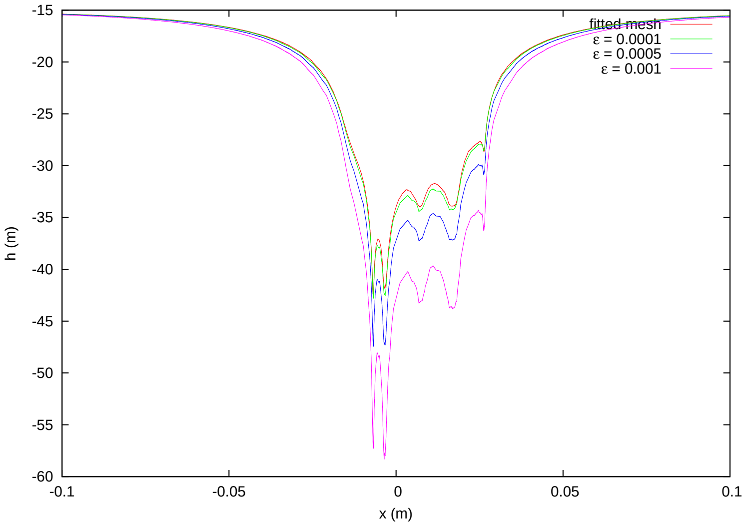

Figure 4.9 Comparison of the value of h on the line depicted in Fig. 4.8 for the original problem (4.2.10) and for the diffuse domain problem (4.3.10) with different values of ε

4.8.2 Nitrate uptake by a growing maize root system

This example is a simulation of water and nitrate uptake by a maize root system and shows the effects of chemotropism on root growth. Chemotropism is included by coupling the model with the implementation of growth and tropisms in RootBox, similar to what was done in the 2D example presented in chapter 3 section 3.7. As explained in 3.7, RootBox simulates root tip response to various types of tropisms through random minimization of an objective function. For each active root tip, several rotations are randomly chosen and the value of the objective function at each new potential root tip position is computed. The growth direction corresponding to the smallest value of the objective function is retained.
In this example, we consider a combination of gravitropism and chemotropism by defining the objective function f_o as

$$f_o = -\lambda c + z, \tag{4.8.1}$$

where $\lambda > 0$ represents the relative strength of chemotropism.
At time $t^{(n+1)}$, the coupling algorithm simply consists in computing the value of f_o at each new potential tip position by linear interpolation of $c^{(n)}$ on the mesh for each active root tip. Then, RootBox generates new root segments based on the best growth direction for each root tip.

In this simulation, the initial water potential in the soil domain is $h_0 = -5$ m. A constant water potential $u_c = -50$ m is imposed at the root collar.
The diffusion coefficient of nitrate in free water $A_0 = 1.6416 \times 10^{-4}\ \mathrm{m^2\,d^{-1}}$ is taken from [4], as well as parameters in the definition of the tortuosity factor (4.2.13): $f_1 = 1.58$, $f_2 = -0.17$, $\theta_l = 0.12$.
As nitrate is hardly adsorbed by the soil, we take $\varphi = 0$.
Michaelis-Menten parameters for nitrate uptake by maize are taken from [3]: $F_m = 8.64 \times 10^{-3}\ \mathrm{mol\,m^{-2}\,d^{-1}}$, $K_m = 2.5 \times 10^{-2}\ \mathrm{mol\,m^{-3}}$.
The initial nitrate concentration c_0 is a linear function of the y-coordinate ranging from 0 $\mathrm{mol\,m^{-3}}$ to 2 $\mathrm{mol\,m^{-3}}$.

Fig. 4.10 presents five snapshots taken during the simulation showing the development of the root system and the evolution of the concentration. Fig. 4.11 shows a horizontal slice of the concentration after a simulation time of 37 days.

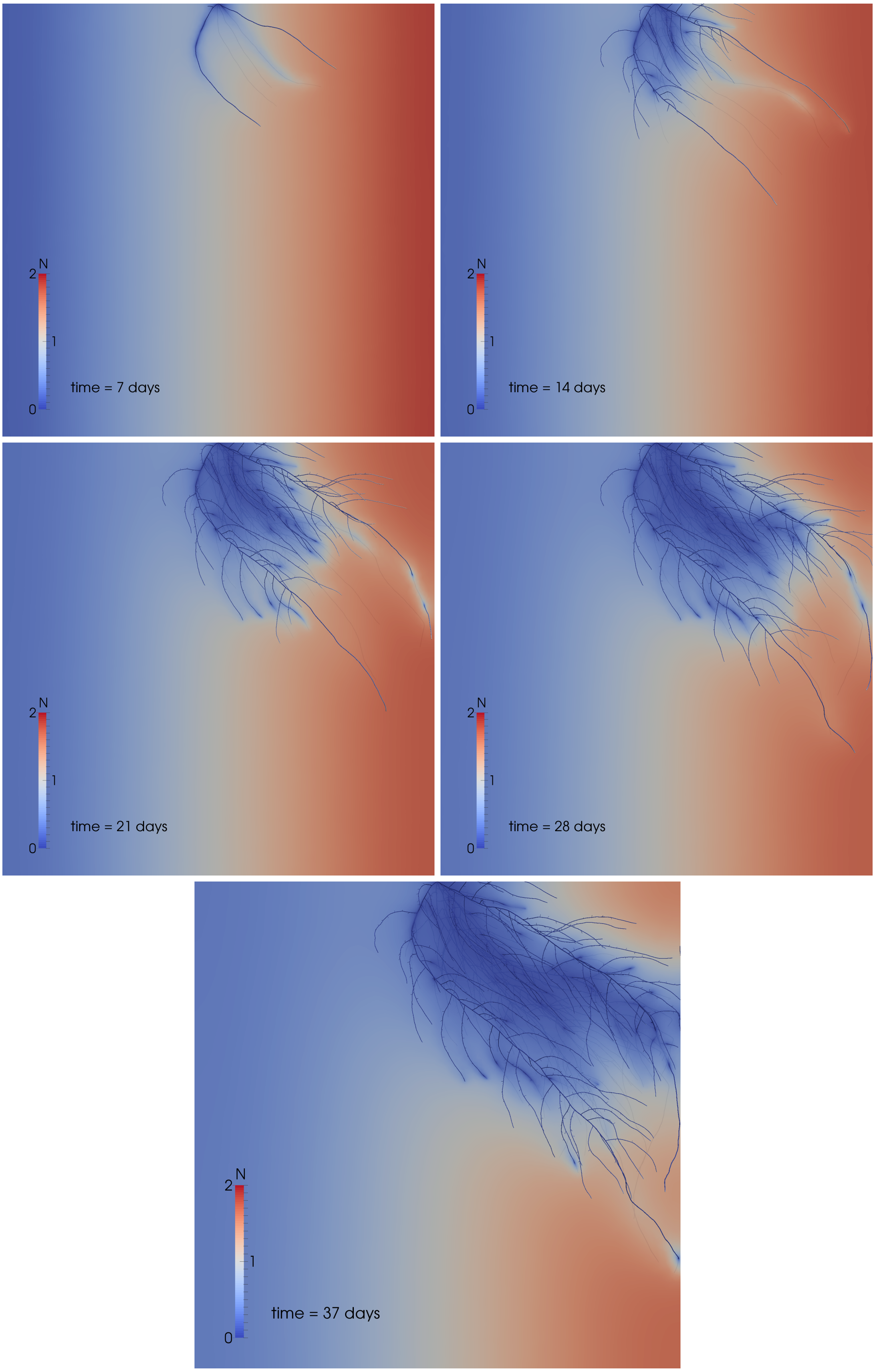

Figure 4.10 Vertical slice showing nitrate concentration at different time steps of the simulation

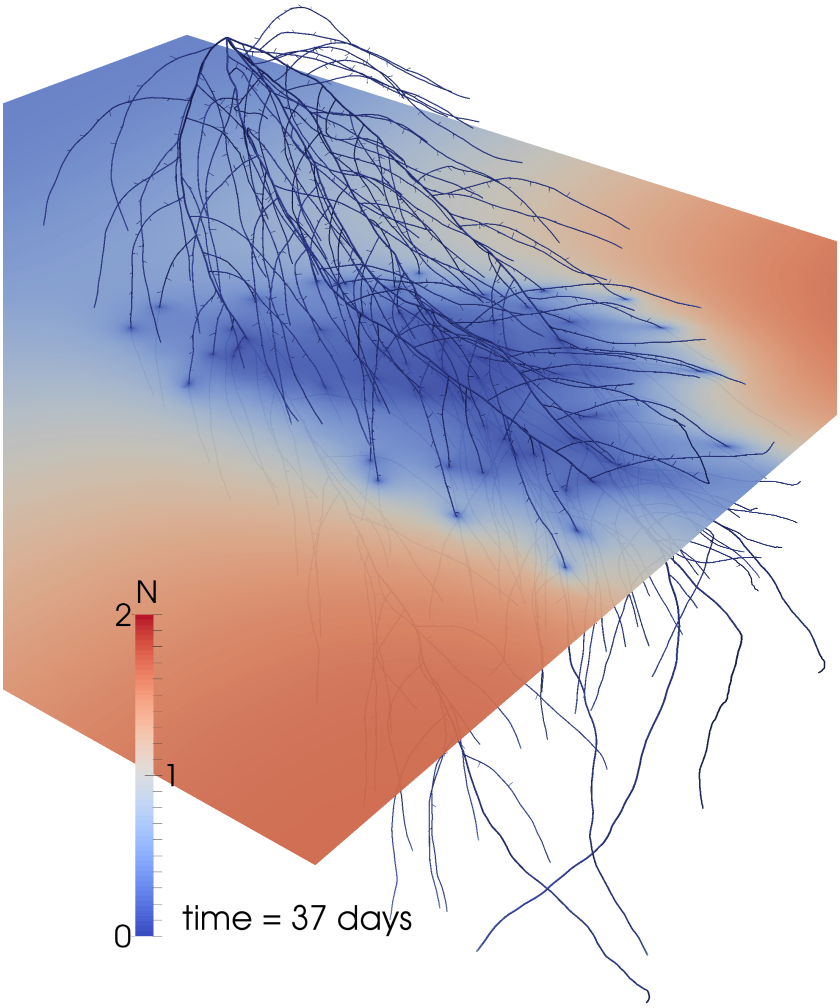

Figure 4.11 Horizontal slice showing nitrate concentration after 37 days

In the following we give some numbers regarding the different parts of the computation for the last time step:

- The root system is composed of 10024 root segments.
- The mesh is composed of 3 927 132 vertices and 22 770 256 tetrahedra.
- Parallel mesh adaptation algorithm 4.7: 16 processors, execution time of 1066 s.
- Assembling and solving the linear systems on 64 processors:
  - Computing the signed distance r for each quadrature point: 907 s.
  - 7 and 10 nonlinear iterations for the water and nutrient problems respectively.
  - Lagrangian step in the method of characteristics: 52 s.
  - Assembling the linear systems: 6 s on average.
  - Solving the linear system for the water problem: 96 s on average.
  - Solving the linear system for the nutrient problem: 33 s on average.

Note that the signed distance function r is computed for every quadrature point in the mesh. Computing r only in the neighborhood of new segments and reusing computations done on the previous mesh should reduce the computation time significantly.

4.8.3 Water and phosphate uptake

This example is a simulation of water and phosphate uptake by a growing maize root system and includes hydrotropism. As in the previous example, hydrotropism is introduced by defining the objective function as $f_o = -\lambda h + z$, where $\lambda > 0$ represents the relative strength of hydrotropism.

In this simulation, the initial water potential in the soil domain is $h_0 = -10$ m. A constant water potential $u_c = -150$ m is imposed at the root collar.

Fig. 4.12 shows the root systems resulting from two different strengths of hydrotropism after a simulation time of 37 days.

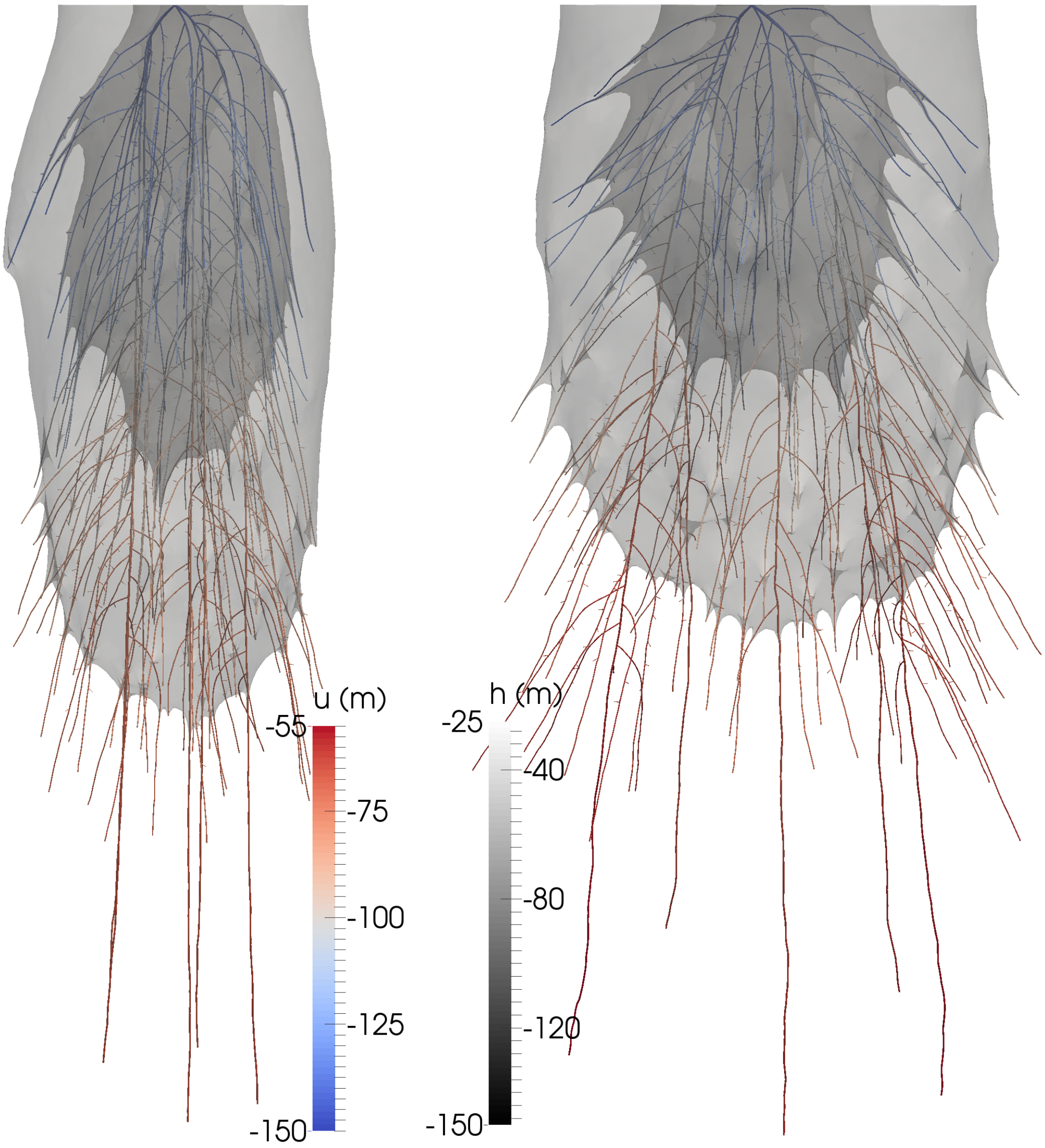

Figure 4.12 Root water potential u and isosurfaces of the soil water potential h for two root systems corresponding to two different values of λ after a simulation time of 37 days

Model parameters for phosphate are taken as follows:

— $A_0 = 7.59 \times 10^{-4}\ \mathrm{m^2\,d^{-1}}$.

— Freundlich coefficients are taken from [56]: $\kappa = 6.15$, $b = 0.72$.

— Michaelis-Menten parameters for phosphate uptake by maize are taken from [74]: $F_m = 1.91 \times 10^{-4}\ \mathrm{mol\,m^{-2}\,d^{-1}}$, $K_m = 2.3 \times 10^{-3}\ \mathrm{mol\,m^{-3}}$.

— The homogeneous initial concentration of phosphate in the soil solution is $c_0 = 2.3 \times 10^{-3}\ \mathrm{\mu mol\,cm^{-3}}$.

Fig. 4.13 shows the phosphate concentration near a portion of the root system after 37 days for the simulation corresponding to the case shown on the right-hand side of Fig. 4.12. As expected, for a poorly mobile nutrient such as P steep concentration gradients and narrow depletion zones develop around the roots.

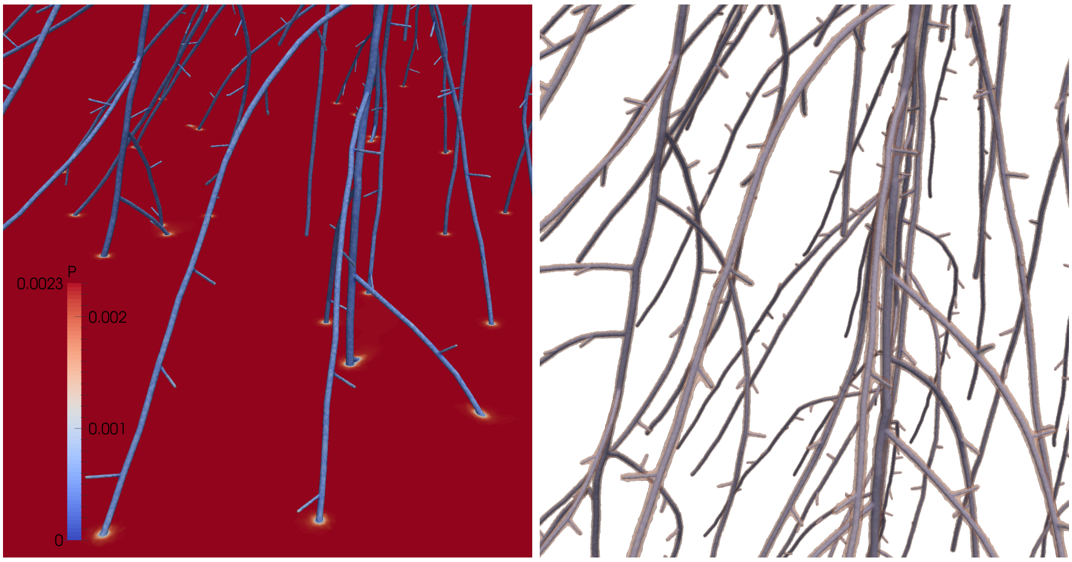

Figure 4.13 Horizontal slice (left) and isosurfaces (right) of the concentration of phosphate in the soil solution

4.9 Conclusion

In this chapter, we presented a diffuse domain approach for a model of soil water movement and solute transport together with root water and nutrient uptake and root growth. The model takes into account the actual surface of the root as a boundary between the soil domain and the root system. The root surface is implicitly described as the 0 level set of a signed distance function and the sharp boundary is replaced with a narrow diffuse interface, allowing us to avoid the difficulty of generating a surface mesh of the soil-root interface for complex root systems.

The model takes advantage of unstructured mesh adaptation in order to resolve the diffuse interface as well as high gradients in the vicinity of the roots.

A parallel approach was considered in order to keep an affordable computing time.
Finally, numerical experiments were performed to show the effectiveness of the diffuse domain approach and illustrate the capabilities of the model.
The model can be used in future studies to investigate more elaborate scenarios including for example day-night sinusoidal transpiration, irrigation and fertilizer application.

It is important to note that the coupled problem of soil and root water flow was formulated and solved in a monolithic way, whereas the water model presented in chapter 3 involved an iterative coupling algorithm between the soil and the root network. This strong coupling allowed us to maintain the quadratic convergence rate of Newton's method for the full problem.
Furthermore, the radial flux at the soil-root interface $L_r(h-u)$ coupling both problems is linear in both h and u, which is why we chose not to apply the Kirchhoff transformation as was done in chapter 3. Using the Kirchhoff transformation would eliminate the nonlinearity in front of the spatial derivative in Richards equation but would also introduce a nonlinearity in the coupling.

Chapter 5

Conclusion and perspectives

In chapter 2, we conducted the mathematical analysis of a model of root P uptake and formulated a shape optimization problem designed to find root shapes maximizing P uptake at the root surface.
In chapters 3 and 4, we proposed numerical models of soil water and solute movement with root water and nutrient uptake that are capable of resolving the complex geometry of root systems as well as local processes at the soil-root interface by taking advantage of advanced mesh adaptation and parallelization techniques. In particular, in chapter 4 we considered the soil-root interface explicitly as well as root growth and chemotropism.
Such models can be used to assess the effect of various parameters in a large range of simulation scenarios as well as quantify the impact of root architecture and rhizosphere processes on the overall uptake pattern.
They can help us improve our understanding of plant-soil relationships and also provide valuable insight for developing simpler models that capture the effective uptake behavior more correctly and ultimately establishing sustainable crop management protocols.

Several features of the modeling framework considered in this thesis can be improved, particularly in regard to soil dynamics as detailed below.
In this work, we only considered homogeneous soils, and the model should be extended to heterogeneous soils. Root water uptake and soil heterogeneity have not often been considered simultaneously, although the variability of soil hydraulic properties significantly affects flow processes and root uptake patterns as stressed out in [42].
Moreover, hysteresis effects were neglected, although they can be of importance when considering irrigation or rainfall in combination with root water uptake. As suggested in chapter 3, hysteresis can be taken into account in the model for example by including empirical hysteresis models such as [41] based on main wetting and drying curves.

In addition, a number of soil processes affecting solute movement and availability are simplified or neglected.
As stated in chapter 3, the simple scalar diffusion coefficient in the convection-diffusion

equation can easily be replaced by the effective dispersion coefficient tensor to account for dispersibility, since water flow is explicitly considered.

In most plant nutrition models, chemical interactions between dissolved elements and the soil are reduced to a buffer power or simplified by using the Freundlich adsorption isotherm, as is the case in this work. The Freundlich equation is an empirical relation between the solute concentration in the liquid phase and the amount adsorbed to soil particles and fails to account for changes of nutrient availability arising from the range of biogeochemical and biochemical processes that occur in the rhizosphere [23, 67]. Future root uptake models should be coupled with mechanistic surface complexation models using thermodynamic and kinetic relationships in order to include soil processes affecting sorbing surfaces [58, 50]. In particular, biogeochemical interactions and microbial activity in the rhizosphere can have major effects on soil properties and ultimately impact the acquisition of nutrients by plants. Root-induced variations in soil pH also play an important role in rhizosphere dynamics, although prediction of rhizosphere pH is a difficult task due to its implication in numerous chemical reactions.

The model also makes a number of simplifications regarding root structure and function.

Osmotic gradients were neglected, although they can significantly affect root water uptake, especially when considering salt accumulation at the root-soil interface caused by salt transport towards the roots by mass flow through the soil. This salinity buildup in the rhizosphere can lead to large osmotic gradients across the roots, effectively reducing root water uptake.

In the simulations, we also used a simplified representation of the hydraulic architecture of the root system by considering constant radial and axial conductivities. In reality, root conductivity is a function of root type and age and varies along root axes. The radial conductivity is affected by the development of apoplastic barriers [71] and by the activity of aquaporins [53], while the axial conductivity depends on the development stage of the xylem. In addition, cavitation may occur in the xylem at low water potentials, causing embolisms and decreasing the axial conductivity [70].

On a similar note, we used a simple Michaelis-Menten model assuming that the nutrient uptake capacity is evenly distributed over the whole root system, while there is experimental evidence that nutrient uptake is not uniform along root axes [17] and depends on root age [15, 60].

Besides, the model can be enhanced by considering multiphasic nutrient uptake [57], taking into account separate high-affinity and low-affinity transporters operating at different concentration ranges.

During soil drying, root-soil air gaps can develop due to root shrinkage, reducing the surface area of the roots in contact with the soil and leading to a decrease of the hydraulic conductivity at the root-soil interface. This can be taken into account in the model for example by assuming that the radial conductivity of the root is proportional to the relative saturation of the soil [29].

Besides, we did not consider physical constraints that soil strength and structure can exert on root growth and development, although root growth induces a substantial reorganization of the soil matrix via aggregation and compaction processes [31].

Root hairs and mycorrhizal hyphae are of crucial importance for the acquisition of poorly mobile nutrients such as P. They can explore a greater volume of soil and dramatically increase the surface area for uptake [21, 33]. Mathematical models have been developed to account for P depletion zones around root hairs [47] and mycorrhizal hyphae [66] at the single root scale. Our model could be improved for example by defining sink terms in the root hair zone, similar to the sink term accounting for uptake by root hairs that was obtained in [47] by the method of homogenization.

Finally, as a response to P deficiency, plants can release organic acid ions such as citrate in the soil solution that compete for sorption sites with P, resulting in increased P availability for uptake [48]. The effects of root citrate exudation can be included by considering coupled partial differential equations describing the evolution of the concentration of phosphate and citrate in the liquid and solid phases.

From a mathematical point of view, future work could consist in establishing convergence for the discretization of the diffuse domain problems introduced in chapter 4 using the framework of gradient schemes [16].

From a numerical point of view, extending the domain decomposition method discussed in chapter 3 to the diffuse domain problems presented in chapter 4 involving root growth and transient mesh adaptation should lead to more scalable parallel algorithms and drastically reduce memory requirements. However, combining domain decomposition methods and transient mesh adaptation is not an easy task, as one has to consider practical dynamic load balancing, repartitioning and interface remeshing techniques.

Following on from the shape optimization procedure introduced in chapter 2, future work could also consist in formulating a parametric or geometric shape optimization problem for the model presented in chapter 4 with realistic constraints regarding root shapes and root growth rules, so as to study the effect of root morphological traits and root system architecture on uptake capacity in various scenarios.

Overall, the models developed in this thesis can help us further our understanding of plant-soil relationships over a range of spatial scales and ultimately make better use of belowground interactions in order to improve the sustainability of agricultural systems.

Bibliography

[1] Amestoy, P., Duff, I., L'Excellent, J., Koster, J.: A fully asynchronous multifrontal solver using distributed dynamic scheduling. SIAM Journal on Matrix Analysis and Applications **23**(1), 15–41 (2001)

[2] Aslyng, H., et al.: Soil physics terminology. Int. Soc. Soil Sci. Bull **23**(7) (1963)

[3] Barber, S.A.: Soil nutrient bioavailability: a mechanistic approach. Wiley-Interscience, New York (1984)

[4] Barraclough, P.B., Tinker, P.B.: The determination of ionic diffusion coefficients in field soils. I. diffusion coefficients in sieved soils in relation to water content and bulk density. Journal of Soil Science **32**(2), 225–236 (1981)

[5] Berninger, H.: Domain decomposition methods for elliptic problems with jumping nonlinearities and application to the Richards equation. Ph.D. thesis, Freie Universität Berlin (2007)

[6] Celia, M.A., Bouloutas, E.T., Zarba, R.L.: A general mass-conservative numerical solution for the unsaturated flow equation. Water Resources Research **26**(7), 1483–1496 (1990)

[7] Ciarlet, P.G.: Discrete maximum principle for finite-difference operators. Aequationes mathematicae **4**(3), 338–352 (1970)

[8] Comte, M., Coron, J.M., Guerrero, S., Tournier, P.H.: Analysis of a model of phosphorus uptake by plant roots. Journal of Evolution Equations **13**(3), 595–615 (2013)

[9] Cordell, D., Drangert, J.O., White, S.: The story of phosphorus: Global food security and food for thought. Global environmental change **19**(2), 292–305 (2009)

[10] Dapogny, C., Dobrzynski, C., Frey, P.: Three-dimensional adaptive domain remeshing, implicit domain meshing, and applications to free and moving boundary problems. Journal of Computational Physics **262**(0), 358 – 378 (2014)

[11] Dixon, H.H., Joly, J.: On the ascent of sap. Philosophical Transactions of the Royal Society of London. B pp. 563–576 (1895)

[12] Dobrzynski, C.: MMG3D: User Guide. Rapport Technique RT-0422, INRIA (2012)

[13] Doussan, C., Pagès, L., Vercambre, G.: Modelling of the hydraulic architecture of root systems: An integrated approach to water absorption - model description. Annals of Botany **81**, 213–223 (1998)

[14] Doussan, C., Pierret, A., Garrigues, E., Pagès, L.: Water uptake by plant roots: II - modelling of water transfer in the soil root-system with explicit account of flow within the root system - comparison with experiments. Plant and Soil **283**(1-2), 99–117 (2006)

[15] Ernst, M., Römheld, V., Marschner, H.: Estimation of phosphorus uptake capacity by different zones of the primary root of soil-grown maize (zea mays l.). Zeitschrift für Pflanzenernährung und Bodenkunde **152**(1), 21–25 (1989)

[16] Eymard, R., Guichard, C., Herbin, R., Masson, R.: Gradient schemes for two-phase flow in heterogeneous porous media and Richards equation. ZAMM-Journal of Applied Mathematics and Mechanics/Zeitschrift für Angewandte Mathematik und Mechanik (2013)

[17] Ferguson, I., Clarkson, D.: Ion transport and endodermal suberization in the roots of zea mays. New phytologist **75**(1), 69–79 (1975)

[18] Fiscus, E.L.: The interaction between osmotic- and pressure-induced water flow in plant roots. Plant Physiology **55**(5), 917–922 (1975)

[19] Frey, P.: Error estimate for 2d and 3d unstructured meshes (2010). URL `http://www.ann.jussieu.fr/frey/software.html`

[20] Friedman, A.: Partial differential equations of parabolic type. Prentice-Hall, Englewood Cliffs, NJ. (1964)

[21] Gahoonia, T.S., Nielsen, N.E.: Root traits as tools for creating phosphorus efficient crop varieties. Plant and Soil **260**(1-2), 47–57 (2004)

[22] Galloway, J.N., Townsend, A.R., Erisman, J.W., Bekunda, M., Cai, Z., Freney, J.R., Martinelli, L.A., Seitzinger, S.P., Sutton, M.A.: Transformation of the nitrogen cycle: Recent trends, questions, and potential solutions. Science **320**(5878), 889–892 (2008)

[23] Geelhoed, J., Van Riemsdijk, W., Findenegg, G.: Simulation of the effect of citrate exudation from roots on the plant availability of phosphate adsorbed on goethite. European Journal of Soil Science **50**(3), 379–390 (1999)

[24] Griffon, M.: Nourrir la planète. Odile Jacob (2006)

[25] Gruber, N., Galloway, J.N.: An earth-system perspective of the global nitrogen cycle. Nature **451**(7176), 293–296 (2008)

[26] Haslinger, J., Makinen, R.A.E.: Introduction to Shape Optimization: Theory, Approximation, and Computation. Society for Industrial and Applied Mathematics, Philadelphia, PA (2003)

[27] Hecht, F.: New development in freefem++. Journal of Numerical Mathematics **20**, 251–266 (2013)

[28] Henrot, A., Pierre, M.: Variation et optimisation de formes: une analyse géométrique. Springer, Berlin (2005)

[29] Herkelrath, W., Miller, E., Gardner, W.: Water uptake by plants: II. the root contact model. Soil Science Society of America Journal **41**(6), 1039–1043 (1977)

[30] Herring, J.R., Fantel, R.J.: Phosphate rock demand into the next century: impact on wolld food supply. Nonrenewable Resources **2**(3), 226–246 (1993)

[31] Hinsinger, P., Bengough, A.G., Vetterlein, D., Young, I.M.: Rhizosphere: biophysics, biogeochemistry and ecological relevance. Plant and soil **321**(1-2), 117–152 (2009)

[32] Hinsinger, P., Plassard, C., Tang, C., Jaillard, B.: Origins of root-mediated ph changes in the rhizosphere and their responses to environmental constraints: a review. Plant and soil **248**(1-2), 43–59 (2003)

[33] Hodge, A., Helgason, T., Fitter, A.: Nutritional ecology of arbuscular mycorrhizal fungi. Fungal Ecology **3**(4), 267–273 (2010)

[34] ávan den Honert, T.: Water transport in plants as a catenary process. Discussions of the Faraday Society **3**, 146–153 (1948)

[35] Hopmans, J.W., Bristow, K.L.: Current capabilities and future needs of root water and nutrient uptake modeling. In: D.L. Sparks (ed.) Advances in Agronomy, *Advances in Agronomy*, vol. 77, pp. 103 – 183. Academic Press (2002)

[36] Javaux, M., Schröder, T., Vanderborght, J., Vereecken, H.: Use of a three-dimensional detailed modeling approach for predicting root water uptake. Vadose Zone Journal **7**, 1079–1088 (2008)

[37] Ji, S.H., Park, Y.J., Sudicky, E.A., Sykes, J.F.: A generalized transformation approach for simulating steady-state variably-saturated subsurface flow. Advances in Water Resources **31**(2), 313–323 (2008)

[38] Jolivet, P., Dolean, V., Hecht, F., Nataf, F., Prud'homme, C., Spillane, N.: High performance domain decomposition methods on massively parallel architectures with freefem++. Journal of Numerical Mathematics **20**, 287–302 (2013)

[39] Karypis, G., Kumar, V.: A fast and high quality multilevel scheme for partitioning irregular graphs. SIAM Journal on Scientific Computing **20**, 359–392 (1998)

[40] Kochian, L.V., Lucas, W.J.: Potassium transport in corn roots: I. resolution of kinetics into a saturable and linear component. Plant Physiology **70**(6), 1723–1731 (1982)

[41] Kool, J.B., Parker, J.C.: Development and evaluation of closed-form expressions for hysteretic soil hydraulic properties. Water Resources Research **23**(1), 105–114 (1987)

[42] Kuhlmann, A., Neuweiler, I., Zee, S., Helmig, R.: Influence of soil structure and root water uptake strategy on unsaturated flow in heterogeneous media. Water Resources Research **48**(2) (2012)

[43] Ladyzenskaya, O., Solonnikov, V., Ural'ceva, N.: Linear and Quasilinear Equations of Parabolic Type, *Translations of Mathematical Monographs*, vol. 23. American Mathematical Society, Providence, R.I. (1968)

[44] Lambers, H., Shane, M.W., Cramer, M.D., Pearse, S.J., Veneklaas, E.J.: Root structure and functioning for efficient acquisition of phosphorus: matching morphological and physiological traits. Annals of botany **98**(4), 693–713 (2006)

[45] Landsberg, J., Fowkes, N.: Water movement through plant roots. Annals of Botany **42**(1), 493–508 (1978)

[46] Leitner, D., Klepsch, S., Bodner, G., Schnepf, A.: A dynamic root system growth model based on L-Systems. Plant and Soil **332**(1-2), 177–192 (2010)

[47] Leitner, D., Klepsch, S., Ptashnyk, M., Marchant, A., Kirk, G., Schnepf, A., Roose, T.: A dynamic model of nutrient uptake by root hairs. New Phytologist **185**(3), 792–802 (2010)

[48] Li, M., Shinano, T., Tadano, T.: Distribution of exudates of lupin roots in the rhizosphere under phosphorus deficient conditions. Soil Science and Plant Nutrition **43**(1), 237–245 (1997)

[49] Li, X., Lowengrub, J., Rätz, A., Voigt, A.: Solving pdes in complex geometries: A diffuse domain approach. Commun. Math. Sci. **7**, 81–107 (2009)

[50] Luster, J., Göttlein, A., Nowack, B., Sarret, G.: Sampling, defining, characterising and modeling the rhizosphere-the soil science tool box. Plant and Soil **321**(1-2), 457–482 (2009)

[51] Mackenzie, F.T., Ver, L.M., Lerman, A.: Century-scale nitrogen and phosphorus controls of the carbon cycle. Chemical Geology **190**(1), 13–32 (2002)

[52] Marschner, H., Marschner, P.: Marschner's mineral nutrition of higher plants, vol. 89. Academic press (2012)

[53] Maurel, C., Verdoucq, L., Luu, D.T., Santoni, V.: Plant aquaporins: membrane channels with multiple integrated functions. Annu. Rev. Plant Biol. **59**, 595–624 (2008)

[54] McGechan, M., Lewis, D.: Sorption of phosphorus by soil, part 1: Principles, equations and models. Biosyst. Eng. **82**, 1–24 (2002)

[55] Mollier, A., Willigen, P.D., Heinen, M., Morel, C.: A two dimensional simulation model of phosphorus uptake including crop growth and P response. Eco. Mod. **210**, 453–464 (2008)

[56] Morel, C.: Caractérisation de la phytodisponibilité du phosphore du sol par la modélisation du transfert des ions phosphates entre le sol et la solution. Mémoire d'HDR, INPL Nancy **80** (2002)

[57] Nissen, P.: Nutrient uptake by plants: effect of external ion concentrations. Acta Horticulturae (Netherlands) **178**, 21–28 (1986)

[58] Nowack, B., Mayer, K., Oswald, S., Van Beinum, W., Appelo, C., Jacques, D., Seuntjens, P., Gérard, F., Jaillard, B., Schnepf, A., et al.: Verification and intercomparison of reactive transport codes to describe root-uptake. Plant and soil **285**(1-2), 305–321 (2006)

[59] Pop, I.S.: Error estimates for a time discretization method for the Richards' equation. Computational Geosciences **6**(2), 141–160 (2002)

[60] Reidenbach, G., Horst, W.J.: Nitrate-uptake capacity of different root zones of zea mays (l.) in vitro and in situ. Plant and Soil **196**(2), 295–300 (1997)

[61] Richards, L.A.: Capillary Conduction of Liquids Through Porous Mediums. Physics **1**, 318–333 (1931)

[62] Roose, T., Fowler, A.C., Darrah, P.R.: A mathematical model of plant nutrient uptake. J. Math. Biol. **42**, 347–360 (2001)

[63] Runge-Metzger, A.: Closing the cycle: obstacles to efficient P management for improved global food security. Scope-Scientific Committee on Problems of the Environment International Council of Scientific Unions **54**, 27–42 (1995)

[64] Saaltink, M.W., Carrera, J., Olivella, S.: Mass balance errors when solving the convective form of the transport equation in transient flow problems. Water Resources Research **40**(5) (2004)

[65] Schneider, C., Attinger, S., Delfs, J.O., Hildebrandt, A.: Implementing small scale processes at the soil-plant interface–the role of root architectures for calculating root water uptake profiles. Hydrology and Earth System Sciences **14**(2), 279–289 (2010)

[66] Schnepf, A., Roose, T., Schweiger, P.: Impact of growth and uptake patterns of arbuscular mycorrhizal fungi on plant phosphorus uptake-a modelling study. Plant and soil **312**(1-2), 85–99 (2008)

[67] Silberbush, M., Barber, S.: Sensitivity of simulated phosphorus uptake to parameters used by a mechanistic-mathematical model. Plant and soil **74**(1), 93–100 (1983)

[68] Sokolowski, J., Zolesio, J.: Introduction to Shape Optimization: Shape Sensitivity Analysis. Springer-Verlag, Berlin (1992)

[69] Somma, F., Hopmans, J., Clausnitzer, V.: Transient three-dimensional modeling of soil water and solute transport with simultaneous root growth, root water and nutrient uptake. Plant and Soil **202**(2), 281–293 (1998)

[70] Sperry, J.S., Stiller, V., Hacke, U.G.: Xylem hydraulics and the soil–plant–atmosphere continuum: Opportunities and unresolved issues. Agron. J **95**, 1362–1370 (2003)

[71] Steudle, E., Peterson, C.A.: How does water get through roots? Journal of Experimental Botany **49**(322), 775–788 (1998)

[72] Stevens, D., Power, H.: A scalable and implicit meshless RBF method for the 3D unsteady nonlinear Richards equation with single and multi-zone domains. International Journal for Numerical Methods in Engineering **85**(2), 135–163 (2011)

[73] Stewart, W., Hammond, L., van Kauwenbergh, S., Sims, J., Sharpley, A., et al.: Phosphorus as a natural resource. Phosphorus: agriculture and the environment pp. 3–22 (2005)

[74] Tinker, P.B., Nye, P.H.: Solute movement in the rhizosphere (2000)

[75] Tournier, P.H.: Adaptive simulation of root water and nutrient uptake by growing plant root systems using a diffuse domain approach. Submitted (2014)

[76] Tournier, P.H., Hecht, F., Comte, M.: Finite element model of soil water and nutrient transport with root uptake: Explicit geometry and unstructured adaptive meshing. Transport in Porous Media **106**(2), 487–504 (2015)

[77] Tuzet, A., Perrier, A., Leuning, R.: A coupled model of stomatal conductance, photosynthesis and transpiration. Plant, Cell & Environment **26**(7), 1097–1116 (2003)

[78] Vance, C.P., Uhde-Stone, C., Allan, D.L.: Phosphorus acquisition and use: critical adaptations by plants for securing a nonrenewable resource. New Phytologist **157**(3), 423–447 (2003)

[79] Varado, N., Braud, I., Ross, P., Haverkamp, R.: Assessment of an efficient numerical solution of the 1D Richards' equation on bare soil. Journal of Hydrology **323**(1-4), 244–257 (2006)

[80] Vitousek, P.M., Aber, J.D., Howarth, R.W., Likens, G.E., Matson, P.A., Schindler, D.W., Schlesinger, W.H., Tilman, D.G.: Human alteration of the global nitrogen cycle: sources and consequences. Ecological applications **7**(3), 737–750 (1997)

[81] Vohralík, M., Wheeler, M.: A posteriori error estimates, stopping criteria, and adaptivity for two-phase flows. Computational Geosciences **17**(5), 789–812 (2013)

[82] Šimůnek, J., Hopmans, J.W.: Modeling compensated root water and nutrient uptake. Ecological Modelling **220**(4), 505–521 (2009)